Tanja Pelzmann, BSc

Study of Creep Behaviour of Advanced 9%Cr Steel Welds for High Temperature Application

MASTER THESIS

For obtaining the academic degree
Diplom-Ingenieur

Master Programme of
Advanced Materials Science

Graz University of Technology

Supervisor:

Univ.-Prof. Dr.tech. Christof Sommitsch

Co-Supervisor:

Dipl.-Ing. Dr. Coline Béal

Institute of Materials Science and Welding

Graz, June 2014

EIDESSTATTLICHE ERKLÄRUNG

AFFIDAVIT

Ich erkläre an Eides statt, dass ich die vorliegende Arbeit selbstständig verfasst, andere als die angegebenen Quellen/Hilfsmittel nicht benutzt, und die den benutzten Quellen wörtlich und inhaltlich entnommenen Stellen als solche kenntlich gemacht habe. Das in TUGRAZonline hochgeladene Textdokument ist mit der vorliegenden Masterarbeit identisch.

I declare that I have authored this thesis independently, that I have not used other than the declared sources/resources, and that I have explicitly indicated all material which has been quoted either literally or by content from the sources used. The text document uploaded to TUGRAZonline is identical to the present master‘s thesis.

Datum / Date

Unterschrift / Signature

Abstract

This work counts among the numerous efforts to improve the creep behaviour of welded components of 9% Chromium steels in order to satisfy the ongoing attempts of further increasing the operating factors temperature and pressure. A main focus is therefore set on the optimisation of the weldment in order to obtain a high quality and improved in-service performance. Such optimization is based on the choice of a suitable base material, an optimized welding procedure and a proper post weld heat treatment. The investigations presented in this thesis comprise an extensive weldability study of electron beam welding of martensitic 9% Chromium steel micro-alloyed with Boron and Nitrogen. The weldability study, covering an initial blind weld study and subsequent butt weld study, is performed on two different steels with slightly different chemical compositions and a given thickness of 25 mm. The weldments are analyzed and characterized in order to further refine the parameter window. Finally a complete parameter set permitting to obtain defect-free welds for the given material and thickness is proposed. In addition, the influence of the post-weld heat treatment on mechanical properties, in particular on the hardness in the heat affected zone, and on the microstructure is investigated. The obtained very sound and narrow heat affected zone, which is an advantage for the creep resistance, complicates the microstructural investigation of the different sub-zones. Microstructure areas, which are related by their distance from the weld center to a certain peak temperature, are additionally thermally simulated using a Gleeble system to investigate the creep behaviour of the different sub-zones. As an outcome, high quality EB welds and simulated heat affected zones for subsequent creep testing were obtained. The second part of the present thesis deals with evaluation of synchrotron micro-computed tomographic data. The samples measured are of another 9% Chromium steel but again with a chemical composition comparable to the material used in the experimental part. The samples were tungsten inert gas welded using a Nickel-based filler material and subject to creep tests at 650 °C and different stress levels. The investigated samples were extracted from the heat affected zone near the fusion zone after rupture. From the qualitative and quantitative analyses of the existing creep pores, conclusions on the size and spatial distribution of the pores within the heat affected zone are drawn.

Kurzfassung

Diese Arbeit gliedert sich in die zahlreichen Bemühungen ein, die Kriechbeständigkeit geschweißter Komponenten 9% Chromstähle zu erhöhen um so dem fortwährenden Bestreben die Betriebsparameter Druck und Temperatur anzuheben, gerecht zu werden. Im Zentrum dieser Anstrengungen stehen daher die Optimierung der Schweißnaht im Hinblick auf ihre Qualität und verbessertes Betriebsverhalten. Die Optimierung der Schweißnaht wiederum fußt auf der Wahl eines geeigneten Grundwerkstoffs, eines geeigneten Schweißverfahrens und schließlich einer angepassten Wärmenachbehandlung. Die in dieser Arbeit präsentierten Untersuchungen umfassen aufwändige Studien zur Ermittlung der optimalen Schweißparameter für das Elektronenstrahlschweißen eines mit Bor und Stickstoff modifizierten martensitischen 9% Chromstahls. Die Parameterstudie wurde mit zwei Stählen vergleichbarer chemischer Zusammensetzung und einer festgelegten Dicke von 25 mm sowohl für Blindschweiß- als auch Stoßnähte durchgeführt. Das Schweißgut wurde jeweils analysiert und charakterisiert um das Parameterfenster weiter zu verfeinern. Schließlich wird ein vollständiges Parameterset zur Generierung defektfreier, reproduzierbarer Schweißnähte für den vorgegebenen Werkstoff bei gegebener Dicke vorgestellt. Ebenfalls wurde der Einfluss der Wärmenachbehandlung der Schweißnähte im Hinblick auf die mechanischen Eigenschaften untersucht, insbesondere der Härte in der Wärmeeinflusszone. Die besonders schmal ausgeprägte Wärmeeinflusszone, die für die Kriecheigenschaften von Vorteil ist, erschwert jedoch die mikroskopische Untersuchung der einzelnen Subzonen. Daher wurden Gefügebereiche, die aufgrund ihres Abstands von der Schweißzentrumslinie einer gewissen Maximaltemperatur zugeordnet werden können, zusätzlich thermisch mittels Gleeble-Experimenten simuliert. Als Ergebnis, konnten Elektronenstrahl geschweißte Proben hoher Qualität, sowie Proben mit thermisch simulierten zugehörigen Wärmeeinflusszonen gewonnen werden. Der zweite große Teil dieser Arbeit befasst sich mit der Auswertung von Synchrotron-Computer-Tomographie-Daten. Bei den untersuchten Proben handelte es sich ebenfalls um einen martensitischen 9% Chromstahl ähnlicher chemischer Zusammensetzung wie die Stahlproben, die im experimentellen Teil verwendet wurden. Die Proben wurden mittels Wolfram-Inert-Gas unter Verwendung eines Nickel-basierten Zusatzwerkstoffes geschweißt sowie anschließend einer Zeitstandprüfung bei einer Temperatur von 650 °C und verschiedenen Spannungen unterzogen. Die qualitative und quantitative Analyse der in den Proben vorhandenen Kriechporen erlaubt Rückschlüsse auf die Porengrößenverteilung, so wie ihre räumliche Verteilung innerhalb der Wärmeeinflusszone.

Contents

1 Introduction

Over the last decades a growing energy demand can be observed which calls for the raise of the thermal efficiency of existing power plants and has consequently entailed numerous international projects and collaborations since the late 1960's in order to accommodate this demand. The KMM-VIN network (European Virtual Institute on Knowledge-based Multifunctional Materials AISBL) is among those and presents the framework that is used in this thesis.
The maximum degree of efficiency achievable by a heat engine is given by Carnot's efficiency and limited by the second law of thermodynamics. A proper thermodynamical design as well as an increase of the operating temperature and pressure allows to approach this ideal efficiency [1]. While the efforts have been more focused on an optimisation of design aspects in the beginning of this evolution, they currently focus on the material development to a greater extend. In the last years, the intensive investigation and research activities, which were also strongly promoted by the Institute of Materials Science and Welding, Graz University of Technology led to the development of martensitic 9-12% Chromium steels. Due to its good tradeoff between adequate corrosion resistance, mechanical properties and considerably lower price (compared to other materials fulfilling the requirements), this material type can now be identified as the favorite steel for thick-wall components in modern thermal power plants. In addition, a decisive selection criterion in the context of utilisation and installation of these materials in power plants is given by their ability to be joined. The joining technologies particularly focus on the weldability of the material, because welding is the major joining and service technology for such applications. Not only the base material design must be aligned with the elevated temperature regime and stress states but also the microstructure caused by the welding procedure. The weld thermal cycle initiates

microstructural transformations in the heat affected zone which has been found to be sensitive to several cracking mechanisms during subsequent creep load [2]. The heat affected zone is therefore the weakest part of the weldment. One specific cracking mechanism - type IV cracking - turns out to be the dominant failure when operating in the creep regime and is therefore the true limiting factor of the part shelf life. Beyond that, the cracking mechanism in question can even be linked to a particular region within the heat affected zone.

It would stand to reason to minimize the heat affected zone. Among the many endeavours pursuing to solve this issue, electron beam welding suggests itself. Due to its high energy density, this welding technique allows quite more narrow and deeper weld joints with lower total heat input resulting in a very small heat affected zone compared to conventional methods e.g. arc welding [3]. The high penetration depth makes multi layer weldments obsolete and a narrow heat affected zone presents a smaller target for crack development in the creep regime.

What is the real potential and the possibilities for achievement of EBW for martensitic 9% Chromium steels? It is not a matter of proving the general applicability (since electron beam welding installations are already available in industrial environments), but to optimise the welding parameters such as accelerating voltage, beam current and welding speed for a given material and thickness in order to get the desired microstructure and mechanical properties. Aside of these aspects, the reproducibility and overall quality of the weld seams should be brought into better focus. All these investigations seek to yield an optimised joint weld from which creep samples are then extracted. Only the creep tests in the intended temperature regime of 650 °C will give a clear answer to the above question.

The content of this thesis is structured in order to follow the performed experimental procedures, starting with a thorough review of related work in that field. The literature survey given in the following chapter (see Chap. 2) provides an overview of the material class of 9-12% Chromium steels. The challenges and problems when welding this material in view of microstructural characteristics of the heat affected zone and how they impact the mechanical and the creep behaviour of the welded joint is put in a nutshell. At the end of this chapter the current state of research is presented with regard to welding of martensitic 9% chromium steels which prepared the ground for the development of a new kind of heat resistant steels with both an improved base and weld material.

The third chapter provides an overview of the used materials and conditions as well as the performed quality heat treatment. The methods used for characterising the welds (Sec. 3.3) are shortly listed, but the welding-related methods comprising the electron

beam welding technology, the Gleeble® physical simulation of the heat affected zone, and the post-weld heat treatment specifications are discussed in more detailed later on (see Sec. 3.2).
Chapter four presents all experimental results. A circumspect characterisation of the steel plates in the as-received state (Sec. 4.1) and after the heat-treatment is given together with the process of the welding parameter determination (Sec. 4.2). The results of the joint weld experiments is the major topic of this chapter and are complemented with dilatometer measurements. Furthermore, the Gleeble® heat affected zone simulation results are presented (Sec. 4.5).
Beside the active investigation on the welding behaviour of the received material, present synchrotron data from a creep tested cross weld martensitic 9% Chromium steel was evaluated as well. The extensive analysis of the sample data with regard to pore size and distribution is addressed in a separate chapter (Chap. 5). The results of the data are supplemented by a closer look on the analytical method itself and the mathematical methods, e.g. filtering and rendering of the data as well as their influence on the results.
The last chapter 6 aims at summarising both the results of the welding experiments and the evaluated synchrotron data. Where possible, reasonable conclusions connecting the results from Chapter 4 and 5 are drawn to enable further improvement for future experiments.

2 Current State of Research

In the present chapter, the current state of research in associated fields is summarised with regard to the development and evolution of the material as well as its weldability and the influence on the creep behaviour in the desired temperature regime. Consequently, a brief introduction to the concept of the heat affected zone, and its different sub-regions is provided. At the end, the phenomenon of creep is generally discussed and linked with typical failure mechanisms limiting the in-service live of welded parts.

2.1 9-12%Cr Steels

The present work is built on the extensive research activities at the IWS since the early nineties and continues the investigations on creep resistant ferritic steels for the use in thermal power plants. It goes without saying, that the history of the material development, the material characteristics as well as the characterisation of weldments has been already outlined and discussed in a very detailed way in many previous works and publications. The gentle reader may therefore be referred to the doctoral thesis of B. Sonderegger [5] which provides a summary of the IWS research activities. Furthermore the thesis of E. Letofsky [6] shall be explicitly mentioned which gives a very good overview of the requirement profile for this material group.
Starting in the late seventies, many different ferritic/martensitic steels were developed in Japan and USA based on the already known 9% steel T9 used for chemical plants and refinieries. The alloying concept was improved in the following decades by the addition of V, Nb, N. The material group of 9-12% Chromium steels is among the martensitic

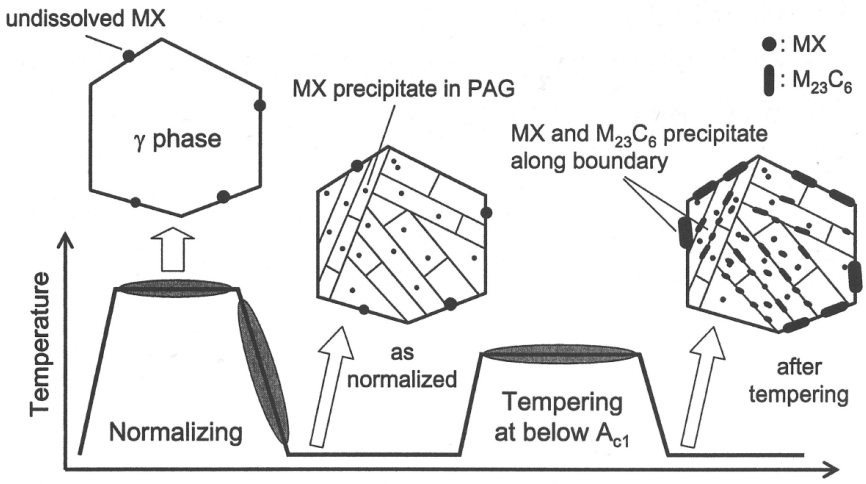

Figure 2.1: Development of the microstructure during the heat treatment typical for QT steels, adopted from [4].

quenched and tempered steels (QT steels). The development of microstructure during the quality heat treatment of the as-cast material is shown in Fig. 2.1. The solution annealing is typically performed aroung 1100 °C in the upper γ-regime in order to obtain a fully austenitic microstructure, the majority precipitates dissolve. The subsequent quenching of the material causes a transformation from austenite to martensite. The alloying elements stabilizing the ferritic structure are also the reason why many of these steels are air-hardening where static air cooling is sufficient to obtain the martensitic structure. During the precipitation hardening below the austenite transformation temperature, the distorted martensitic microstructure is tempered and fine precipitates form at preferred nucleation sites like grain laths or boundaries. These steels are also characterised by a high thermal conductivity and small heat expansion and the martensite structure provides an ideal platform for high creep resistance [5]. The creep performance is influenced to a high degree by the strengthening mechanisms, which is described in a later section of this chapter. The strengthening is mainly achieved by solid solution and precipitation strengthening. The integration of foreign atoms on parent lattice sites and their interaction with dislocations leads to the hindrance of the same. Precipitates incorporate new phase boundaries into the matrix and also hinder the dislocation movement. The size, distribution, volume fraction and dispersion mainly determine the effect. The alloying elements and their roles for the microstructural improvement are listed in Tab. 2.1. However, 9-12% Chromium steels exhibit limited service lifetime and failure, but based on different mechanisms depending on the Cr content. Above 11% Chromium, Z-phase may form and lead to steel embrittlement while at lower Chromium contents the efffect of the coarsening of $M_{23}C_6$ carbides

dominate. To date, there have been many reports of failures of weldments for both classes [7].

Table 2.1: Role of alloying elements in iron-based superalloys after [8]. Not all of the listed effects occur in a given alloy.

Effect	**Elements**
Solid-solution strengtheners	Cr, Mo, W
Fcc matrix stabilizers	C, W, Ni
Carbide form:	
MC	Ti
M_7C_3	...
$M_{23}C_6$	Cr, Mo
M_6C	Mo
Carbonitrides: M(CN)	C, N
Promotes general precipitation of carbides	P
Forms γ' Ni_3(Al,Ti)	Al, Ni, Ti
Retards formation of hexagonal η (Ni_3Ti)	Al, Zr
Hardening precipitates and/or intermetallics	Al, Ti, Nb
Oxidation resistance	Cr, Mo
Improve hot corrosion resistance	La, Y
Sulfidation resistance	Cr
Improves creep properties	B
Increases rupture strength	B

2.2 Welding of martensitic 9-12%Chromium Steels

As it can be seen from Tab. 2.1, elements like Carbon or Nickel stabilize the austenite regime while Chromium stabilizes the ferritic structure. Thus, the austenitic region, generated in the heat affected zone during welding, transforms always to martensite by air-hardening. The influence of the different alloying elements are summarised in the carbon equivalent, which is an expression of the weldability of the material. Several different methods for the assessement of the carbon equivalent are available, but as a general rule, a steel is regarded as weldable if C_{equ} <0.45 [9]. Higher values of C_{equ} lead to a hardness increase and embrittlement in the heat affected zone. Thus, only martensitic Chromium steels with low carbon (below 0.15%) content exhibit a satisfying weldability. Furthermore, a post-weld heat treatment is required in any case to temper the martensite formed in the heat affected zone during welding.

2.3 The Heat Affected Zone (HAZ)

Besides the effects and processes involved when a material is heated above its melting temperature due to welding and its solidification hereafter, also the material close to the molten zone is exposed to a thermal cycle. The properties and microstructure of this region are changed - this is why it is often referred to as heat affected zone (abbreviated with HAZ in the further text). However, the induced changes are by no means uniform, thus the zone is further divided into subregions as indicated in Fig. 2.2. Each of this subregions is described by its own microstructure related to the experienced thermal cycle and by its unique mechanical properties. Because of this gradient in microstructure and properties, the heat affected zone plays such a substantial role when it comes to the creep behaviour of welded materials.
The specific structure and width of each subregion depend upon the applied thermal cycle and the properties of the base material including its thermal and/or mechanical history. The complete thermal cycle is characterised by the heating and cooling rate as well as on the dwell time, denoting the time the material is exposed (at a given point) to a given peak temperature. It is more convenient to discuss the different stages of the complete thermal cycle separately and translate the ideas afterwards into the different sub-zones shown in Fig. 2.2.
The heating cycle has an impact on the degree of superheating, the dissolution of precipitates and is thus mainly responsible for the grain growth properties [9]. Processes such as phase transformations, the evolution of precipitates or grain size are interconnected and are influenced by the thermal cycle. High heating rates lead to a superheating of the material which causes a shift of possible phase transformations to higher temperatures compared to those indicated in the phase diagram. This may also shift the dissolution of some precipitates to higher temperatures. Some precipitates may dissolve while others stay stable due to the superheating of the material and pin the grain boundaries. This so-called Zener-drag determines the size of the growing grains by the volume fraction and radius of the present particles. Processes starting in the heating cycle, like grain growth and solution of particles, are continued during the dwell time. The dwell-time and the related peak temperature determine the different regions in the heat affected zone. The majority of metals exhibit grain growth due to the weld thermal cycle [9]. Stable precipitates do not completely disable grain growth but remarkably reduce it by pinning the grain boundaries.
Assuming particle dissolution during weld, the edge of the grain growth zone corresponds to the precipitate solubility borderline. A pre-heating treatment encourages the

effect since the thermal input is additive to the weld energy input and also the cooling is delayed. On the other hand, the presence of precipitates such as carbides or nitrides does not completely suppress grain growth but it is of course less pronounced. [9]
The rapid cooling rate implies that the phase transformations do not usually occur under equilibrium conditions [9] and limits diffusional processes. The development of a new phase requires the availability of sufficient nucleation sites (f.e. free surfaces, grain boundaries, inclusions) and enough time to overcome the critical radius for further growth. The cooling rate influences the formation of different morphologies, modes of growth, composition and lattice structures [9]. The continuous-cooling-temperature (CCT) diagrams allow to determine the finally obtained structures depending on the applied heating cycle and cooling rate. At very high cooling rates, diffusion is no longer possible and non-diffusional phase transitions such as the formation of martensite will occur.
The above consequences can now be applied to the subzones indicated by Roman numerals in Fig. 2.2 by taking their experienced thermal cycle into account. It has to be noted, that the below descriptions of the regions allude to the FeC-phase diagram and so does the naming of the phases. Nevertheless the overall concept is valid for all metals.

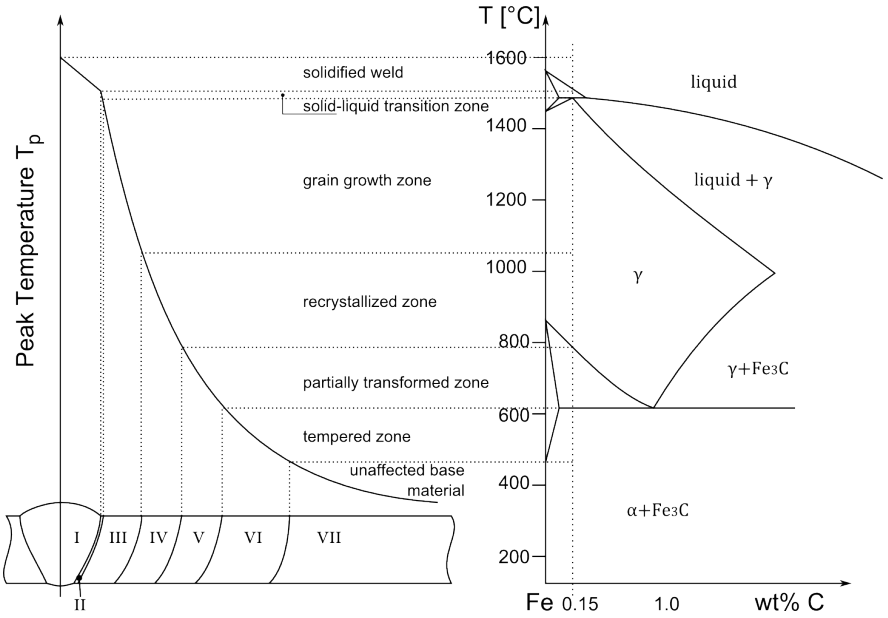

Figure 2.2: A schematic diagram indicating the different sub-regions of the heat affected zone of a transformable steel, adopted after [9]. Each region is linked to the corresponding phase area in the phase diagram based on the peak temperature it experiences. The phase diagram as well as the heat affected zone do not reflect the real dimensions but the non-scale illustration was chosen for the benefit of clarity.

I (Solidified weld): T>T_m, the transition L+$\delta \rightarrow \delta + \gamma$ causes at first the segregation of those alloying elements with reduced solubility in ferrite (f.e. C, Mn) at the liquid grain boundaries. In the next step the enriched liquid grain boundaries transform to austenite and at lower temperatures to martensite due to the higher C-content (beginning of martensite temperature is lowered with an increase of C [10]). The maximum increase in grain growth occurs at initial stages [9] and thus the grains near region II are larger than the inner grains which solidified later. The solid-liquid interface and the related heat dissipation process lead to an equiaxed dendritic structure. High welding speeds promote dendritic growth due to supercooling of the melt.

III (Grain growth zone): T $\gg$ A_{C3}, this zone is also referred to as coarse grained HAZ (CGHAZ). The high peak temperatures induces the nucleation of delta ferrite and the coarsening of austenite grains due to the dissolving of precipitates. A martensitic structure is formed during the cooling cycle leading to an increase of strength and hardness accompanied by a decrease in ductility and toughness.

IV (Grain refined zone): T >A_{C3}, this zone is also often referred to as fine grained HAZ (FGHAZ). On the one hand the low peak temperature does not dissolve all precipitates completely but on the other hand, the time period spend in the austenite region during the heating cycle is small leading to small austenite grains. These small austenitic grains preserve a large grain boundary network which serves as a nucleation site precipitates during PWHT and for pores during creep. The high cooling rates lead in the most common cases to the non-diffusional transformation of austenite to martensite.

V (Partially transformed zone): A_{C1} <T <A_{C3}, this zone is also denoted intercritical HAZ (ICHAZ). The temperature range between A_{C1} and A_{C3} only leads to a partial $\alpha \rightarrow \gamma$ transformation during heating. New austenite grains nucleate on prior austenite grain boundaries or martensite lath boundaries [11]. Depending on the cooling rate a wide range of possible structures is obtained. For the alloy discussed in this work, the transition $\gamma \rightarrow \alpha$' (fresh martensite) is performed while the untransformed martensite is tempered a second time.

VI (Tempered zone): T <A_{C1}, there is none phase transformation due to the relative low peak temperature (<A_{C1}). The microstructure is tempered, but maximum temperature is usually above the temperature of a post weld heat treatment. The tempering may promote the coarsening of precipitates.

VII (Unaffected base material): No major microstructure changes can be observed in this region. The total width of the HAZ starts at the inner borderline of the solid-liquid transition zone and ends at the border to the unaffected base material

2.4 Creep Resistance and Cracking Mechanisms

The plastic deformation dependent on time and temperature of material caused by a load, is called creep. A material experiencing a constant load at a homologous temperature (T/T_m) of $\approx 0.3 - 0.4$ leads to an elongation of the material with time. The creep deformation requires a minimum homologous time since heat resistant materials are characterised by a high bond energy and counts among the visco-plastic processes.

2.4.1 Phenomenology

The creep-induced deformation of a material passes three stages which are illustrated in the strain-time-curve in Fig. 2.3. The curve does not start at zero strain since the application of a load results in a time-independent instantaneous strain ϵ_0 which is composed of an elastic and plastic part. The following short description of the different stages refer to the Roman numerals in Fig. 2.3.

I (primary creep) The strain is slowly increasing while the strain rate $\dot{\epsilon} = d\epsilon/dt$ strongly changes and usually decreases [12]. The deformation leads to the generation of dislocations which cause a hardening increase and which is the reason for the decrease of $\dot{\epsilon}$ at constant stress.

II (secondary creep) The dislocation density is not increasing arbitrarily, because higher temperatures also allow recovery processes where dislocations glide and annihilate. The annihilation is facilitated when the distance between two dislations is small, hence the dislocation density is high. The equilibrium established between these two competing processes results in the stationary creep behaviour in this region. It is worth noting, that this assumption is only valid if the microstructure and consequently the applied stress do not change.

III (tertiary creep) The strain rate increases again in this regime, leading to the fracture of material. This stage is further characterised by a massive inner damage

and large total pore volume which causes a severe reduction in cross-section. The smaller cross-section is then the reason for the rise in strain rate.

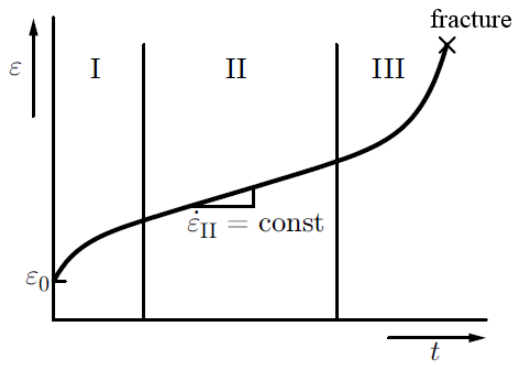

Figure 2.3: Schematic illustration of the change in strain with time upon constant load, after [10].

2.4.2 Creep and Failure Mechanisms

The above described stages of the creep behaviour are based on different creep mechanisms which in turn are determined by the temperature and stress applied. In the following paragraphs, a summary of the creep mechanisms involved on a microscopic scale is provided. For a very detailed discussion of this topic it is referred to [12–14].

Dislocation Creep

At temperatures in the order of the homologous temperature, dislocations are able to overcome precipitates by the accumulation or emission of lattice vacancies [12]. This behaviour is known as dislocation glide. Thus the strain rate depends on the ability of the dislocations to send out or accumulate vacancies. Furthermore, some dislocations serve as a sink while others serve as a source for vacancies and this results finally in a vacancy current density. The magnitude of this current density is the determinant factor for the strain rate.

Consequence I: Temperature and stress level mainly affect the vacancy diffusion which is the principle of this creep mechanism.

Diffusional Creep

Vacancies are formed at grain boundaries whose normal is parallel to the direction of tension, and which subsequently migrate to grain boundaries whose normal is perpendicular to the tension or experiences a lower tension. The transport of material

is opposite to this process which is also known as Nabarro-Herring-Creep. This creep mechanism occurs especially at lower tensile forces while at higher tensile forces dislocation creep is dominant. In addition to that, smaller grains enhance the process because the diffusion length –the grain diameter – is reduced, and also diffusion along the grain boundaries is possible.
Consequence II: Large grain diameters are preferred of two reasons: the diffusion length in case of volume diffusion is increased and the number of diffusion trails is reduced in the case of grain boundary diffusion.

Grain Boundary Sliding
The diffusion along grain boundaries as described above, is followed by a change of the grain's shape and leads to grain boundary sliding. This mechanism does not contribute much to the overall creep behaviour of a metallic material. Nevertheless, the glide of a grain boundary towards a grain boundary triple point may lead to a stress overshoot and cause fracturing of the boundaries this way.
Consequence III: Grain boundaries which are more resistant to sliding hinder the diffusional creep and reduce the risk of fracturing.

2.4.3 Concepts for the Development of Creep Resistant Alloys

The above consequences can now be summarised to a general "recipe" for the alloying concept of heat resistant steels where different base material are possible such as Ni-base, Cobalt-base or Iron-base. Briefly outlined, the following assumptions are stated:

- The formation of vacancies shall be complicated. This requires a high vacancy formation enthalpy which can be further related to high bond energies and even further to high melting temperatures.
- When a vacancy is formed, its diffusion shall be hindered. This demands that the energy barrier, which needs to be overcome by an atom willing to change its place with a vacancy, is high. The migration vacancy enthalpy is higher in dense crystal structures such as fcc or hcp.

- A coarse grain structure is preferred. It elongates the diffusional paths and reduces the strain rates.
- An oriented grain structure, that means the grains are elongated parallel to the direction of tensile, reduces shear stresses along the grain boundaries. A single crystal structure is the optimum.
- Especially at higher stress levels, the migration of dislocations greatly contributes to the plastic deformation. All mechanisms used for the hardening process can be used, where the thermal stability of precipitates is crucial. Grain-refinement has to be excluded since it enhances grain boundary diffusion (see above). The second exclusion is hardening by deformation which would lead to a recovery process in the first stage (primary creep) and thus to a loss of hardness.
- Solid solution hardening using alloying elements with high melting temperatures is a preferable option. Dispersion hardening may also give a good creep resistance due to the attractive force between particle and dislocation which pins the dislocations.

The desired effects are generated by choosing the proper alloying elements with regard to the base material. For Iron-based heat resistant alloys, the common alloying elements and their respective role are listed in Tab. 2.1. The addition of Boron enhances the formation of borides and plays also an important role in the case of type IV cracking (see below) [8]. An overview of the precipitates formed and relevant for the mechanical properties of 9%Cr steels is provided in [15]. Besides the aim of the alloying elements to increase the creep strength the alloy usually has to fulfill further requirements. In case of the material investigated in this work, also corrosion resistance is among those requirements. Chromium will promote the formation of Cr_2O_3 on the external surface of the material and is the principal element for hot corrosion resistance [8].

2.4.4 Selected Damage Mechanisms in Creep Exposed Welded Joints

The creep rupture is determined by its intergranular character, the material mainly gives way at the grain boundaries [12]. The damage of the grain boundaries is caused by the generation of pores and microcracks. The types of pores can be distinguished between “cavern pores” and “key pores”. The former are of a globular shape and are build at grain boundaries exposed to an external tensile load (see Sec. 2.4.2). The en-

ergy required to form small pores is higher, therefore the pores do form at later stages in the creep process. In addition, the pore formation is brought forward by high temperatures, long time periods and local stress concentrations (f.e. due to precipitates along the grain boundaries) [12]. Key pores develop by grain boundary sliding and cause a fracturing at the triple point of the grain boundaries. This process is typical for high stress levels. Both pore types finally lead to a reduction of the supportive cross-section, the resulting stress overshoot promotes a quick rise of the strain rate in the tertiary creep regime until the collapse of the material.

When it comes to welded parts, additional failure mechanisms should be taken into account with regard to the present heat affected zone. Schüller et. al have identified and categorised four main damage mechanisms in weldments of heat resistant steels which are indicated by the Roman numerals in Fig. 2.4. Types I-III are related with the welding process itself and potential post-treatment. They may be caused by the solidification process, hydrogen-induced or due to the post-weld heat treatment. This includes also temper embrittlement and sometimes long-term creep related cracks resulting from the mechanisms described above. [16]

However, type IV cracking has been exclusively identified as a cracking mechanism occurring after long creep durations. The cracking mechanism can be assigned to the outer region of the heat affected zone, next to the base material. This region can be further related to the intercritical and grain refined HAZ (see Fig.2.2). The type IV cracking has turned out to be the major nonconformity for weldments in power plants and occurs as well in ferritic/bainitic materials as in ferritic/martensitic 9-12% Cr steels. The reason for this mechanism is explained by the different creep behaviour of neighbouring microstructures in the HAZ. [11]

As described in Sec. 2.3, the temperature experienced by the grain-refined and the intercritical zone is not sufficiently high to dissolve all particles which can further coarsen during PWHT. Letofsky [6] also concluded, that the precipipitation of Laves and Z-phases and the related solid solution strengthener depletion as well as the dissolution of MX particles are nowhere else that pronounced as in this region [17]. Furthermore, as described in Sec. 2.4, the presence of coarse precipitates along the grain boundaries facilitates the generation of pores, since the local strain concentration is overcome by a gain in energy. TEM investigations showed a decrease in the dislocation density near the grain-refined zone which is caused by the recovery process at higher temperatures. To sum it up, the type IV cracking can be related to the structural weakening of a heat affected subzone which has less creep strength than the surrounding HAZ [11].

Understanding the complex material behaviour leading to type IV cracking is essential in order to develop effective counteractions which will require the interaction of a

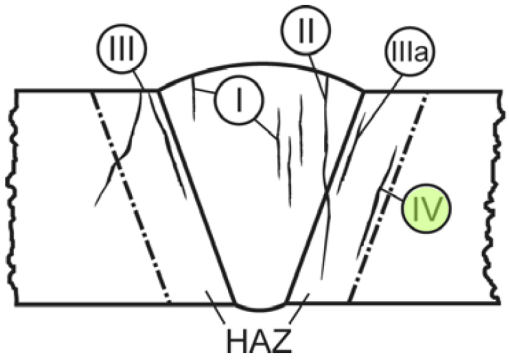

Figure 2.4: Modified illustration of different cracking modes identified in weldments of heat resistant steels, the important type IV cracking is highlighted in green, adopted from [2, 11].

creep resistant material with good weldability, a proper welding process and optimised welding parameters.

2.5 Martensitic 9Cr Steel Strengthened by Boron and Nitrides (MARBN)

Type IV cracking was identified as major cracking phenomenon in heat resistant steel weldments. As discussed above the 9-12% Chromium steels represent a compromise between the mechanical, thermal and econmical requirements for material used in thermal power plants. Researchers in Japan and to a smaller extent, also in Europe have been considering adding Boron (in the range of 90-130 ppm) to eliminate this type IV cracking [7] by suppressing the formation of the fine-grained zone [18–23]. An extensive investigation of the influence of Boron has been performed by P. Ernst [24]. Boron-induced precipitates improve the strength properties and curing. The atomic radius of Boron is smaller than Iron but larger than Nitrogen and Carbon [25]. The Boron atom is thus able to substitute Carbon atoms in carbides which increases the total amount of precipitates. The improvement of creep properties is assumed to be connected with the stabilisation of $M_{23}C_6$ carbides, and the slowdown of their coarsening rate [6, 7]. This stabilisation also leads to a stabilisation of the overall microstructure and increases thus the creep strength. The Boron addition lowers the weldability of steel [25], but with regard to the low amount alloyed, this may be a minor effect. The mission of Nitrogen is to extend and stabilise the γ-regime. Furthermore, Nitrogen in-

creases strength and the creep-resistant properties at elevated temperatures [25]. With metallurgical experience, Nitrogen will form together with Carbon carbonitrides which have a high thermal stability and will increase the mechanical properties. Another aim of Nitrogen, especially in Chromium steels, is to substitute Carbon which lowers the weldability [6].
Nonetheless, Nitrogen tends to form BN which consumes the majority of soluble Boron which is regarded as essential alloying element for the suppression of grain refinement in the heat affected zone. The reduction of Nitrogen to avoid BN formation is at the cost of VN which is among the desired precipitates. Semba et al. [26] discovered that a certain, but still small amount, of Nitrogen aids the precipitation of fine MX (like VN) but when exceeding a certain Nitrogen-treshold value, BN is formed. The optimum balance between N and B content together with an optimisation of welding parameters is of specific interest in the research community.

2.5.1 Welding of MARBN Steels

After MARBN steels have been identified as potential steels for use in thermal power plants, an investigation of the properties of the related weldments was self-evident. Investigations have been made both on conventional welding procedures such as gas tungsten arc welding (GTAW), manual metal arc welding (SMAW) and submerged arc welding (SAW) as well as on non-conventional welding processes like electron or laser beam welding. A comparison between the results using different processes is provided in [27]. The EBW procedures is still among the non-conventional methods for MARBN steels even if the principle applicability for 12%Chromium steels was already proofed in the late eighties [28]. A comparison between GTAW and EBW welded creep tested samples of 11%Cr steels yields very promising results for the EB weldments in view of creep strength [29]. In general, the conventional welding processes imply the utilisation of filler material which needs to be adopted to the desired weldment properties. The weld hardness is a topic, but which is manageable with a proper post weld heat treatment [27]. The high hardness obtained with EBW needs a more careful heat treatment design [28] since the combination with residual stress may lead to stress corrosion cracking [11].

3 Materials and Methods

The investigated materials as well as the major methods used for the experimental part of this work are briefly introduced in this chapter. Electron Beam Welding is one of the key aspects of this thesis, thus a deeper insight in the physical principles and advantages of this method is delivered. The relevant parameters and the specific experimental setup are described in more detail in the subsequent Measurement and Results chapter.
The evaluation of synchrotron data of creep-tested crosswelds of a MARBN steel builds the second big part of this thesis. Therefore, an introduction to the 3D-reconstruction methods and pore analysis is given in a separate chapter.

3.1 Materials and Preparation

Two different cast material plates both with akin chemical composition were provided within the framework of the KMM-VIN european network:

- material test plate; used for parameter optimisation
- weld test plate; used for "real" welding and characterisation of welds

An additional steel plate of unknown composition but with comparable thickness was used to gauge the welding parameter frame and are presented in the Appendix (A.3), though the steel plate will not be discussed in any more detail.

3.1.1 Material Test Plate (MTP)

A material test plate with the physical dimensions [275 x 155 x 25] mm (always denoted [width x length x height] here and in the following text) was provided by Goodwin Steel Casting Ltd. and is shown in the as-received state in Fig.3.1a. Though the exact composition is confidential, the chemical composition lies within the ranges given in Tab. 3.1. The entry NPM1 denotes the composition of the cross-welded creep samples investigated using SµCT. According to the delivery note, the plate was cast as part of the Goodwin air melt charge one (GAM 1 melt), but the as-received condition was not further specified. A quality heat treatment consisting of hardening and tempering as further described in Sec. 3.1.3 was applied. The machined surface of the plate did not require any further preparation for the welding experiments and so the plate was cut into samples:

- 1x small bar for basic characterisation
- 2x [130x150x25]mm plates for weld parameter study
- 1x tensile test sample with B8x40 geometry according to DIN 50125:2004-01.

The material test plate was used for an initial refinement of the welding parameters in view of material and thickness, since the available amount of the weld test plate was limited. An overview of the experimental workflow is given in Fig. 4.1, Fig. 4.2 lists the performed experiments and the related results are presented in the related sections of Chap. 4.

Table 3.1: Qualitative chemical composition of 9%Cr MARBN steels and of a known representative of the material group NPM1 in wt.%. The weld and material test plate's composition lie within the given range. The composition of the entry NPM1 is identical to the chemical composition of the creep tested samples investigated using CT.

	Cr	Co	W	Mo	V	Nb	B	N	Al	B+N
Maximum	8.9	3.2	3.1	0.1	0.22	0.11	0.0195	0.021	0.02	0.038
Minimum	8.6	2.8	2.5	0.01	0.19	0.06	0.009	0.015	0.005	0.0285
NPM1	9.3	2.9	2.8	-	0.21	0.06	0.012	0.013	<0.005	0.025

3.1.2 Weld Test Plate (WTP)

The actual material of interest for which the welding parameters shall be optimised is the weld test plate which, if so, is abbreviated with WTP. It was delivered in form of a bonnet casting from an eight tonne AOD melt by Goodwin Steel Casting Ltd. A stabilising heat treatment at 740°C for 12 hours was applied to the weld test plate after casting, and corresponds to the as-received state [30]. The chemical composition lies within the given range listed in Tab. 3.1.
Contrary to the material test plate, the surface of the weld test plate was still covered with a thick oxide layer due to the casting process. Especially the removal of the hard oxide layer was very time-consuming and required a slow feedrate. The remaining upper part of the initial ingot was used to machine other sample geometries, in total the ingot was cut into the following samples:

- 1x small piece of not precisely defined geometry for basic characterisation
- 4x [∼105x∼155x25] mm[1]: plates for electron beam welding
  - 2 plates were used for parameter study
  - 2 plates were used for the final optimised butt weld: one welded plate was used for characterisation and machining of tensile test samples, the second plate is foreseen for machining cross-weld creep samples
- 15 x [90x16] mm cylindrical samples for Gleeble heat affected zone simulation
- 10 x [10x4] mm cylindrical samples for dilatometer measurements

After a characterisation of the weld test plate in the as-received state, the quality heat treatment, as described in the following section, was applied. Other tests performed with the heat treated material are summed up in Fig. 4.2 and the related results are presented in the Measurements and Results chapter (Chap. 4).

3.1.3 Quality Heat Treatment(QHT)

In order to get the desired microstructure and mechanical properties, a quality heat treatment defined by the IMPACT project partners was applied [30]. The long annealing times compared to the plate thickness were matched with those appropriate

[1]Due to the machining process the length and width specifications for the 4 plates vary in the range of ±5 mm (indicated by "∼"), but the thickness is the same for all plates

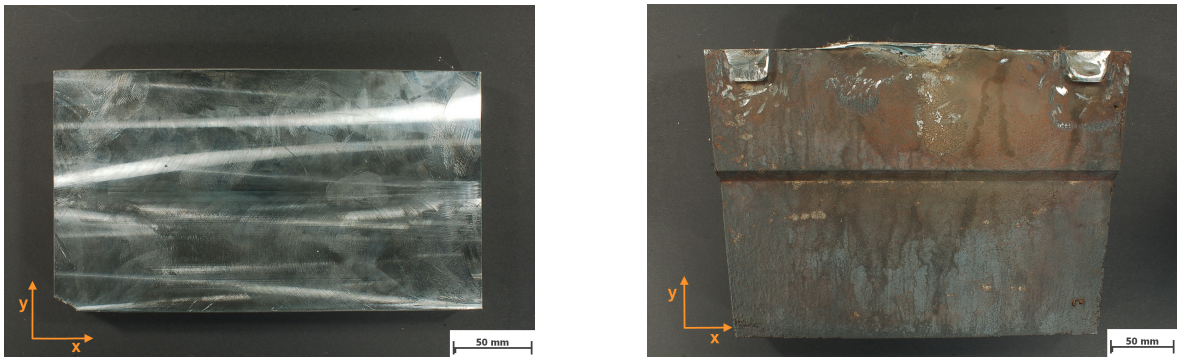

(a) (b)

Figure 3.1: Cast material test plate 3.1a and weld plates 3.1b in as-received state.

when annealing large castings in order to exclude any effect of the heat treatment on the later creep behaviour. The heat treatment was performed with a NABATHERM laboratory furnace of type HTC 03-14 with silicon carbide heating elements in ambient air and pressure.

The temperature sequence for the normalizing and tempering heat treatment for the material and weld test plates is given in Fig. 3.2. A thermocouple was welded onto the plate surface to monitor the temperature sequence. As already outlined above, the long holding time at 1200 °C was matched with the industrial heat treatment process and caused a thick oxide scale, up to 6 mm, and maybe also decarburisation (which was not further investigated). Although the weld point was protected with a ceramic paste, the growing oxide layer caused a drop-off of the thermocouple within the first three hours of the heat treatment.

The quality heat treatment comprises a solution annealing followed by tempering. The aim of the first part of the heat treatment is to dissolve the strategic alloying elements C, N, V and Nb in view of the later microstructural design of the alloy [10].

The present alloy was designed as air hardening steel which means that the critical cooling rates are lowered while the beginning of the martensite temperature is raised, and thus no quenching was required to obtain the desired martensite structure. The morphology of the martensitic structure is directly linked to the prior austenite microstructure from which it arose. A fine-grained austenitic structures offers a refined and homogenous martensitic morphology. This effect is caused by a higher number of possible nucleation sites for the martensitic crystals within the austenitic grain [31]. After the upper critical cooling rate is overrun, the further martensite formation is promoted by a sufficiently high supercooling which also leads to a high defect density (formation of twins, dislocations, stacking faults) [10]. However, given the fact that

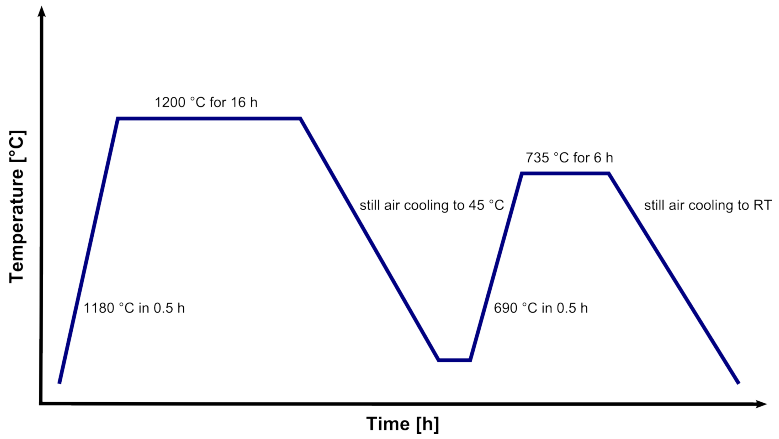

Figure 3.2: Schematic of the applied normalising and tempering heat treatment

the test plates are very small compared to the actual size of parts they represent, and the holding time at elevated temperature was quite long, the finally obtained grains were not fine.

The cooling performance in the furnace can be approached according to Newton with an exponential decay. Since the sample would stay at temperatures below 200 °C for a time sufficiently long, due to the low cooling rates in the lower temperature regime, where no critical structural changes are expected, it was therefore decided that no holding time at 45 °C is required. After the material was cooled down to 45 °C by static air cooling in the furnace it was heated up again to 735 °C for tempering. This part of the heat treatment is crucial in order to obtain the long-time mechanical properties at elevated temperatures which is demanded for the creep resistance. The high defect density generated during the cooling process, is the driving force for the dislocation recovery during the subsequent tempering process leading to a stable dislocation substructure. Moreover, the defects also serve as a nucleation site for precipitates such as $M_{23}C_6$ or MX.[31]

The tempering temperature is usually chosen to be above the in-service temperature but below A_{c1} in the case of components with long service lives [31]. The furnace control was programmed to stop at the end of the 6 h tempering process and the furnace door was opened to promote the cooling of the plates. The thick oxide layers were afterwards removed by machining.

3.2 Welding-related Experiments

3.2.1 Electron Beam Welding (EBW)

All welding experiments, i.e. blind welds and joint welds, were performed by means of electron beam welding (abbreviated with EBW in the further text), thus a more in-depth discussion of the process principle and the parameters influencing the welding results is given.
The overall machinery of an EBW installation is comparable to that of a scanning electron microscope since the aim in both cases is to generate a focused electron beam. But they obviously differ in the energies involved and consequently in the effect of interest caused by the beam-sample-interaction. While the SEM is dealing with the detection of generated particles such as secondary electrons or X-rays for the image formation, the EBW process uses the heat generated by the non-elastic interactions of the incident electrons with the sample as heating source for welding.
In very simple terms, the electrons colliding with the sample's bulk atoms transfer parts of their kinetic energies to the electrons which further exchange these energies with the lattice phonons. An increase of the lattice vibrations - characterised by the phonon energy - is equivalent to a raise in temperature. Starting lower power densities, the temperature rise is adequate to reach the melting temperature and melt the metal. It is important to note that the metal is vaporised likewise due to the low pressures in the vacuum mode of the EBW process. The weld pool at low power densities is broad and not of high depth and thus this is not the conventional mode of operation.
At higher power densities ($>10^5$ W/cm^2), the melting and sublimation of the material results in the formation of a keyhole whose shape is mainly determined by the electron momentum, the vapour pressure, and the surface tension of the surrounding molten material. The keyhole itself is filled with the metal vapour, ions and surrounded by a molten zone [32]. The beam traverses the component and melts the material at the leading edge of the beam, which hereafter solidifies at the trailing edge as shown in Fig. 3.3. It is worth noting that not all electrons contribute to the melting/sublimation of the metal and several secondary processes occur alongside as for example the generation of x-rays, secondary electrons, secondary ions or thermal electrons.
Considering the speed of the dominant process, the creation of the keyhole can be regarded as instantaneous and is indicated by the yellow shaded area in the figure while the dotted cone illustrates the surrounding molten zone. When the beam is moved at a constant velocity, the molten material is transported (see the black and green arrows

in Fig. 3.3) on each side to the rear front of the beam where it solidifies. The heat transfer processes involved (highlighted in red color font color) are the heat conduction to the ambient base material, the convection due to the bath agitation, and the thermal radiation from the surface.

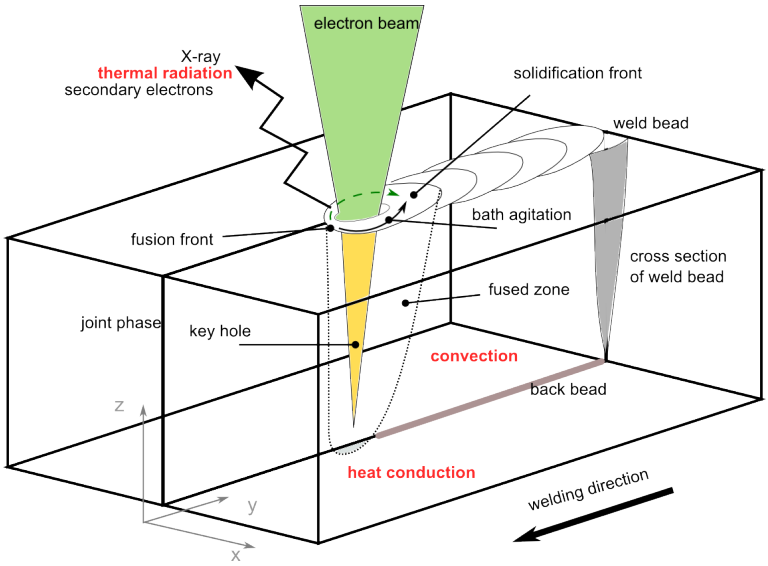

Figure 3.3: Schematic illustration of the weld formation process. The involved heat transfer processes are highlighted in red.

Advantages and Limitations

The finally obtained weld seam is mainly manipulated by the power density and the beam orientation, which in turn depends on the acceleration voltage, beam current, lens current, and welding speed. Furthermore, it is possible to deflect, split and oscillate the beam which allows to create beam figures in order to control the energy input adapted to the requirements of the given material.
The EBW process allows to set and vary these parameters not only statically but also dynamically during the welding process, a block diagram for the closed feed-back loop of a modern EBW plant is given in Fig. 3.4. This gives a high degree of freedom and permits the welding of components with complicated design, dissimilar materials, or materials with difficult weldability.
The manifold advantages like the minimal heat input, the small HAZ, and the low thermal distortions are contrasted by the prevalent economic aspects like relative high asset costs, extensive joint preparation and limitations due to the working chamber in view of size and evacuation time [33]. The high penetration depth allows to weld

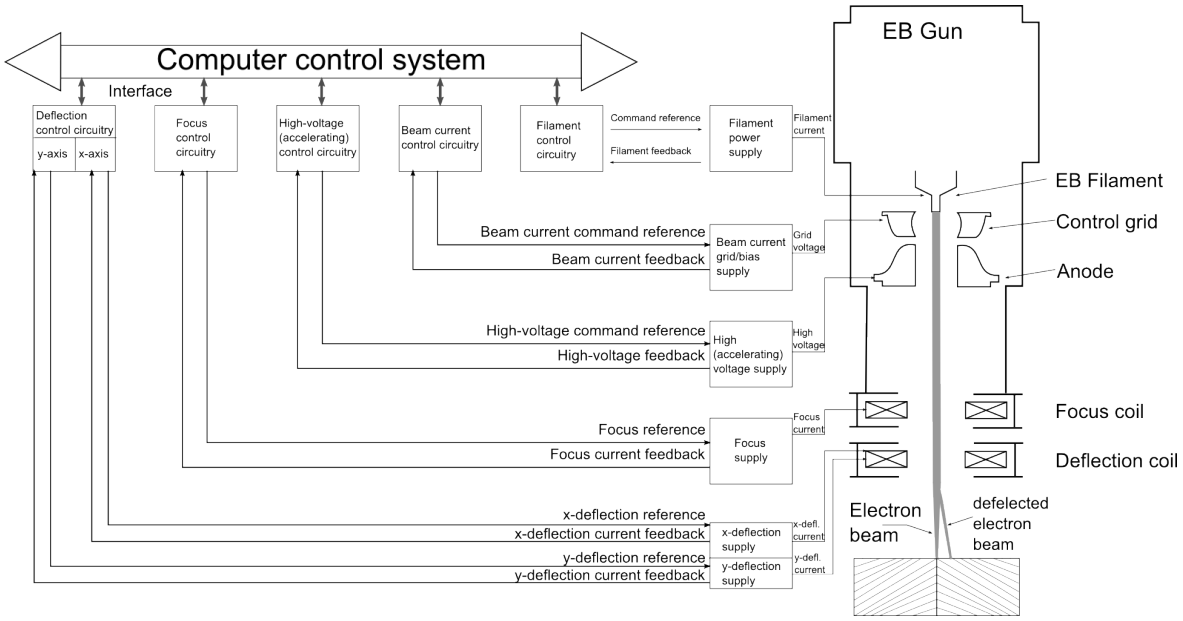

Figure 3.4: Block diagram showing a typical modern closed-loop gun control system (EB...electron beam) adopted from [33]

thick-walled components in a one step, then again also very thin materials can be welded. The size of the parts is also limited by the size of the vacuum chamber, where a larger size of the recipient requires more time for the creation of vacuum. So, the welding itself – when the required parameters have been determined before – is very fast, but the overall process is time consuming. Especially the complex interrelationships between the individual process variables as well as the sophisticated equipment demands extensive pretests. Therefore, electron beam welding is mainly used for high performance parts where quality and integrity is an essential target.

For none of the welding experiments performed any filler material was used and thus the metallurgy of the weld pool could not be actively influenced. This also means that any evaporation of the alloying elements is not compensated [34]. In many cases the effect is negligible due to the small volume of the weld pool or due to a minor impact on the properties of the welded part. Nevertheless in some cases the evaporation should be taken into consideration. For many elements, the vapor pressure at the melting temperature is higher than the working pressure in the EBW chamber. The vapor pressure for some common alloying elements as a function of temperature is given in App. A.7. It is recognized that elements with a high vapor pressure at the melting temperature tend to outgas which leads to a local depletion zone and pore formation in the molten zone [34]. For the present material, any dissociation of precipitates containing B or N would also cause a loss of boron and nitrogen which both have a high vapor pressure in their elementary form. As B and N have both been identified as essential for the

alloying concept in the case of MARBN steels, a degassing would thwart these efforts.

Joint Preparation

The IWS provides a PRO BEAM electron beam chamber machine of type EBG 45-150 K14 with which all experiments for this work were performed. The relevant adjustments and parameters are listed in the related section in the Measurement and Results chapter.
As the electron is a charged particle, it experiences a force when entering a magnetic or electric field. Thus, magnetic materials need to be degaussed in order not to deflect the beam during the welding process which would lead to incomplete fusion or fusion defects. The material itself but also clamping systems or installations within the chamber should be degaussed or made of non-magnetic materials. The recommended threshold value is defined with 1 Gauß (0.1 mT) [34]. For this purpose, the material is transported on a flat conveyor with constant and low speed through a strong alternating magnetic field. The breakup of the magnetic domains leading to a reduction of the remanent field is optimal when the directions of the external and internal fields are aligned. In practice this means, that the sample needs to pass the demagnetization device several times and with different orientations. Besides the strength of the applied alternating magnetic field, also the frequency plays an important role. The penetration depth of the field is directly linked with a permanent and fully demagnetization and depends on the frequency and the sample thickness. In very general terms, lower frequencies should be preferred. The thickness of the weld test plates allowed to use a frequency in the order of the American mains frequency: 60 Hz. Four to five passages proved to yield a satisfying demagnetization for the present material and geometry.
The surface quality determined by the roughness of the workpiece should be around $R_E = 1.6$ µm to max. 3.2 µm. All plates were ground on the upper and lower sides, the contact surfaces also ground with special care to the parallelism of the joints. Furthermore, the joint preparation comprises a cleaning of the seam zone to achieve an area free of oxides, grease, and oil. Cleaning and degreasing was done using acetone and followed the recommendations of the directive DVS 3213 [35]. The cleaning area shown in Fig. 3.5 was met. For the EB weld experiments itself no pre-heat or special weld preparation was postulated. As for all welding processes, special care has to be given to the design of the weld geometry. The shrinkage due to the solidification induces stress and can therefore lead to buckling, or in the worst case, lead to cracks. A good intro-

duction into the design considerations for EBW welds is given in [36]. For all welding experiments a clamping system was used and the plates for further butt welding were also tack welded at the end planes. The temperature was tracked with three thermocouples of type K welded at different postitions relativ to the central fusion line as shown in Fig. 3.6 to relate the thermal gradient to the obtained microstructure.

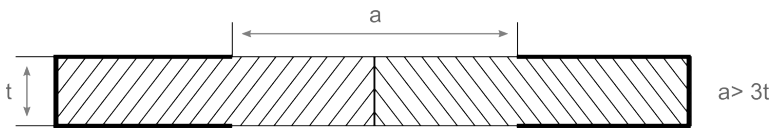

Figure 3.5: The recommended cleaning area (a) should be three times the plate thickness (t) as a minimum [34]

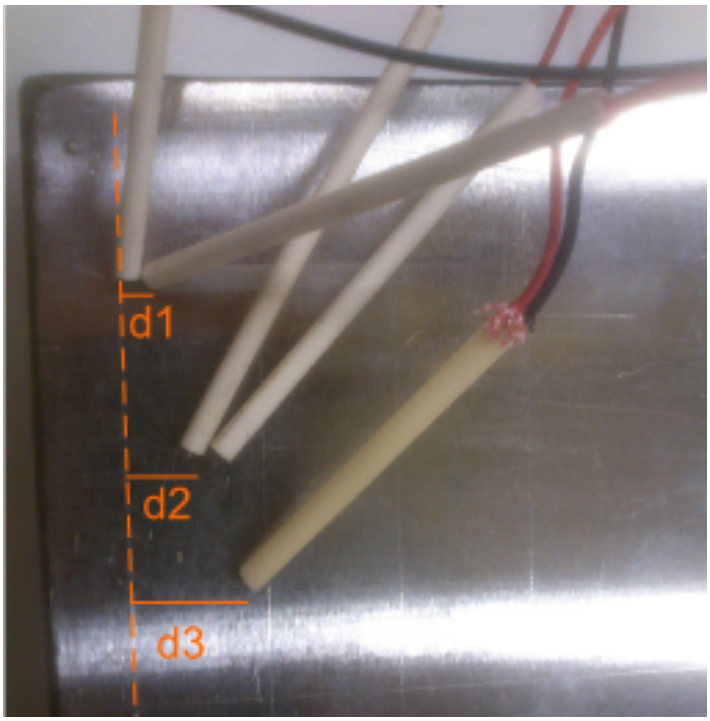

Figure 3.6: Three type K thermocouples were spot welded at different positions relative to the weld central line indicated by the dashed line. The distances were chosen to be as close as possible to the bead: d1 $\approx$ 3mm, d2 $\approx$ 3.5mm, d3 $\approx 4 - 4.5$mm

Optimising Parameters

The parameters influencing the final weld seam are kept constant or regarded as constant respectively while some are varied statically or dynamically. Tab. 3.2 presents an overview of the parameters and their influence on the welding process.

Table 3.2: Process parameters for EBW and their influence on the obtained weld. The column c/v indicates if the parameter is kept constant (c) or variable (v).

Parameter	**c/v**	**value**	**influence**
accelerating voltage	c	120 kV	determines the kinetic energy of the electrons and therefore the line energy, the beam spread angle decreases with higher voltages and thus the emittance is increased
beam current	v	59 - 70 mA	the beam current is determined by the filament current, a high beam current increases the line energy but also the beam diameter
slope-in / sloupe-out	c	5 mm	this is the length along which the power density increases/decreases to its maximum value, helps preventing excessive weld convexity
beam modulation figure	c	circle	determines the distribution of the line energy on the workpiece and thus the shape of the weld, many different geometries are preinstalled, but can be freely modified
beam figure amplitude	c	0.5 mm	amplitude in x and y-direction, in case of a circle x = y
beam oscillation	c	600 Hz	improves the fusion and solidification process, increases the diameter of the keyhole, prevents the liquid walls from collapsing and allows gas porosity to rise and escape, root spiking is reduced likewise [37]
filament current	c	about 46 A	depending on the cathode material and geometry, the filament current generates the required temperatures for the desired beam current
Focusing lens current	c	2602 mA	determines the focal spot size, focal length, process stability and focus position. It is crucial for the penetration depth, focus was adjusted to the sample surface, a modification to under- or over-focused mode can be used for preheat or smoothing
Welding speed	v	8 -10 mm/s	is inversely proportional to the line energy and determines the shape of the isothermal curves around the heat source (see Fig. 3.9), also influences weld quality f.e. weld porosity
working pressure	c	$\approx 3 \cdot 10^{-}4$ mbar	influences the beam diameter and divergence by scattering processes, a low pressure is favorable, also influences the vapor pressure curve of the alloying elements

The usage of a clamping system assured a constant operating distance (distance between height of sample surface and sample stage) of 9.8 mm.
The adjustement of the beam is the crucial part for obtaining weldments of high quality. The software for monitoring and control of the pro-beam EBW plant supports automatic beam adjustment. The result screen of such an adjustment is shown in Fig. 3.7 together with a pseudocolor illustration of the beam profile. A preferably round and narrow profile allows for very high power densities. The working pressure in the chamber is about $3{\cdot}10^{-4}$ mbar and thus in the order of high vacuum.
The optimisation process consists of two steps:

1. determine the line energy ($E = (U \times I)/v$) necessary to reach the desired welding depth by varying the beam current and the welding speed

2. fine-tuning of the above variable parameters (I,v) to eliminate irregularities in the weld support by the altering additional variable parameters like beam oscillation, beam figure or focus point

The interrelation between the beam current and the welding speed is in general very complex and shows a very small adjusting tolerance. This may lead to an unexpected high impact of machining variables (such as thickness variations or surface roughness). One can counteract it in an active way by increasing the travel speed, beam current or oscillating the beam. [38]

(a) (b)

Figure 3.7: Screenshot of the result screen after the auto beam adjustement: the resulting beam profile is displayed in pseudocolor (a) together with the values defined for centering and stigmatisation (b).

Post Weld Heat Treatment (PWHT)

The post weld heat treatment (PWHT) conditions are also pre-defined by the project to allow comparable results from the different project partners involved. The design of the PWHT is based on the past experience in comparable cases of the project. The required post weld heat treatment sequence is shown in Fig.3.8 and was also performed in the NABATHERM laboratory furnace.

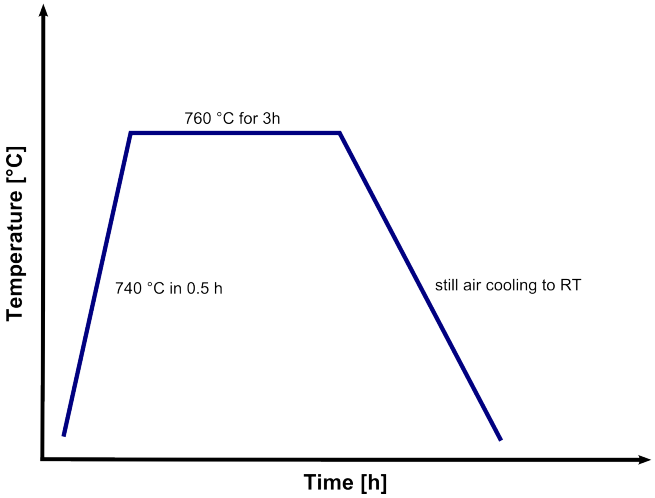

Figure 3.8: Schematic of the post-weld heat treatment for the welded and HAZ simulated samples.

3.2.2 Physical Simulation of Heat Affected Zone

The high heating and cooling rates related to the EBW process result in a very narrow heat affected zone which is desired in the case of the final weld but is also a downside for the investigation of the different regions within this zone. The temperature profile characterising the welding process is schematically shown in Fig. 3.9.
A physical simulation of the welding process implies the application of a well-defined temperature profile on the specimen. The obtained microstructure at a certain isothermal plane is comparable to that obtained in the related welding process. The HAZ in question is enlarged and can be investigated in detail.
The Gleeble®-3800 basic system equipped with its digital control system provides a powerful tool to control the thermal and the mechanical test variables simultaneously throughout the applied cycle [39] and thus enables the physical simulation of the HAZ. The Gleeble QuickSim comes with a set of software tools including a HAZ simulation tool which allows to generate a thermal cycle according to the welding conditions in the real process. The heat transfer is taken into account via the selection of an appropriate model where one can choose among Hannerz, Rykalin 2D, Rykalin 3D and Rosenthal equations. A very detailed and extensive scientific treatise on the different models is provided in the literature [3, 9, 40, 41]. The Appendix App. A.6 provides a small overview of the parameters which need to be defined in the software including some screenshots.
The cylindrical shaped sample is clamped by two jaws and heated via resistance heating as outlined in Fig. 3.10 according to the thermal cycle specified in the HAZ simulation module of QuikSim software. The heating of the bulk sample is based on the passing through of a current with low frequency in order to obtain a uniform heating. The heat gain of the bulk materials is equal to the energy input due to the current flux which is defined by Joule's Law P=U·I, rearranging the equation applying Ohm's law U=R·I finally gives $P = I^2R$. The control of the resistance of the whole system is crucial in order to control the temperature profile in the sample. And thus the heating and the cooling rates can be influenced by choosing f.e. different materials for the jaws. Besides the material selection for the jaws, the contact length between jaw and sample should preferably be large to maximise the cooling rate. The finally achieved temperature cycle in the specimen is further influenced by the specimen cross section, the free span length and the desired peak temperature. The axial thermal gradient increases with the peak temperature and even more when the free span length becomes smaller.
Thus, the control of the thermal gradient is the crucial part of this physical simulation. In order to obtain a homogenous simulated microstructure at the center of the Glee-

ble sample over a length which can be easily accessed and investigated with the light optical microscope, high peak temperatures and a small free span length are required. In a first attempt, cylindrical samples with a diameter of 16 mm were used together with copper jaws. The choice of copper jaws further favors a high thermal gradient because of the high thermal conductivity of copper (which is the second largest after pure silver). Limited by the design of the jaw grip, a minimal free span length of 7 mm could be achieved. In addition to that, a good and close contact between the jaws and the sample was not given all-around the boundary surface. Since the required heating and cooling rates were not achievable in this setting, it was decided to reduce the specimen diameter to 10 mm. The altered sample geometry allowed the use of a different copper jaw pair which provided a better overall surface contact and furthermore the free span length was reduced to 4.8 mm.
It should be mentioned at this point, that in the temperature region of interest, the influence of the specimen diameter on the cooling rate is rather small if the free span length is too small and only becomes obvious when the free span length is increased [39].
The Gleeble HAZ simulation was now performed in order to simulate three different regions of the HAZ of the final EBW weld seam, each corresponding to a thermal cycle which was recorded during welding at diffent distances from the fusion line (see Fig.3.6). The chosen mathematical model for the heat transfer was Rykalin-2D which is based on the assumption that the plates can be regarded as "thin" and the heat transfer process is isotropic. Furthermore the heat source, i.e. the electron beam, is regarded as a line source which allows a dimensional reduction for the heat conduction to the 2D case. According to N. N. Rykalin [42] the heat conduction equation can be solved for this case and leads to the following temperature field:

$$T - T_0 = \frac{Q}{d\sqrt{4\pi kc\rho(t - t_0)}} \exp\left(\frac{-r^2 c\rho}{4k(t - t_0)}\right) \tag{3.1}$$

And thus the heat input causing the temperature field can be expressed as [39]:

$$Q = \sqrt{\frac{4\pi kc\rho\Delta t}{\frac{1}{(T_2 - T_0)^2} - \frac{1}{(T_1 - T_0)^2}}} \cdot d \tag{3.2}$$

where:

Q	...	energy input [J/cm]
c	...	specific heat [J/(g °C)]
ρ	...	density [g/cm^3]
k	...	thermal conductivity [W/(cm°C)]
d	...	plate thickness [cm]
T_0	...	ambient temperature, T = 20 °C
T_1,T_2	...	temperature defining the cooling time [°C]
t_0	...	pre-heat finish time
Δt	...	cooling time from T_2 to T_1 [s], $T_2 > T_1$

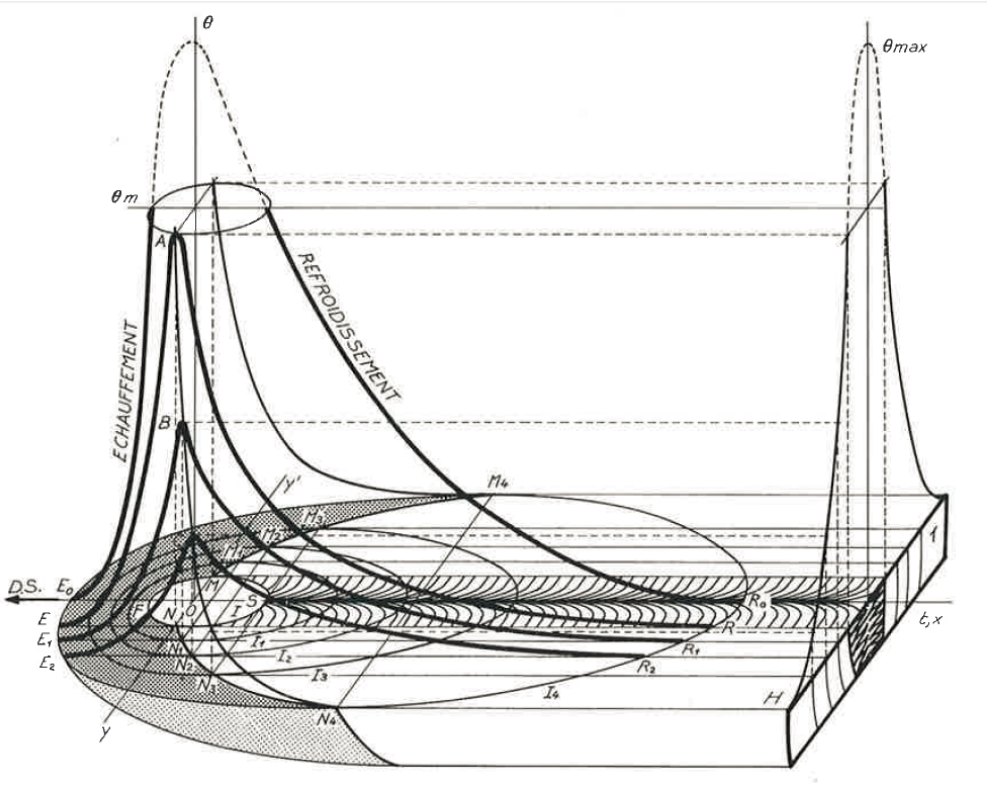

Figure 3.9: Three-dimensional temperature distribution and its projections. Note that the intense heat source and the heat sink of the welded material form a very steep temperature profile. The movement of the heat source results in bow-like curve for the different peak temperatures (Tp(y)) which piles up the isotherms at its leading edge. The projection in the T,y-plane shows the different peak temperatures experienced by the microstructure around the molten zone.Echauffement...heating up, Refroidissement...cooling cycle, figure adopted from [40]

The Gleeble now calculates the currents and times based on the Rykalin 2D model and the model-dependent parameters (a detailed description of the used parameters is given in App. A.6) in order to produce the desired temperature cycle. In total, three thermocouples were used as indicated in Fig. 3.10b. The central thermocouple is used

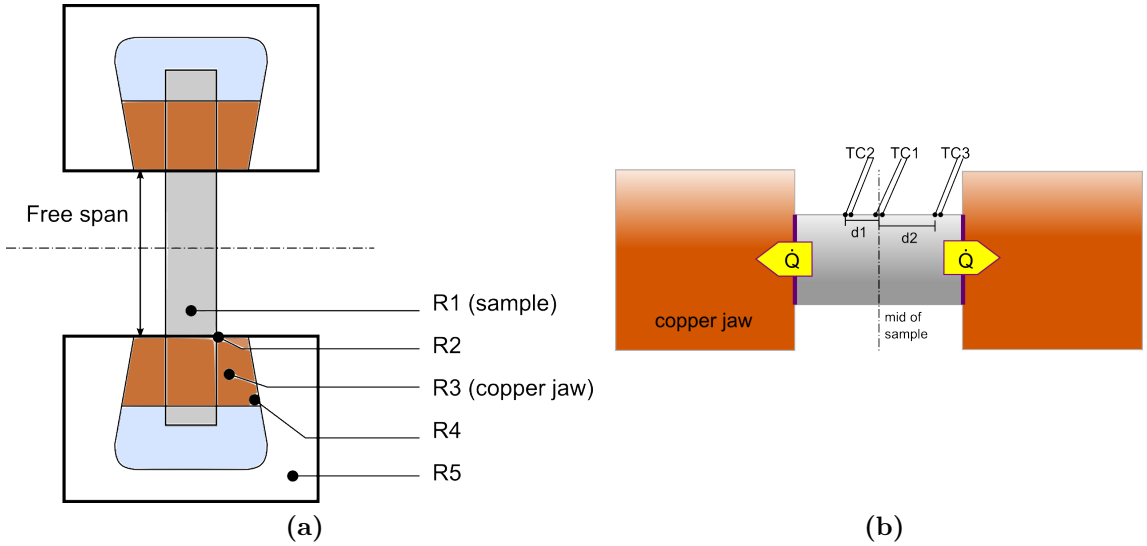

Figure 3.10: 3.10a: Electric resistance of the components in the electric heating loop which influence the bulk heat gain given by I^2R_E. Figure adopted from [39]; the light blue shaded areas indicate air, the brown shaded areas indicate the copper jaws. The position of the thermocouples is shown in 3.10b where d1,d2 are the distances from the central thermocouple and d2 >d1. The distance are in the range of 1.4 to 1.7 mm.

as controlling thermocouple in order to obtain the desired peak temperature. The other two thermocouples were used in order to record the thermal gradient at distances d1≈ 1.4 mm and d2≈ 1.6 mm from the center. The test is performed and the parameters which were previously defined among the acquisition variables are recorded. The data is then evaluated and plotted using Origin and Matlab. After simulation, one specimen was cut longitudinally in order to investigate the obtained microstructure. The other specimens were subjected to the same post weld heat treatment as specified in Sec. 3.2.1.

3.3 Characterisation Methods

3.3.1 Light Optical Microscopy

In order to investigate the microstructure of the materials, the regions of interest were cut-off of the sample and thermo-embedded. The surface of the samples was ground and polished afterwards with diamond paste to 1 µm, and in a few cases even vibrational polished to improve the etching process. A modified Lichtenegger's and Bloech's etchant (for more details on the composition and etching instruction, see A.1)

was used to reveal the microstructure of the materials while a standard Adler etchant was used to analyse the weld seams on a macroscopic scale.
The stereomicroscope Zeiss Axio Discovery.V20 allows a user-defined setting of the level of illumination and was used to document the macroscopic structure of the etched welds. For the study of the microscopic structure a microscope of type: Zeiss Axio Observer.Z1m was used. For the two microscopes as well as for the camera, the Axio Visio Software Package was used.
Larger parts, e.g., the weld plates in the as-received state, were documented with a Nikon D50 camera mounted on vertical travel rail. The precise determination of the vertical position, the magnification of the camera together with the sample height also allowed to specify a scale.

3.3.2 Micro Hardness

Hardness measurements were performed according to EN ISO 6507-1:2005. All hardness measurements were performed using a load 0.1 kg which is in the regime of microhardness. In addition these measurements were performed by means of Vickers which implies that the indenter is build by an equilateral diamond pyramid with an opening angle of 136°.
The hardness measurements were always performed on non-etched ground and polished base material or cross-sections of welded seams using wether the hardness testing machine EMCO TEST M4C 025 G3M or the EMCO TEST M1C 010. The former requires a manual sample movement and was used in case of little test points ($N \leq 20$) while the latter offers an automatic sample stage and was therefore used for hardness maps requiring a large matrices of test points (up to 750 test points were measured for some samples). The test point data matrices were further assigned to a color map and always one pixel between two single data points in vertical direction was interpolated. The measurement of the hardness on the cross section of the welded sample allows to monitor the hardness increase due to the welding process and to evaluate the influence of the post weld heat treatment. A discontinuous change of the hardness from the base material to the welded area would facilitate the initiation of cracks when the cross welded component is exposed to a (multi-axial) stress state.

3.3.3 Tensile Test

The tensile test provides information on the strength and ductility under uniaxial tensile stress. The material is machined to a well-defined geometry (specified in standards) with screw threads on both ends with which it is fixed in the vertical aligned sample holder. A good overview of the machine's components, the different specimen geometries and influencing parameters is given in ASTM E8M [43].
The base material of the weld test plate and the material test plate as well as the EB cross welded samples in PWHT condition were tensile tested at room temperature in order to investigate the strength of welds and the rupture location.
The tensile tests were performed with the testing machine Zwick/Roell TC-FRXXMOD type A1K. The sample geometry for all samples made out of the weld test plate in every condition was according to DIN 50125:2004-01 form B10x50, the material test plate in the as-received condition used a B8x40 geometry. The testing procedure for the samples tested at room temperature followed the requirement given in DIN EN ISO 6892-1:2009-12.

3.3.4 Dilatometry

Dilatometer measurements allow to investigate the sample length change as a function of temperature. The change in length can be either reversible due to thermal expansion or due to phase changes. For all measurements, a Bähr Typ DIL 805 A/D horizontal dilatometer available at the Institute was used together with cylindrical shaped samples with a diameter of 4 mm and a length of 10 mm. The sample is placed between two horizontal spring mounted silica stamps, which apply just as little force as necessary to keep the sample in the horizontal position. The complete set-up (stamp-sample-stamp) is shifted into a copper coil which heats the sample via induction heating. The type S thermocouples are welded parallel aligned on the horizontal center of the sample. The chamber is evacuated and allows high cooling rates through floating the chamber or forced cooling via a (noble) gas stream.
In total two different types of dilatometer measurements were performed: one was aiming at determining the austenitizing temperatures (A_{c1} and A_{c3}), and the other one to reproduce the EBW thermal cycle using the parameters as listed in Tab. 3.3. The high heating rate for the latter experiment exceeded the maximum sampling rate of the dilatometer electronics. The resulting dilatometer curve was very noisy and showed

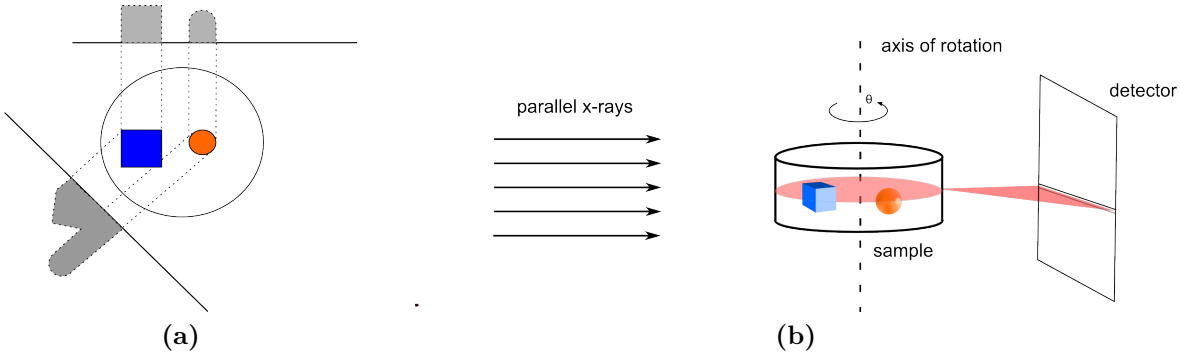

Figure 3.11: Basic principle of CT scanning 3.11b and image formation by 2D projections 3.11a. The resulting projections are dependent on the angle between the projection line and the object.

an oscillating trend which did not correspond to the actual material elongation, it was therefore not further evaluated.

Table 3.3: Dilatometer parameters for the different measurement set-ups. The measuring error of the thermocouple was taken from the specifications and is ±2.5°C up to 375 °C and $\pm 0.075 \cdot (T)$°C up to 1200 °C

T-cycle	ramp rate [K/s]	T_{Peak} [°C]	hold time [s]	cooling
near-equilibrium	$0.\dot{3}$	1100	180	free cooling
EBW-T-cylce	1000	1100	1	free cooling

3.3.5 Synchrotron-Microtomography

The word tomography has its origin in the ancient greek where *tomos* means "slice, selection" and *graphō* means "to write" and thus already conveying the idea of the measurement principle as a set of 2D projections of the specimen is recorded. The mathematical framework is based on the fundamental concept that an n-dimensional object can be reconstructed from its (n-1)-dimensional projections and was first described by Johann Radon in 1917 [44]. Considering the definition of the integral calculus, the projection of a 3D object on a 2D plane at a certain angle is given by the integration of its contour function which is schematically outlined in Fig. 3.11a. The computed tomography (CT) is now based on the generation of several 2D projections at different angles and a following reconstruction of the 3D object via a Radon transformation.
The 2D projections in turn are obtained by the interaction between an incident high-energy, low-divergence, monochromatic x-ray beam with the sample which is of two

kinds: first the beam intensity is attenuated by absorption processes and second it experiences a phase shift. The former interaction process is used for attenuation-contrast projections and the latter in the case of phase-contrast projections. The measurement set-up is illustrated in Fig. 3.11b. The beam source and the detector are installed exactly opposite each other, the sample is placed between them. If the axis of rotation of the sample is exactly perpendicular to the axis spanned by the incident beam (and the surface normal of the detector), always the same "slice" (indicated by a red oval in Fig. 3.11b) is projected on the same detector line. Many projections at different angles form the raw data for every pixel on a single slice. The height of one detector line can not be infinitesimal small and thus the slices consist of small subvolumes called voxels. In practice either the beam and detector move while the sample stands still (CT for medical application) or the sample is moving on a stage (as for the SµCT measurements presented in this work). The Radon transformation now allows to calculate back the intensity attenuation for each voxel leading to a grayscale image for each slice and the stacked slices represent the overall information for the whole 3D sample.
For obtaining information on the internal structures and geometries of materials (regardless of the material type) one desires a high resolution and high intensity at in a time-efficient manner. Beside this, the technique (as indicated in Fig. 3.11) requires a coherent parallel beam and since suchlike x-rays demand for a reactor or spallation source, one has to apply for beamtime at the available international sites. This method allows the non-destructive investigation of the internal features of sample while the high-flux guarantees for an excellent signal-to-noise ratio and high resolution. In the case of creep sample studies the analysis of the formed pore volume during creep and its distribution is of particular interest. The software-based reconstruction and volume rendering offers all these possibilities along with many powerful mathematic tools for further analysis.
The data analysed in this work was recorded at the SPring-8, Japan in 2011 with the approval of JASRI (Proposal no. 2011A1291). The sample material type is NPM1 (the chemical composition is listed in Tab. 3.1) and the samples were welded by a gas tungsten arc welding process using a nickel based filler metal (Nibas 70/20-IG) [45]. The welded samples have been uniaxial creep tested at 650 °C at different stress levels [70,80,100,130 MPa] until rupture. For the 3D damage investigations, specimen was extracted from the creep tested crosswelds as illustrated in Fig. 3.12. The figure also shows the size of the region of interest which was defined for the SR-µCT. In order to cover parts of the weld metal and the heat affected zone, three subsequent measurements with a small overlap were performed. The relevant material data and parameters are summarized as follows:

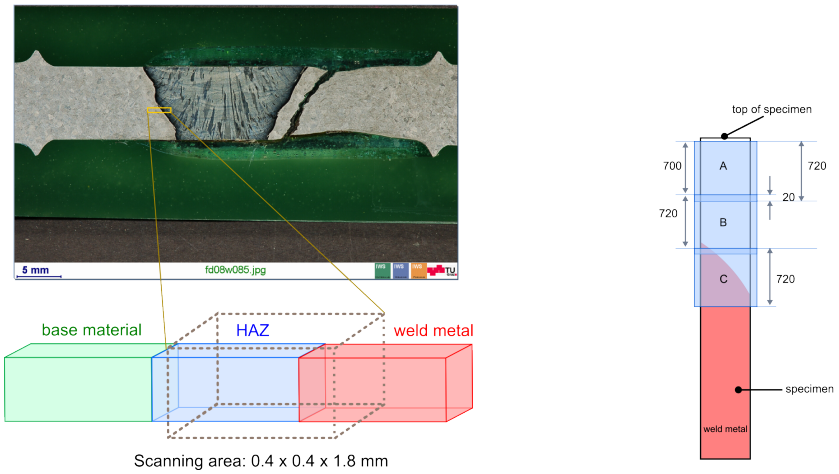

(a) **(b)**

Figure 3.12: The samples were extracted from the HAZ opposite to the crack (orange rectangle) and covered the weld metal and the HAZ region (3.12a). The CT data were recorded three times by shifting the region of interest (indicated by the blue rectangles) alongside the sample length while a small overlap was kept 3.12b. All sizes stated in drawing refer to micrometers (µm).

Energy :	37.7 keV
Distance sample-detector :	65 mm
Voxel size :	0.5 µm^3
Spatial resolution :	1 µm

4 Measurements and Results

This section provides the results of the performed experiments grouped into basic characterisation of the base material, welding studies and heat affected zone simulation. This experimental work comprises results for the material and weld test plate.

4.1 Characterisation of the Base Material

Two steels with comparable chemical composition (see Tab. 3.1, p. 18) were used in the framework of this thesis. The material test plate (MTP) was exclusively used for a prior blind weld and butt weld study, thus the characterisation of this material was

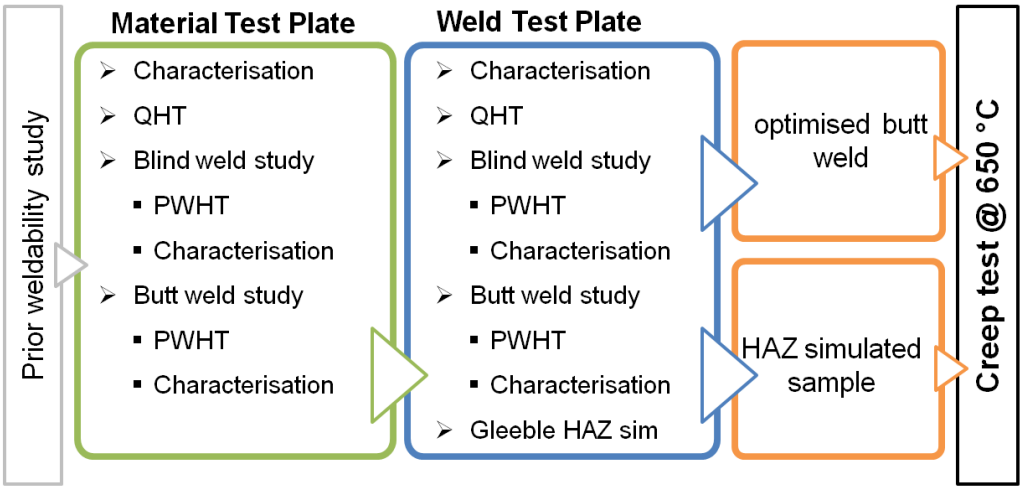

Figure 4.1: Workflow of the experimental part. The prior weldability study was performed at the Institute in October 2013 [46].

MARBN Material		EXPERIMENTAL WORK										
		Testing of Base Material					Weldability Studies		Welding	Testing of Weldments		
Name	condition	Tensile Testing @ RT	Microstructure Hardness Testing	Microscopy	Dilatometry	Weld simulation studies	Experimental welding trials	condition	VE	Tensile Testing @ RT	Hardness Map	Microscopy
material test plate	as-received		X	X								
	QHT	X	X	X			EBW blind welds	as-weld	X		X	X
								PWHT	X		X	X
							EBW butt welds	as-weld	X		X	X
								PWHT	X		X	X
weld test plate	as-received	X	X	X								
	QHT	X	X	X	X	X	EBW blind welds	as-weld	X		X	X
								PWHT	X		X	X
							EBW butt welds	as-weld	X		X	X
								PWHT	X	X	X	X

Figure 4.2: Overview of the experimental work carried out on the material and weld test plates in different conditions. VE...visual examination

reduced to a minimum. On the other hand, the weld test plate (WTP), which was the actual material for parameter optimisation, was investigated and tested in more detail. Both steel plates were characterised in the as-received and QT condition in view of microstructure and hardness. The weld test plate was also tensile tested at room temperature in both conditions (see Sec. 4.1). The experimental overview in Fig. 4.2 groups the performed measurements and experiments into tests for the non-welded and welded material in different conditions.

The microstructure of the polished sample in the as-received condition was investigated in the etched and un-etched condition. The latter revealed a high grade of porosity of the microstructure, as shown in Fig. 4.3. Since the gas solubility in metals decreases with temperature, a narrow solidification interval may lead to the generation of gas pores. Small gas pores also ascend slower and become entrapped by the solidifying material. The micrographs Fig. 4.4-4.7 show the microstructure of the etched test plates in the as-received condition with two different magnifications. The prior austenite grains are very large and the material contains a lot of pores. Due to the casting process delta ferrite is also present in both materials.

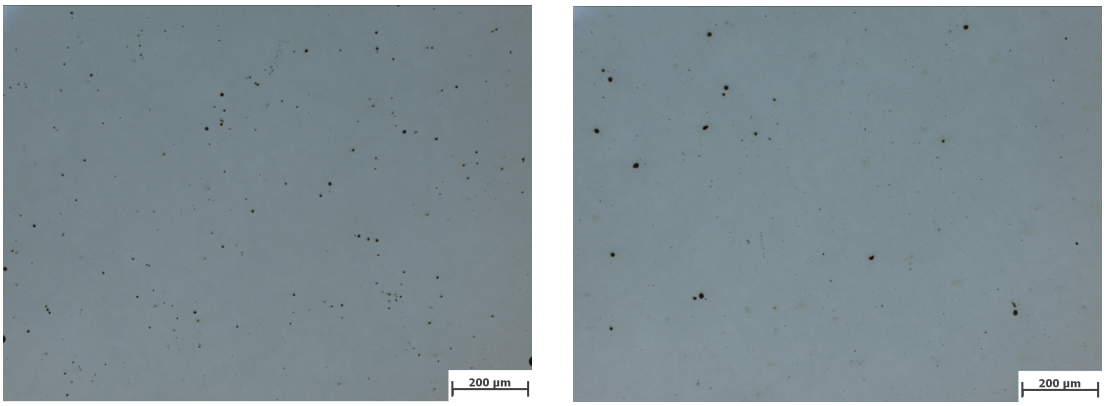

(a) MTP, as received **(b)** WTP, as received

Figure 4.3: Small entrapped pores in the two steels. The pore diameter is slightly larger for the weld test plate.

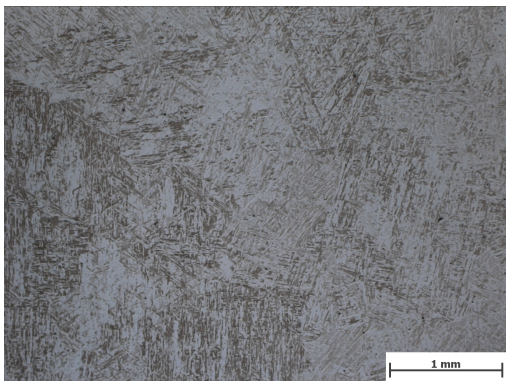

Figure 4.4: MTP, as received [Vilella]: martensitic microstructure, the prior austentite grain boundaries are not visible

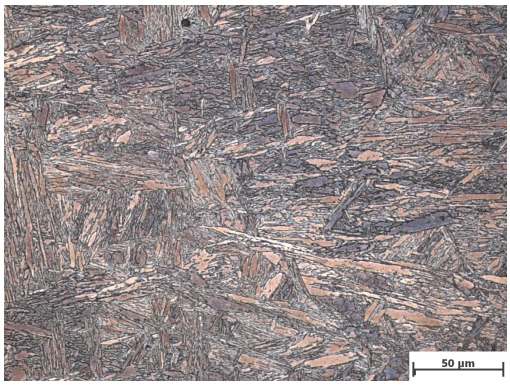

Figure 4.5: MTP, as received [Vilella]: the martensitic structure colonised by acicular ferrite

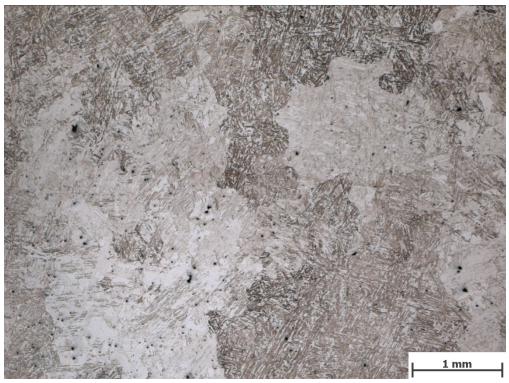

Figure 4.6: WTP, as received [Vilella]: martensitic microstructure, the coarse prior austenite grain size is partly indicated by different etched domains

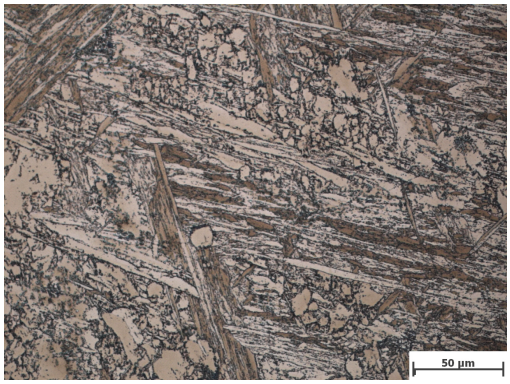

Figure 4.7: WTP, as received [Vilella]: the martensitic structure colonised by scattered ferrite

After the quality heat treatment as described in Sec. 3.1.3 on page 19, the samples were again ground and polished to generate a proper surface condition for further etching. In order to reveal the prior austenite grain boundaries etching is required and many etchants have been developed for this purpose. The ongoing research at the institute on 9% Chromium steels has already led to an improved etchant for the MARBN steels based on Lichtenegger's and Bloech's reagent. Nevertheless the etching process has proved very difficult and did not yield the prior austenite grain boundaries. Several other etchants have therefore been tested with variation of the etching condition, a detailed review of the etchants and the obtained micrographs is given in App. A.1. The micrographs for the QT microstructures are shown in Fig. 4.8-4.11. The prior austenite grains are definitely smaller than in the as received condition and no delta ferrite is visible anymore. The fine dispersed carbides align along the PAGB but also

on the marteniste laths. A comparison of the hardness measured in as-received and after QT for both materials is given in Tab. 4.1.

Table 4.1: Hardness of in the as-received state and after QT for both materials, (average of 10 test points, HV10), AR...as-received, QT...quality heat treatment

	AR	QT
MTP	431	249
WTP	271	261

The remarkable difference in the Vickers hardness of the two materials in as-received condition may be attributable to a heat treatment of the weld test plate. According to the delivery note, after casting, the weld test plate was subcritically annealed at 740°C for 12 h to stabilize the microstructure. The QT heat treatment allows to reset the thermal history of the microstructure and all future experiments were solely performed with the steel plates in this heattreated condition as the starting point.

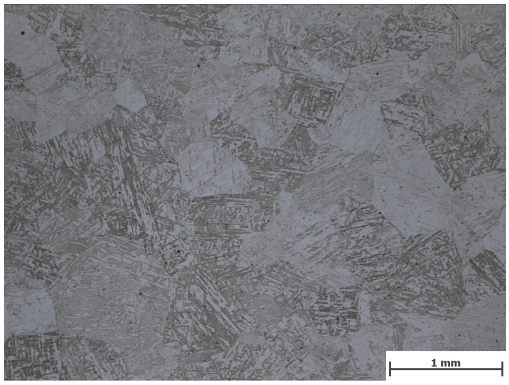

Figure 4.8: MTP, QT [Vilella]: tempered martensite characterised by lath packets, some of prior austenite grains are now well-defined and smaller than in the as received state

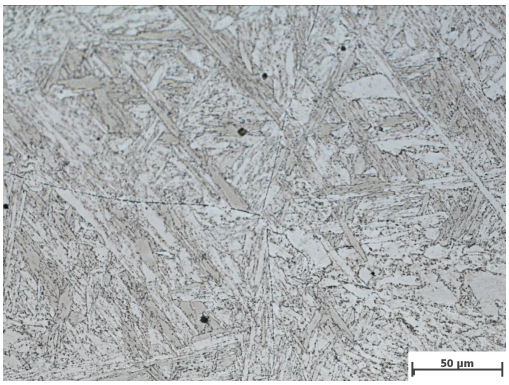

Figure 4.9: MTP, QT [mod. LB]: finely dispersed chromium carbides at PAGB

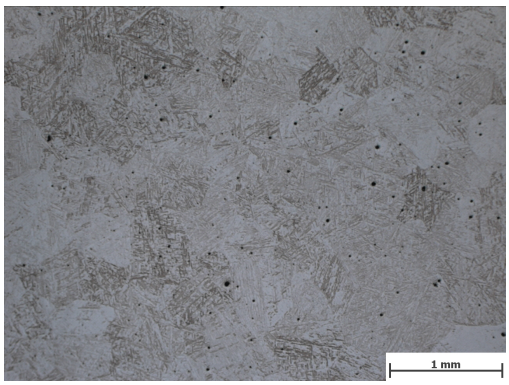

Figure 4.10: WTP, QT [Vilella]: tempered martensite structure, the etching attack does not allow to evaluate PAGB size

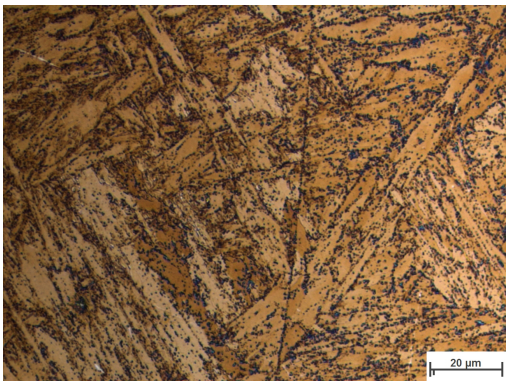

Figure 4.11: WTP, QT [Vilella]: martensitic matrix and fine dispersed precipitates

Tensile Test

The weld test plate was tested in the as-received and in the heat treated conditions, the material test plate solely in the heat treated condition. The tensile curves are shown in Fig. 4.12 and the related values are given below in Tab. 4.2. The material and weld test plate exhibit a comparable yield strength, but the tensile strength of the weld test plate is in any condition higher. The tensile curve of WTP in as received condition has the highest yield and tensile strength which may be correlated with the stabilisation heat treatment which was mentioned on the delivery note. However, the complete thermal history of the material in as-received state is unknown and therefore an interpretation or comparison with the QT weld test is not possible. It has to be noted that the premature failure of one of the heat treated weld test plate samples (black curve) was caused by an oxide inclusion. The characterisation of the inclusion can be found in App. A.4.

Table 4.2: Evaluation of tensile test at room temperature for material and weld test plate after QT. One sample of the weld test plate was also tested in as-received condition (ar).

sample	$R_{p0.2}$ [MPa]	R_m [MPa]	ϵ [%]
WPT-ar (blue)	707	826	17
WTP-QT (red)	654	787	17
WTP-QT (green)	640	778	17
WTP-QT (black)	636	773	15
MTP-QT (pink)	641	733	15

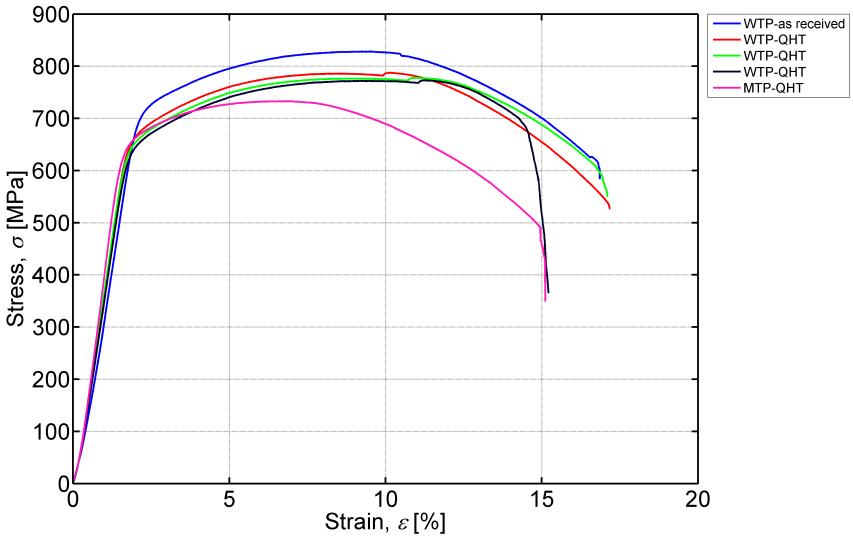

Figure 4.12: Tensile test at room temperature according to EN 10002-1

Table 4.3: Transformation temperature at low heating rates (0.3 K/s) and forecast calculated using Matcalc

	A_{C1}	A_{C3}	M_S	M_F
Dilatometry	846	887	384	260
Matcalc	805	833		

Dilatometry

A dilatometry test was performed to obtain the transformation points during heating and cooling with the parameters given in Tab. 3.3. The curve is shown in Fig. 4.13. The tangent method, where the beginning of a phase transformation is defined as the first point deviating from a fitting tangent, was used to determine the start and end of the transformations. The test was only performed for the weld test plate, results are given in Tab. 4.3 (all values in [°C], margin of error ±20°C).

A phase fraction diagram for the equilibrium condition in the temperature range from 400 to 1600 °C was also calculated using the software tool MatCalc for validation. Considering the finite heating time of the dilatometry and the margin of error, the above values are in good agreement with the forecast values. The phase fraction diagrams are listed in App. A.2.

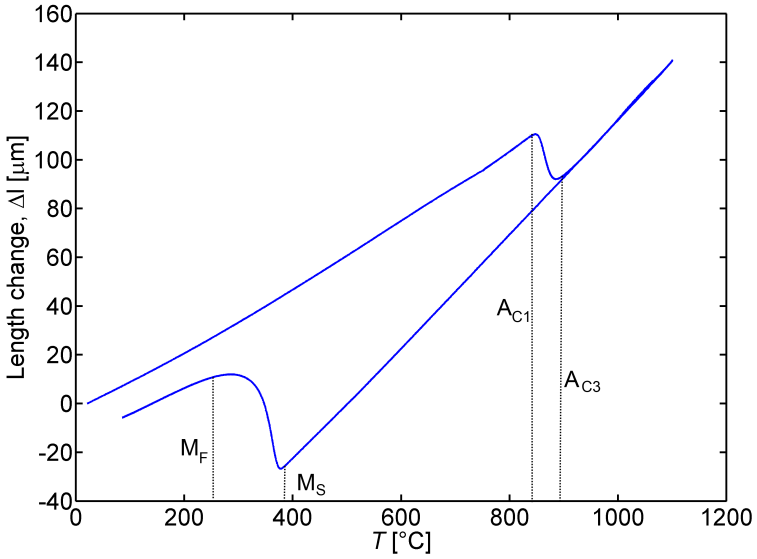

Figure 4.13: Dilatometer curve of the QT weld test plate, recorded with a ramp rate of 0.3 K/s, a holding time of 180 s at 1100 °C and a free cooling.

4.2 Blind Weld Study

4.2.1 Material Test Plate

The as-delivered material test plate (see Fig. 3.1a) was cut in two halves, denoted with “A” and “B”. In an initial test run, the transferability of welding parameters

for plates of comparable thickness was shown (see App. A.3). Based on this pre-test, the parameter window could be further reduced for the material test plate and a new thickness of 25 mm. The complete blind test parameter set is shown in Tab. 4.4. The welded plates were cut along the cross-section, ground and etched with Adler's reagent. For blindwelds which were identified to be adequate via visual inspection, macrographs were taken (see Fig. 4.14 and 4.15). Since a cross-sectional cut at an arbitrary position entails the risk of an incorrect evaluation of the weld quality, a longitudinal cut was performed for a selection of the blind welds. According to the cross-sectional cuts in Fig. 4.14 and 4.15, weldment E, H (Plate A) and 7, 8 (Plate B) were selected. The obtained macrographs after etching the polished cut surfaces are shown in Fig. 4.16-4.19. From this evaluation the parameters were further reduced based on the following conclusions:

- **Plate A**
  - I = 65 mA could be identified as lower boundary for the beam current
  - the majority of the weldments contain pores which may be related to an unfinished degassing of alloying elements and Nitrogen is a potential candidate. This is supported by the fact, that the weldment with the most pores (G) refers to a comparably high welding speed.
- **Plate B**
  - The slight increase in velocity from 9.25 to 9.5 mm/s compared to weldment (G) from Plate A, but with the same beam current, promoted this effect even more. In addition, the high velocity hindered the seal of the key hole and lead to the entrapping of a heavy cavity at the root (5).
  - 9.5 mm/s was identified as maximum welding velocity

Some of the weldments exhibited end-crater cracks in the slope-out regime. In the case of longitudinal weldments, this could be countermeasured by ending the weld bead on an outlet piece as it is recommended in EN ISO 6520-1. Therefore, the modification of the slope-in and slope-out parameters was not further considered, the evaluation being focusing only on the part of the weldment where the beam has reached its final energy density. The parameter window is thus narrowed to 65 <I <70 mA and 8 <v <9.5 mm/s.

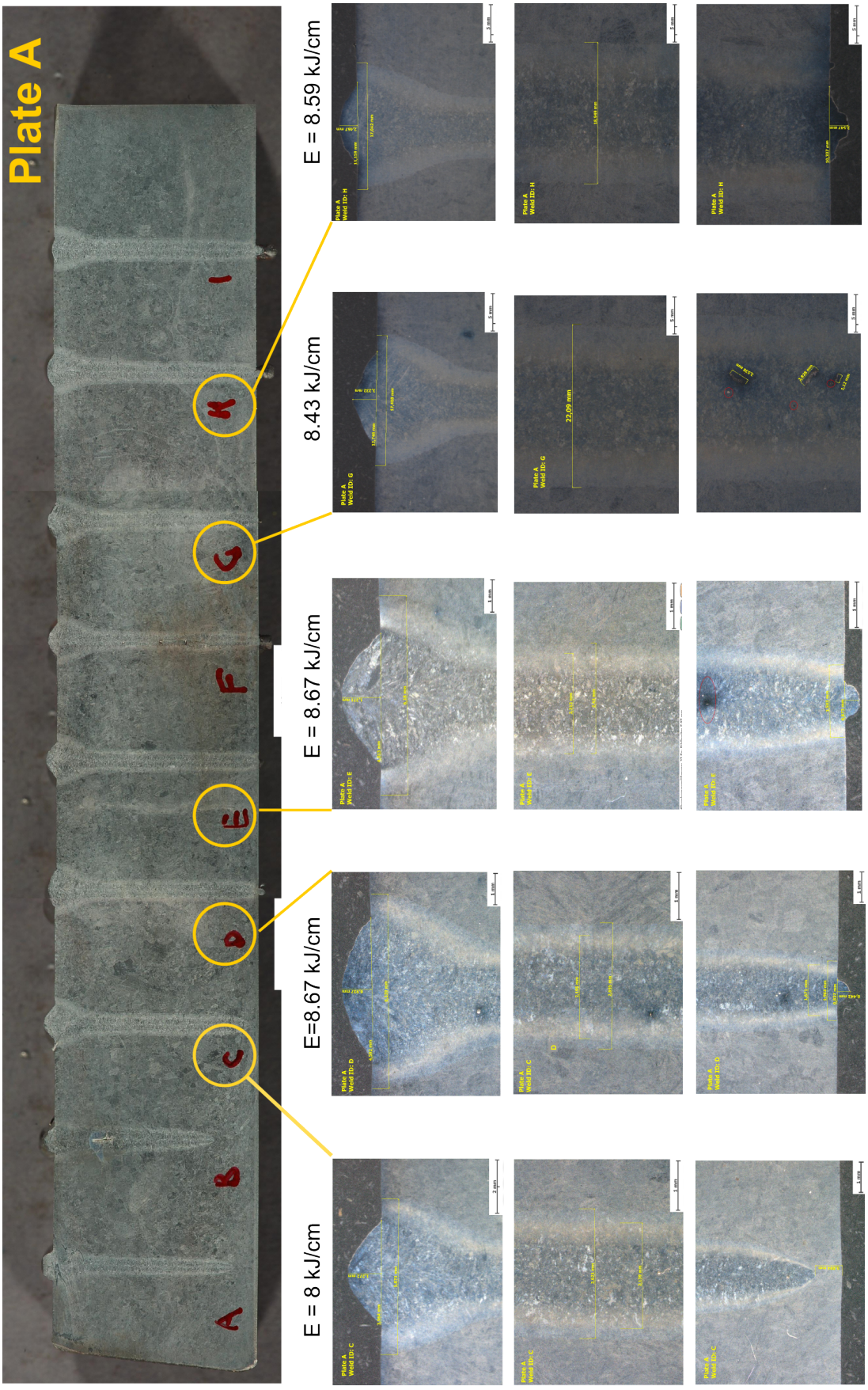

Figure 4.14: Selection of blind weldments of material test plate and their macrographs

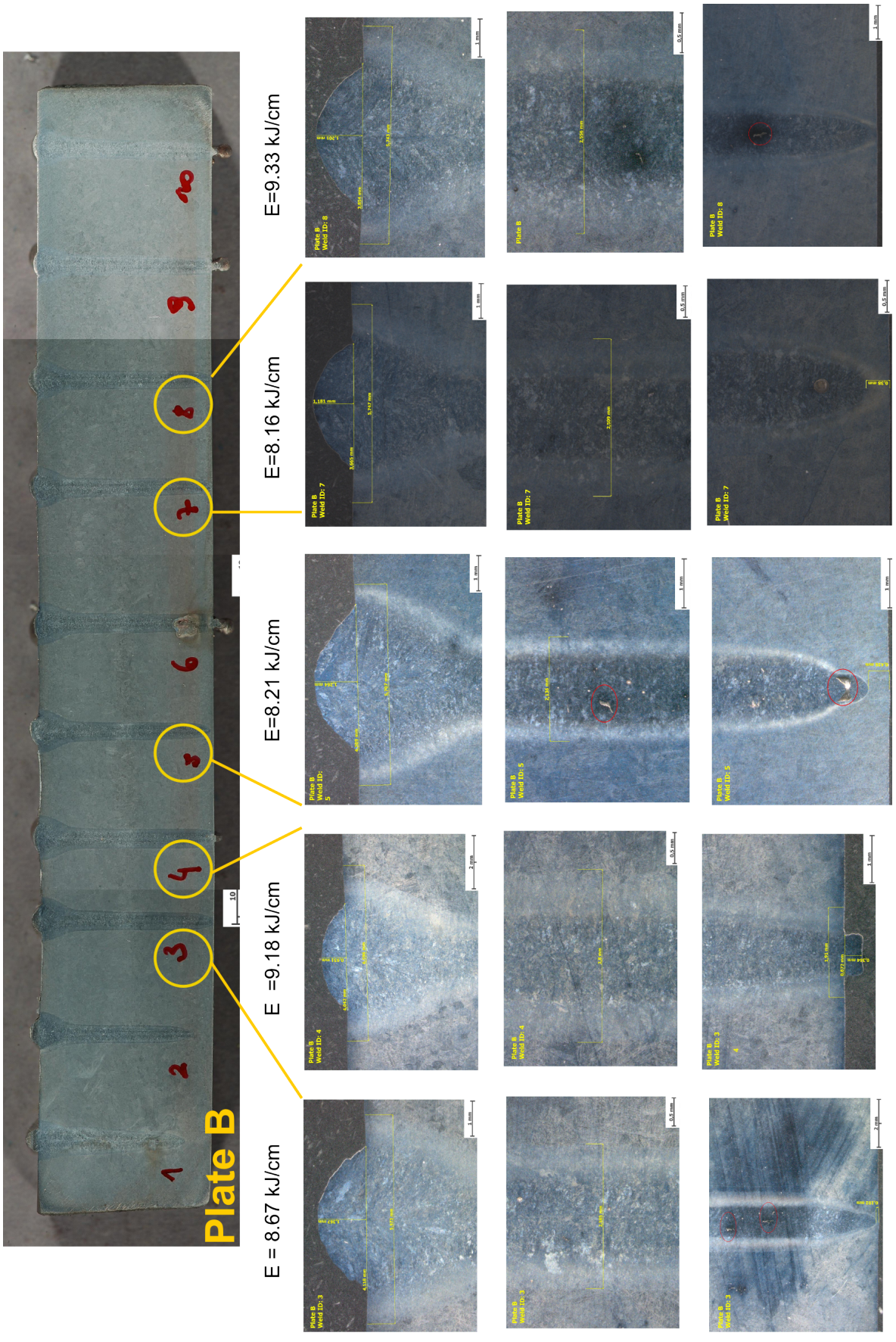

Figure 4.15: Selection of blind weldments of material test plate and their macrographs

Table 4.4: Parameters for blind weld study on material test plate, the focus was set to the surface of workpiece

Identifier	I (mA)	v (mm/s)	SL (mA)	P (kW)	E (kJ/cm)
C	60	9	2603	7,20	8,00
D	65	9	2602	7,80	8,67
E	65	9	2599	7,80	8,67
G	65	9,25	2599	7,80	8,43
H	68	9,5	2597	8,16	8,59
3	65	9	2602	7,80	8,67
4	65	8,5	2599	7,80	9,18
5	65	9,5	2599	7,80	8,21
7	68	10	2597	8,16	8,16
8	70	9	2596	8,40	9,33

Figure 4.16: MTP,longitudinal section of blind weld E [Adler]: severe end-crater crack due to restraint to shrinkage of the concave shaped weld seam, improper slope-out.

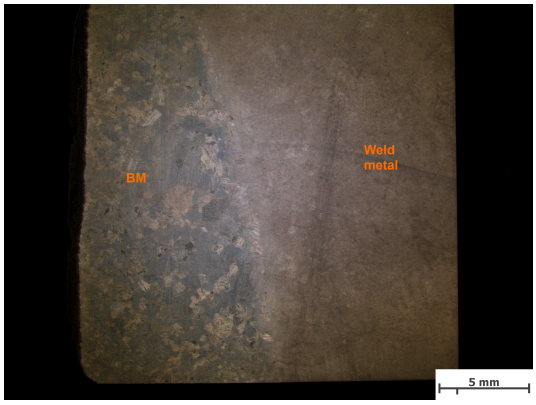

Figure 4.17: MTP,longitudinal section of blind weld H [Adler]: no pores and cracks are visible, homogenous molten zone along the length of the weld seam, slope out region.

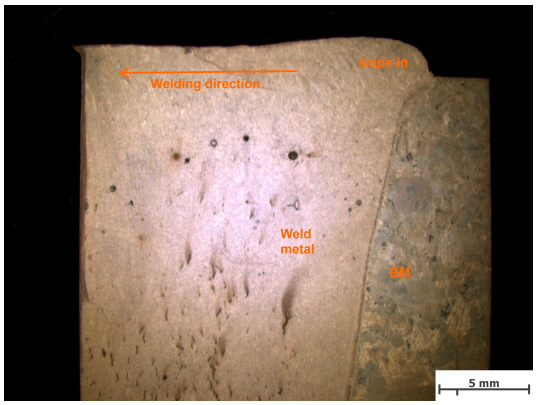

Figure 4.18: MTP,longitudinal section of blind weld 7 [Adler]: heavy pore formation, the spherical form, distribution and size of the pores would indicate an inadequate degassing of the melt during welding due to high speed (v=10 mm/s here).

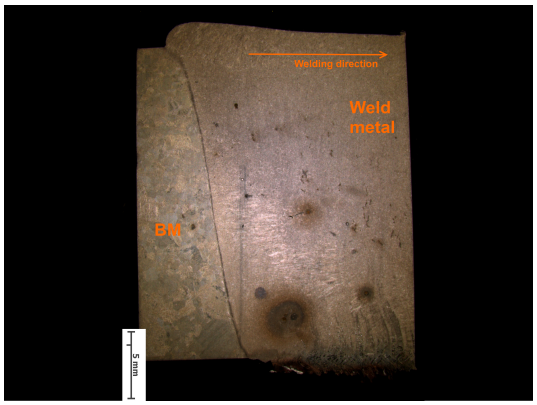

Figure 4.19: MTP,longitudinal section of blind weld 8 [Adler]: entrapped pores, small hot cracks, and root spiking in some parts

4.2.2 Weld Test Plate

Based on the above findings the parameters E, H, 8 were used as starting point for the blind weld study on the weld test plate, the parameters are listed once more in Tab. 4.5. Regardless of the pore formation in MTP blind weld 7, it was decided to re-test these parameters as well, in order to check the reproducibility of failures. The macrographs are shown in Fig. 4.20-4.26. The parameter set 7 was definitely identified as being not suitable. Assuming that in general less line energy is required for a butt weld of the same material and thickness, the parameters E,H are evaluated as best parameters for further butt welding. Nevertheless, parameter set 8 is tested too.

Table 4.5: Parameter selection for the blind weld study of the QT weld test plate

Identifier	I (mA)	v (mm/s)	SL (mA)	P (kW)	E (kJ/cm)
E	65	9	2599	7.8	8.67
H	68	9.5	2597	8.16	8.59
8	70	9	2596	8.4	9.33

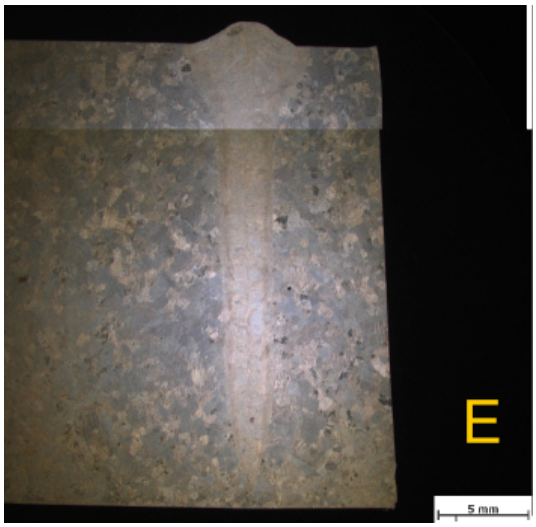

Figure 4.20: WTP,blind weld E [Adler]: cross-section, no pores and not fully penetrating, the overall quality is adequate, regular weld bead

Figure 4.21: WTP,blind weld H [Adler]: cross-section, no pores and not fully penetrating but penetration depth is larger than for E, the overall quality is adequate, regular weld bead

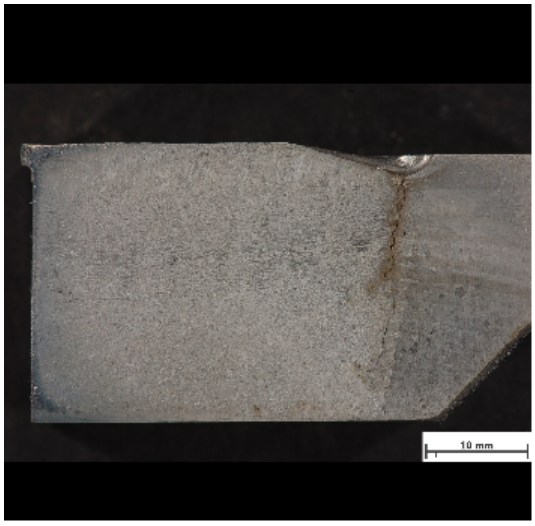

Figure 4.22: WTP,blind weld H [Adler]:longitudinal cut, besides the end-crater crack the overall quality is satisfying

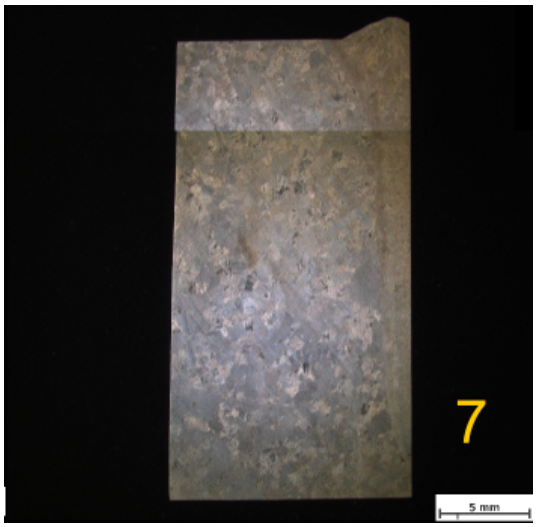

Figure 4.23: WTP,blind weld 7 [Adler]:cross-section, no pores and not fully penetrating, the overall quality is adequate, regular weld bead, the cross-sectional cut was performed after the longitudinal cut.

Figure 4.24: WTP,blind weld 7 [Adler]: longitudinal cut, the penetration depth over the weld seam length is not constant, a general decrease is identifiable which starts at the mid of the weld seam and is thus not triggered by the slope-out of 5 mm.

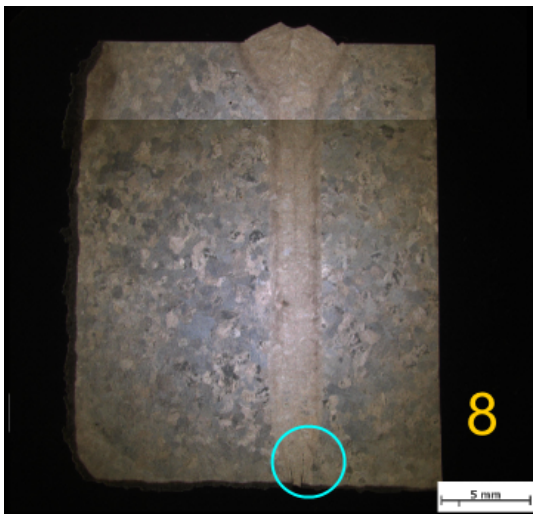

Figure 4.25: WTP,blind weld 8 [Adler]: underfill of weld seam and longitudinal crack in the weld metal zone at the root (marked with blue circle)

Figure 4.26: WTP,blind weld 8 [Adler]:longitudinal cut, the quality in general is adequate, the etching process revealed despite repeated etching an inhomogenous result. a small crack is visible, the through-welded root is an indication that the plate is fully penetrated.

4.3 Joint Weld Study

4.3.1 Material Test Plate

The parameters derived from the blind weld study were now transferred to joint weldments. The plate was cut into smaller pieces, the contact surfaces were ground with special regard to parallelism. Parameter H did not lead to the required penetration depth and was not further investigated. The parameter set 8 produced a very thick irregular root and was therefore also not cut and etched. The crack observed in the weldment E may be caused by an insufficient beam adjustment.

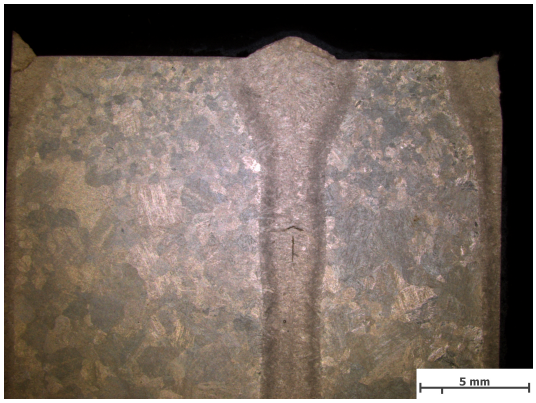

Figure 4.27: MTP,butt weld E [Adler]:The cross section shows two cracks, one in transverse and one in longitudinal direction in the weld metal zone.

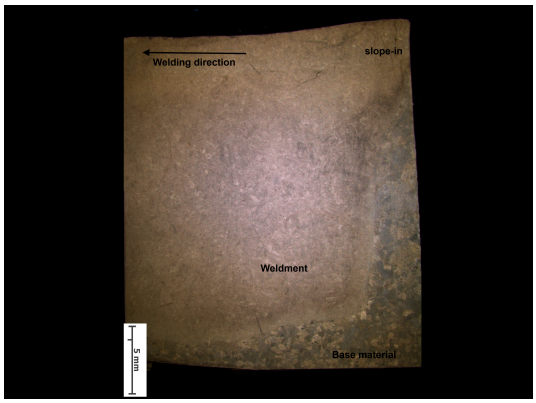

Figure 4.28: MTP,butt weld E [Adler]:longitudinal cut, no pores or cracks were visible across the first half of the weld seam, full penetration was not achieved along the complete weld length.

4.3.2 Weld Test Plate

According to the joint weldments of MTP, the parameter for the butt weld study of the weld test plate could be further reduced to E and 8. The parameter E was used for a repeated blind welding and a butt welding, parameter 8 was only used for butt welding. The three weldments are shown in Fig. 4.29. The penetration depth of parameter E suggested a slight increase in line energy, while parameter set 8 seemed not to fit despite higher line energy. While the root of the blind weld E is only weakly defined, but visible, the root of the related butt weld E is not defined. The small root at the lower image border is caused by a gap between the contact surfaces. The parameter set 8 leads to a severe underfill and concavity of the upper bead, accompanied by a very

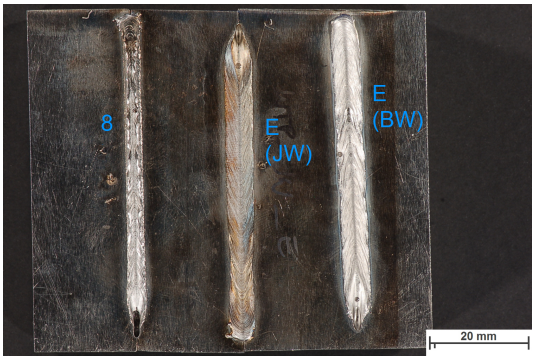

(a) top side

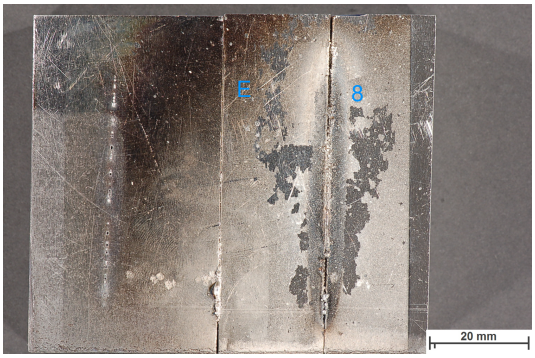

(b) bottom side

Figure 4.29: Weld test plate with two joint welds and one blind weld for check-up

(a) top side

(b) bottom side

Figure 4.30: Weld test plate with final optimised weld parameter. The orange arrow indicate the position of the thermocouple closest to the fusion line.

pronounced and irregular root. The results suggested to keep the beam current value (65 mA) but slightly decrease the velocity to achieve a higher line energy and thus a better penetration. A butt weld with I=65 mA, v=8 mm/s was performed and yield the desired weld quality. A detailed presentation of the microstructure and properties of this finalised weld seam is given in the next section. It is worth noting that this "optimum" parameter set was repeated several times, to check the reproducibility and was finally used as welding parameter to obtain a continuous weld bead over a length of 150 mm. This weld is shown in Fig. 4.30.

4.4 Characterisation of Joint Weld

The optimised welding parameters produced two weldments of ≈ 150 mm length on WTP material of 25 mm thickness. One of the weldments was cut in order to machine

tensile test samples and to obtain micrographs. Results from this initial characterisation are presented in the following.

4.4.1 Microscopy

A stacked image showing the microstructure of the final weldment after PWHT is given in Fig. 4.31. The width of the heat affected zone of the weldment is ≈ 0.75 mm. The quality heat treatment of the machined plates caused a thick oxide layer as already outlined above. This again required the machining and grinding of the plates, where at some positions the plates were so pitted that a complete removal would not have allowed to keep the desired thickness of 25 mm. It was therefore decided to keep the thickness at costs of some areas of minor surface quality. In the root area, an offset as well as a slight displacement of the beam due to a higher remanent magnetic field in this area is exhibited. Nevertheless this did not have any impact on the performed or planned measurement since this part is removed during the machining of the samples anyway. Details of different regions in and around the weld are shown in the as welded condition in Fig. 4.32-4.37 and after PWHT in Fig. 4.38. The spots from hardness measurement were still visible in the light optical microscope and were used as referencing point for the investigation of the weldment after PWHT. The as-welded sample was fully ground and thus no hardness spot left. The turns with micrometer screw at the LOM for horizontal positioning were therefore kept constant between two positions.

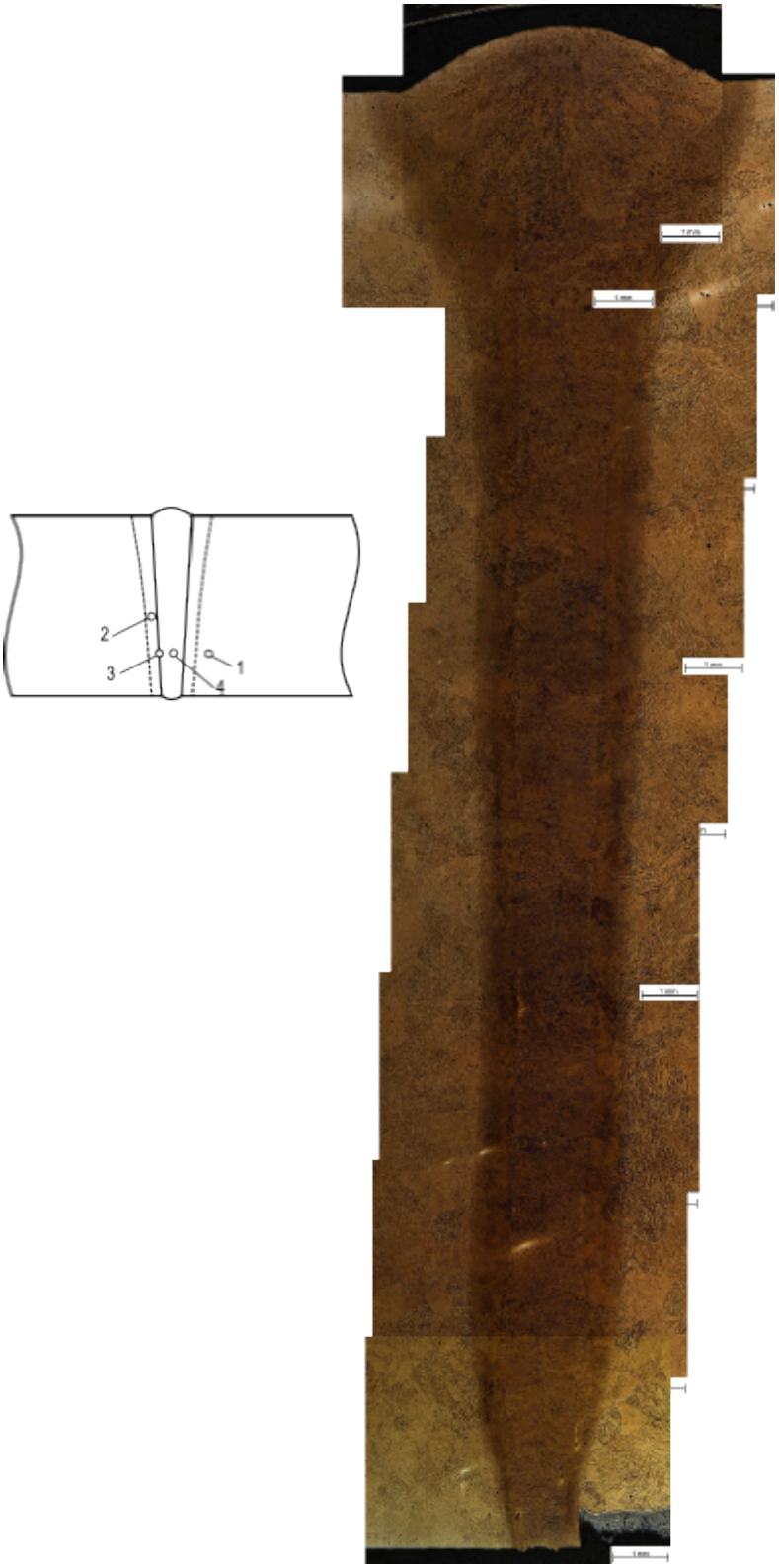

Figure 4.31: Stacked micrograph of the final weld seam after PWHT. The small schematic links different zones of the weldments to numbers which are used for further referencing. The width of the HAZ is ≈ 0.75 mm.

Figure 4.32: Overview of the region ranging from base material to molten zone

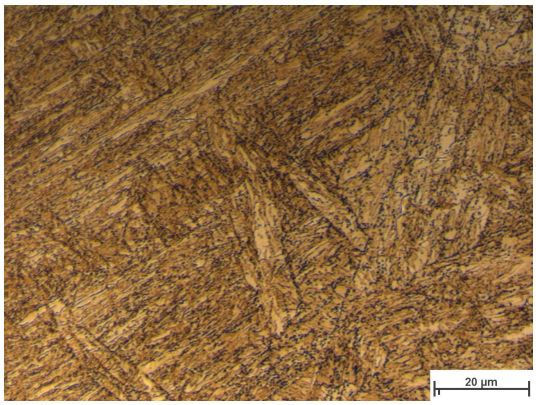

Figure 4.33: (1-2) - Transition from base material to heat affected zone

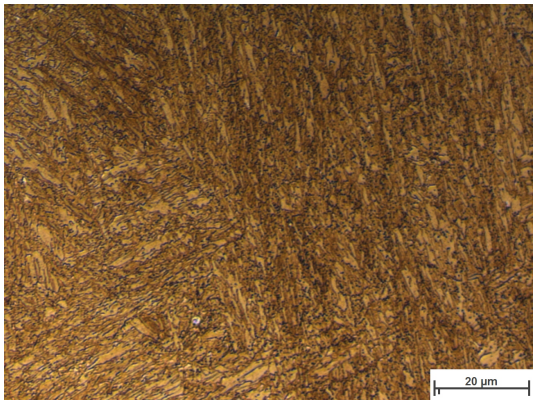

Figure 4.34: (2) - Transition to a very fine structure, no PAGB visible

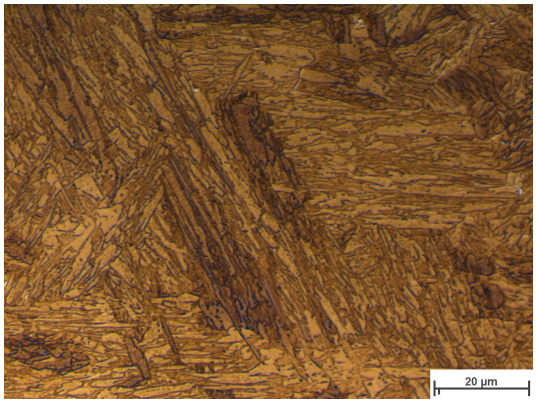

Figure 4.35: (2) - Transition to a coarser grained structure

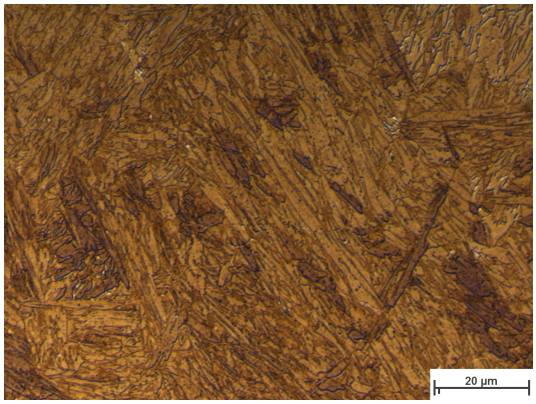

Figure 4.36: (3) - Transition from the coarser grained structure to molten zone

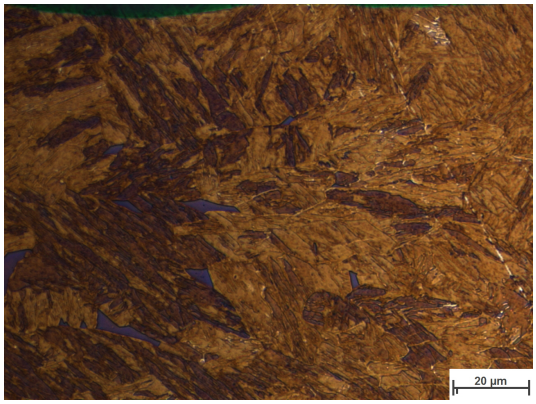

Figure 4.37: (4) - The molten zone without filler metal does not show a pronounced microstructure alignment. Delta ferrite appears blue by the etching.

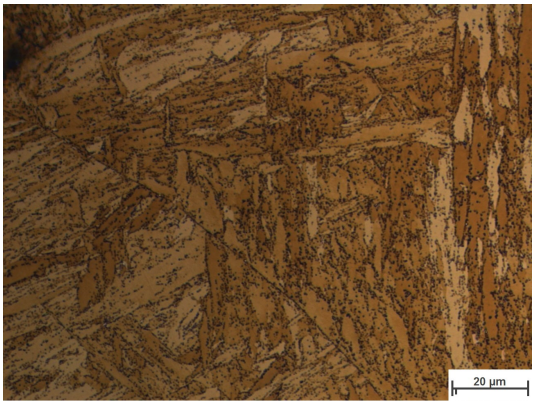

(a) 1 - Base material(#13)

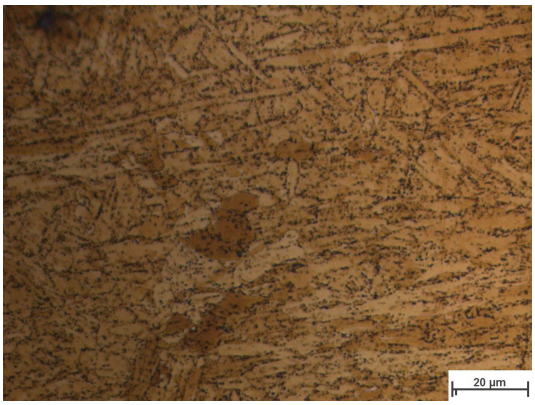

(b) 2-HAZ(#11)

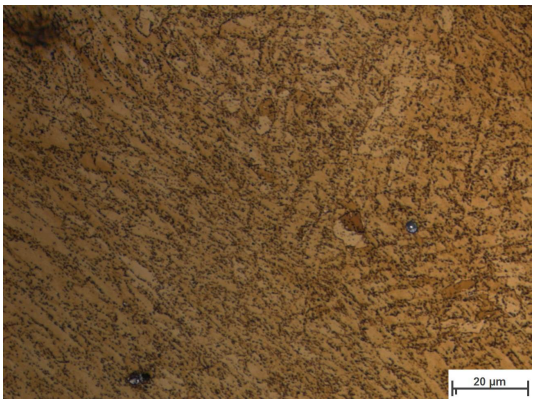

(c) 2-HAZ (#10)

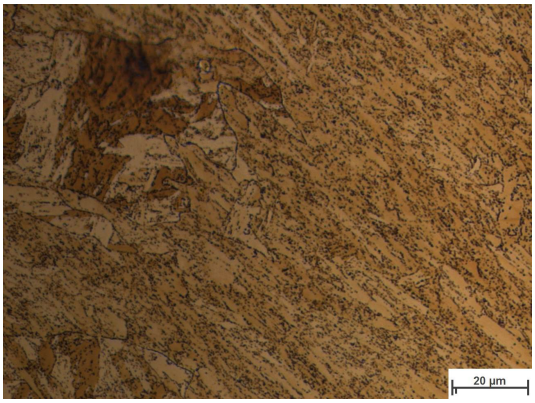

(d) 2- HAZ(#8)

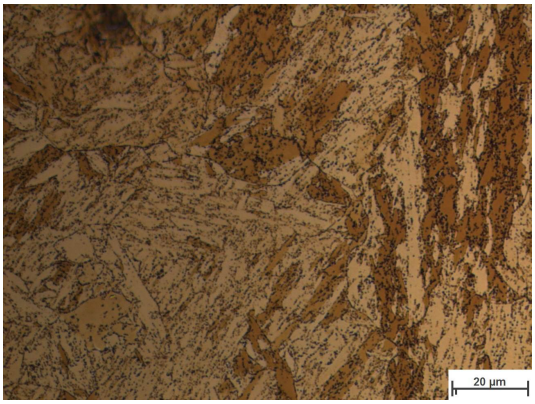

(e) 3- Transition HAZ, molten zone (#7)

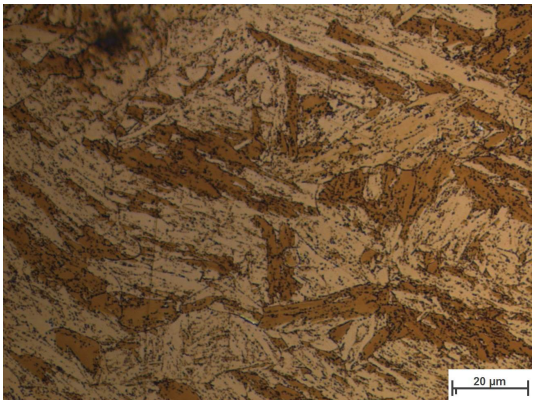

(f) 4 - Molten zone (#6)

Figure 4.38: The different microstructures of a region ranging from the base material to the molten zone after PWHT is shown. The numbers in brackets refer to the labeled hardness spots in Fig. 4.39, where #6 is located in the center of the weld while #13 is located in the unaffected base material. The residual hardness spots were used as a marker and are visible as blurred spots in the upper left corner in some of the images.

4.4.2 Hardness Measurement and Influence of PWHT

A hardness profile across the realised weldments was recorded where the maximum from all recorded hardness measurements was 475 HV1 in the weld metal and the minimum 180 HV1 in the base material. These values were used as outer boundaries for an assignment of pseudocolors to the hardness values, the colored harness profile for the final butt weld is shown in Fig. 4.39. The color index is shown at the bottom of the images, where the harness increases in steps of 17 HV1 from dark blue to white. In the as-welded condition, the highest values occur in the weld metal and at the fusion line, the hardness in the weld metal center is around 460 HV1 and drops to ≈ 400 HV1 at the fusion line. In the HAZ values between 300 and 400 HV1 are measured which decrease to ≈ 260 HV1 for the unaffected base material.
The PWHT clearly decreases the hardness gradient, the hardness ranges now from 300HV1 in the weld metal to 270 HV1 at the fusion line and 235HV1 in the base material.

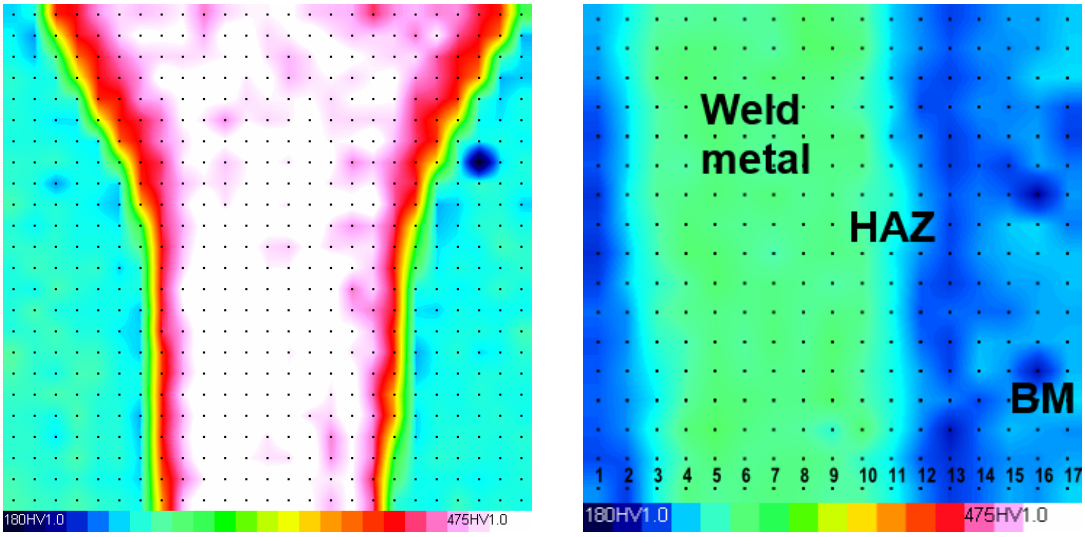

(a) as weld **(b)** PWHT

Figure 4.39: Pseudocolored hardness map of the final butt weld in (a) as-weld and (b) PWHT condition.

4.4.3 Tensile Test

In total four tensile test specimens of geometry B10x50 according to B50125:2004-01were machined from the final welded plates after PWHT. The curves obtained at room temperature are shown in Fig. 4.40. The measured variables are listed in Tab. 4.6

Table 4.6: Results from tensilte test at room temperature

Sample	$R_{p0.2}$ [MPa]	R_m [MPa]	ϵ [%]
(blue)	614	750	17
(red)	614	751	17
(green)	619	742	17
(black)	612	748	16
WTP-QHT	654	787	17

where the colors refer to the line color in the respective figure. In general the values elongation is congruent with the values for the quality heat treated weld test plate without weldment, also the yield strength and tensile strength are slightly lower than those values. The macrograph in Fig. 4.41 shows that the fracture definitely occurs in the base material, the crack propagates from pore to pore.

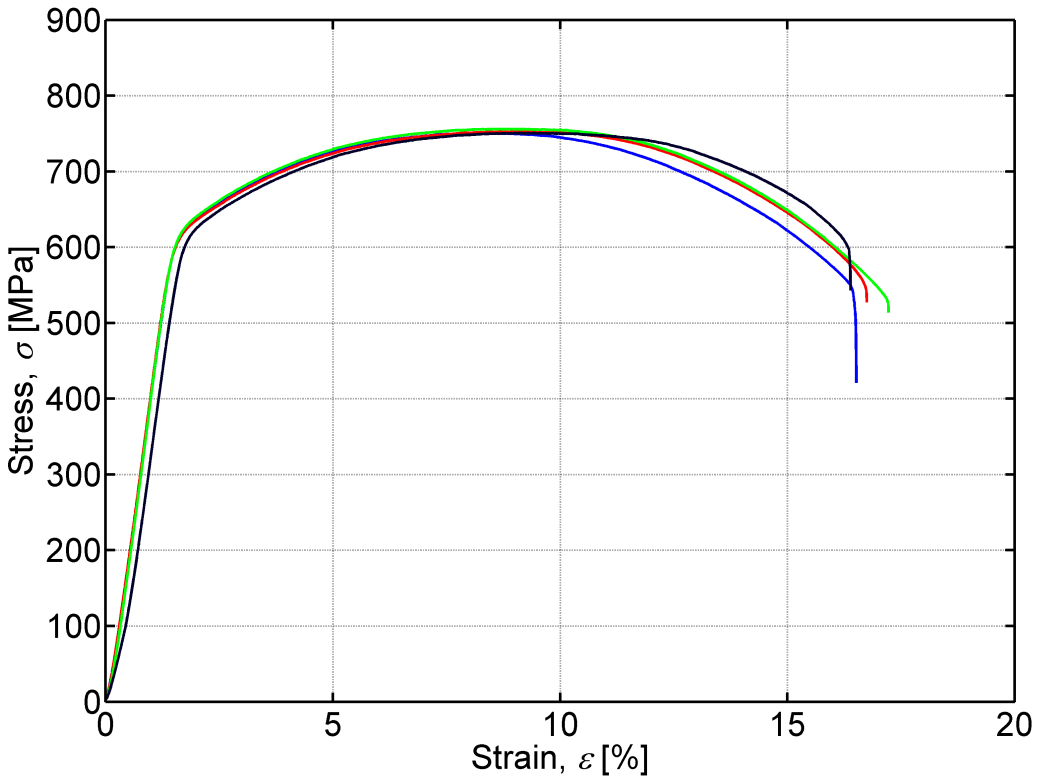

Figure 4.40: Tensile test at room temperature of the optimised weldments after PWHT

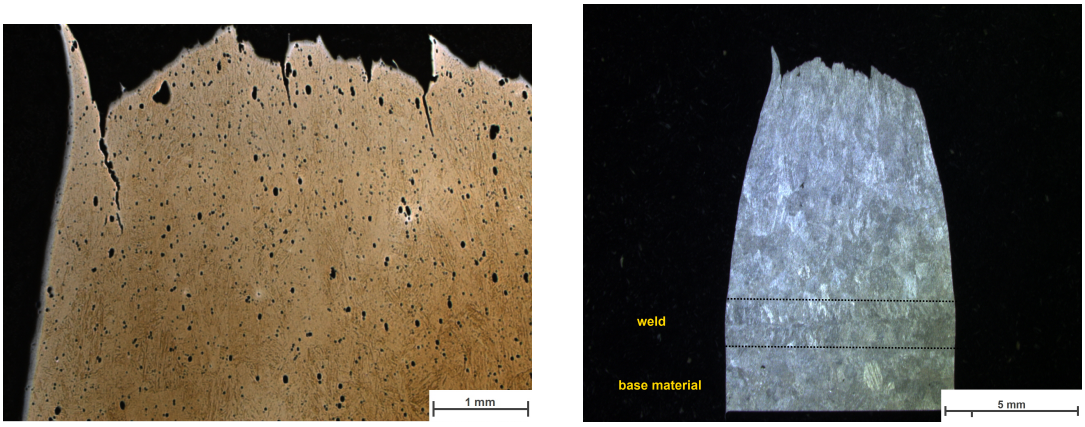

(a) Micrograph **(b)** Macrograph

Figure 4.41: (a) Longitudinal cut of tensile sample fracture location etched with mod. LB and Adler. The crack development along pores is clearly visible. (b) The etching did not give a good contrast between weld seam and base material, therefore the welded area is framed by dashed lines.

4.5 Gleeble Heat Affected Zone Simulation

The EB welding did also involve the tracking of the temperatures dependent on the distance from the weld center in order to correlate the obtained microstructure with the appropriate peak temperatures. In Fig. 4.42 the thermal cycle for the optimised butt weld parameters is shown. It was not possible to measure higher temperatures without melting parts of the spot-welded thermocouples. Based on the assumption of a melting temperature around 1520 °C, and the highest measured peak temperature during the EB welding cycle, the peak temperature range of interest was defined from 900 to 1300°C for the subsequent HAZ simulation. The $t_{8/5}$ time was determined to be 4 s, and this value was then used for the QuikSim Software, along with the physical properties calculated with JMat-Pro (see App. A.5). On the Gleeble samples, the central thermocouple (TC1) was used as control thermocouple, two different thermocouples with different distances from the axial sample center were used to measure the thermal gradient. The desired cooling rate could not be achieved (see Tab. 4.7), nevertheless a $t_{8/5}$ time of 6 s is still adequate. The thermal cycles corresponding to the four different peak temperatures are shown in Fig. 4.43-4.46. A peak temperature of 1300 °C caused a partly melting of the sample, see Fig. 4.48. As outlined in Sec. 3.2.2, the electric resistance of the components influences the bulk heat gain. The transition resistance R2 (sample/copperjaw) in Fig. 3.10 is higher than the pure resistance of the sample and thus the temperature measured of by the thermocouple closest to the

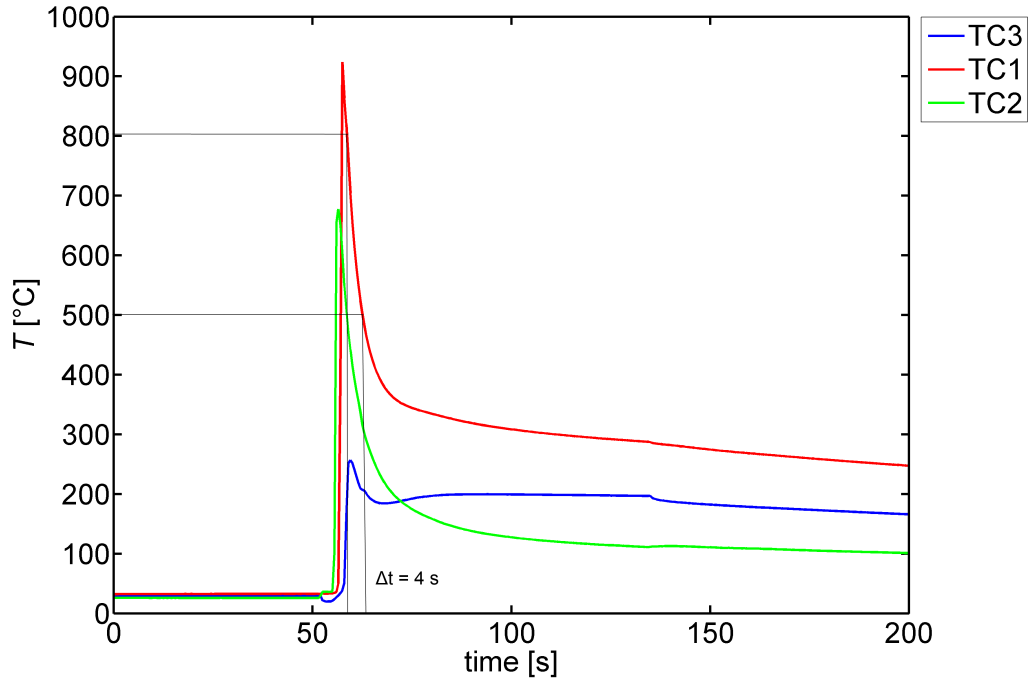

Figure 4.42: Thermal cycle corresponding to the "optimised" parameters (I=65 mA, v=8 mm/s). The numbering of the thermocouples does not correspond to the chronological order they have been passed by the beam, but to the distance of the fusion line. So, thermocouple TC3 was the most distant thermocouple but experienced the thermal cycle at first (the related curve is shifted left).

jaws/farthest from the central thermocouple records a higher peak temperature than the programmed temperature.

In the caption of the below temperature curves, d1 denotes the distance of TC2 from TC1, and d2 is the respective distance for TC3. The physical simulation for 1100 °C was performed twice in order to investigate the microstructure. The micrographs are shown in Fig. 4.49-4.52. The other samples are foreseen for creep testing along with the welded EBW samples. A comparison of the microstructure between the simulated microstructure and the HAZ of the EB weldment is given in Fig. 4.57. A one-to-one-relationship could not be detected with between the simulated HAZ and a subregion in the real EB weld. This has been reported also in other publications and especially weld simulation for very high temperature gradients seemed to be not a fully reliable method [9].

Table 4.7: Calculated and measured values of peak temperature and $t_{8,5}$

T, t	calculated	TC1	TC2	TC3
T_{peak}	900,00	899,63	755,96	934,95
$t_{8/5}$	6,52	6,56	NaN	5,94
T_{peak}	999,80	997,80	851,40	1082,30
$t_{8/5}$	6,27	6,30	6,58	6,39
T_{peak}	1099,80	1098,20	978,70	1128,10
$t_{8/5}$	6,13	6,14	6,14	6,02
T_{peak}	1299,70	1298,70	1269,40	1316,10
$t_{8/5}$	6,00	6,01	5,92	5,96

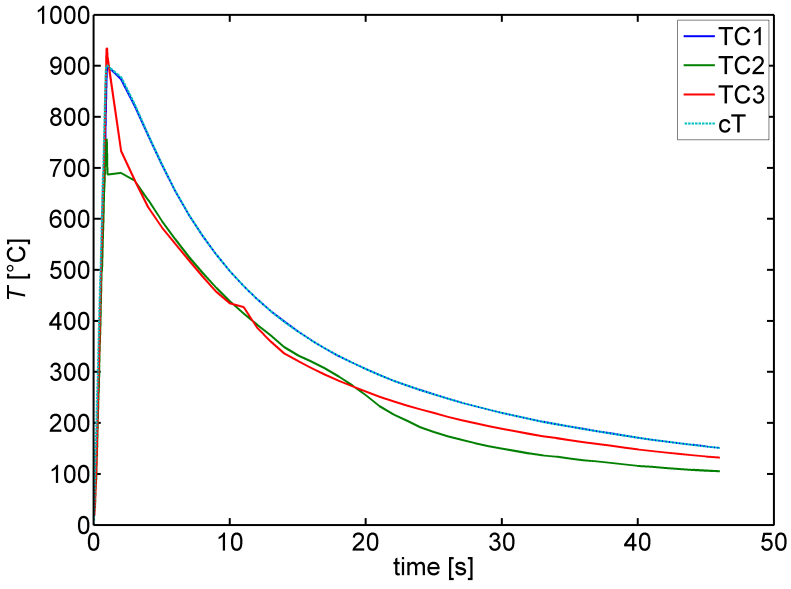

Figure 4.43: Calculated and measured T-cycle for T_{peak} = 900 °C. d1 = 1.4 mm, d2 = 1.6 mm.

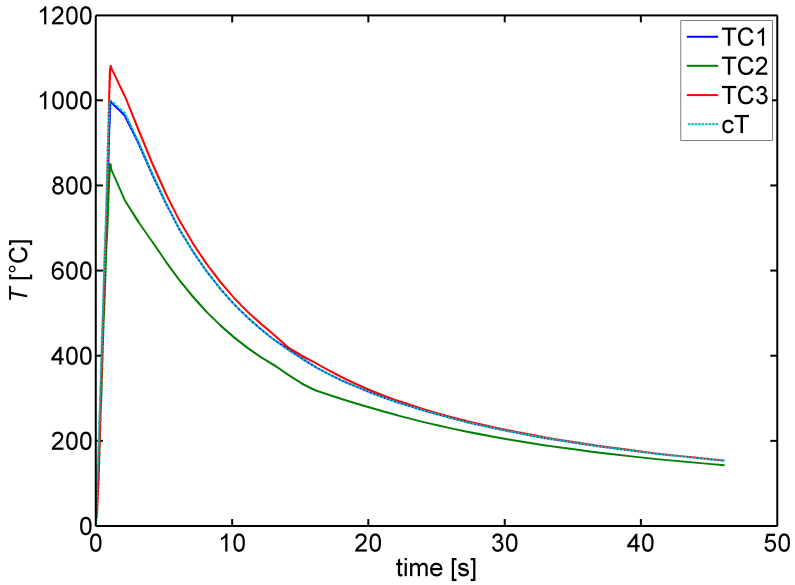

Figure 4.44: Calculated and measured T-cycle for T_{peak} = 1000 °C. d1 = 1.3, d2 = 1.5

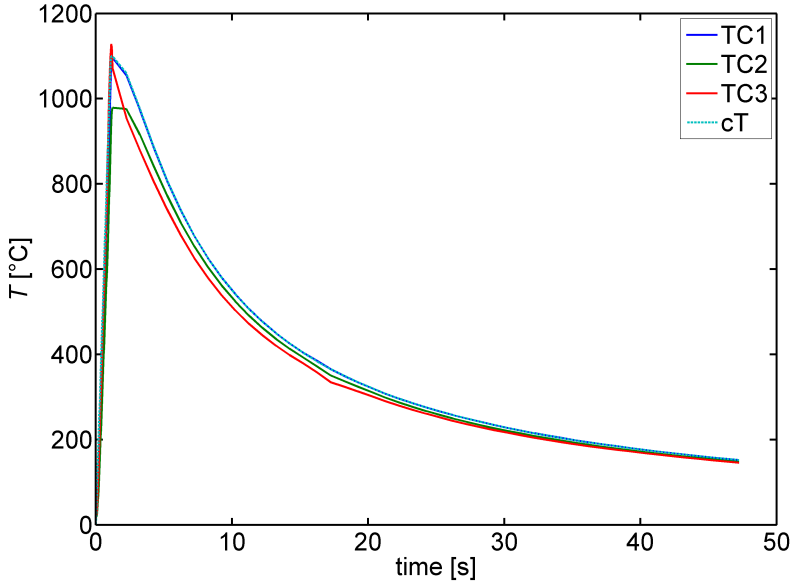

Figure 4.45: Calculated and measured T-cycle for T_{peak} = 1100 °C. d1 = 1.4 mm, d2 = 1.6 mm

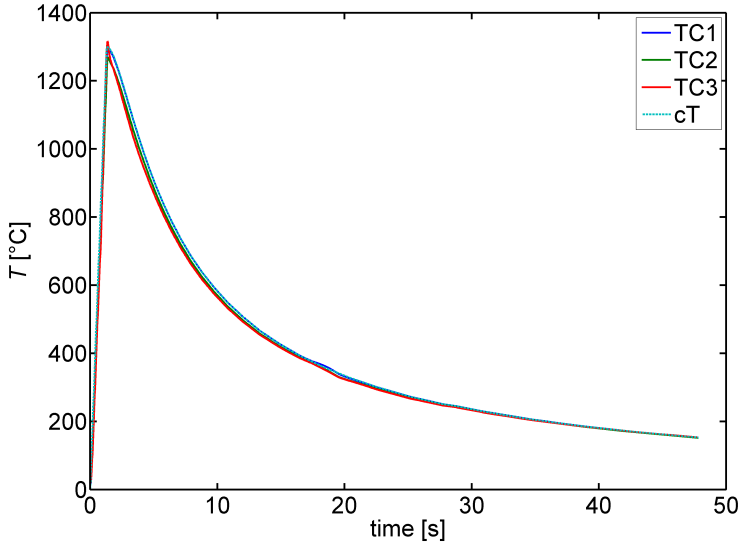

Figure 4.46: Calculated and measured T-cycle for T_{peak} = 1300 °C. d1 = 1.5 mm, d2 = 1.7 mm

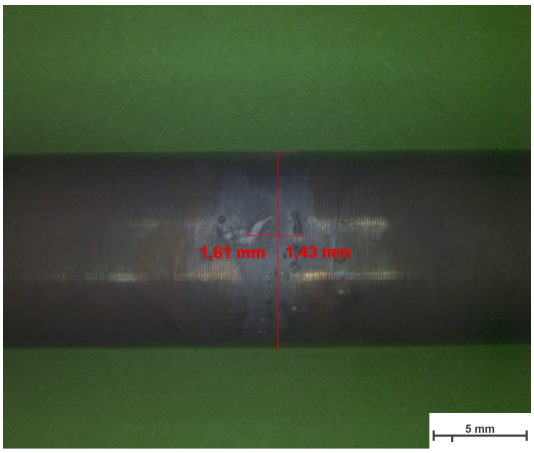

Figure 4.47: Gleeble sample after the HAZ simulation, the position of the TC2 and TC3 are indicated, the free span length was 4.2 mm.

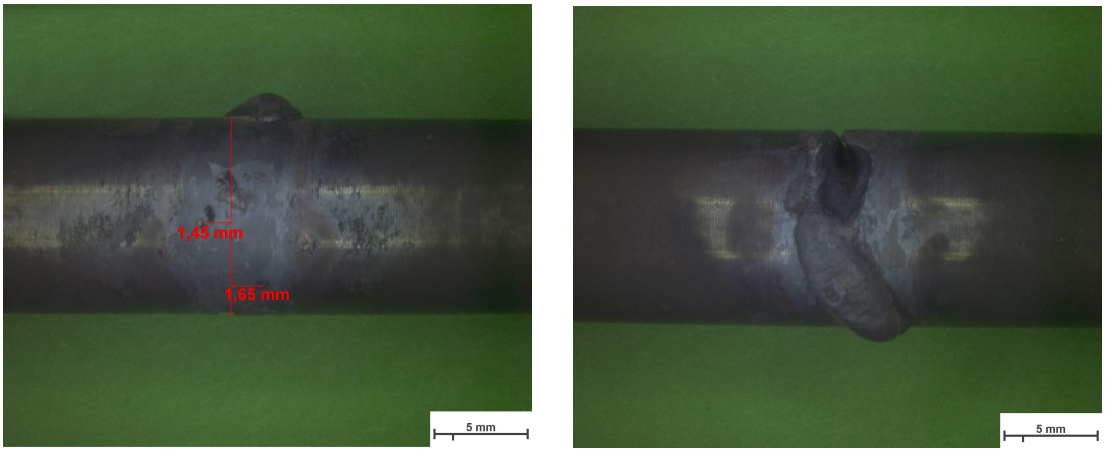

(a) (b)

Figure 4.48: The sample exhibited to a peak temperature of 1300 °C is partly molten in the center. A local overheating due to a wrong thermocouple signal of the central thermocouple TC1 can be excluded, since no irregularities in temperature are shown in the temperature curves of TC2, TC3.

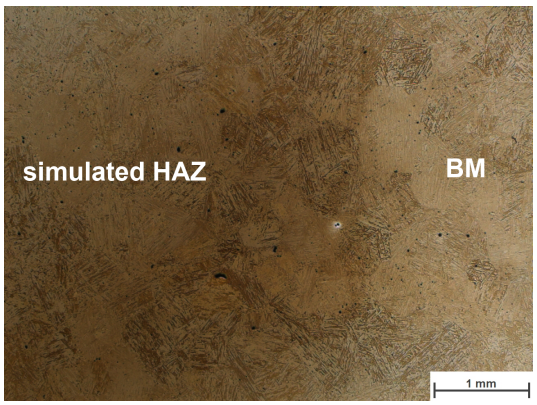

Figure 4.49: Overview of the region ranging from base material to simulated heat affected zone in as-welded condition.

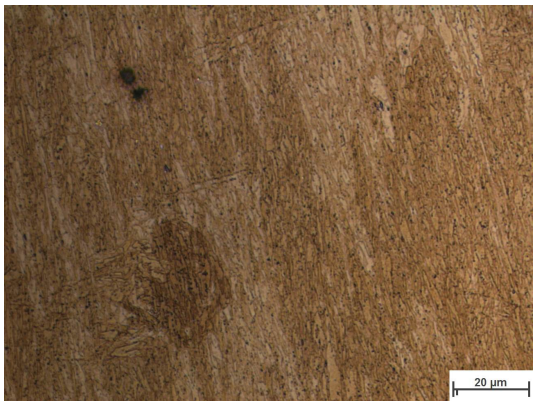

Figure 4.50: Microstructure at the center of the simulated HAZ in as-welded condition, $T_{peak} = 1100°C$.

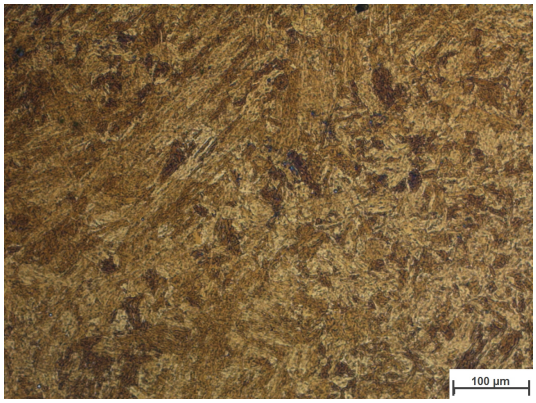

Figure 4.51: Microstructure of the center of the simulated HAZ after PWHT with lower magnification, $T_{peak} = 1100°C$.

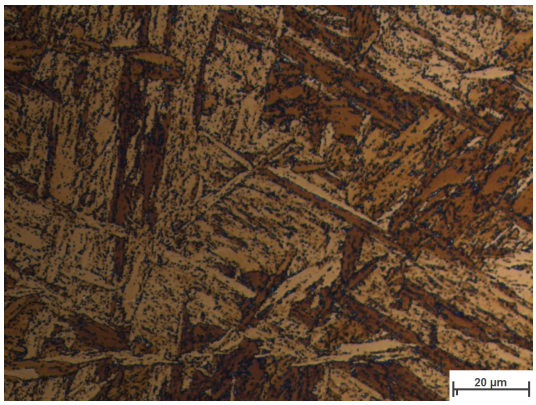

Figure 4.52: Microstructure detail in the PWHT condition, tempered martensite and precipitates along the martensite laths, $T_{peak} = 1100°C$.

4.6 HAZ Simulation Using Dilatometer

The aim of the dilatometer measurement using the same thermal cycle as for the Gleeble HAZ simulation was to determine the transformation points when using very high heating rates (similar to the one experienced during EBW and Gleeble HAZ simulation). The desired heating rate of 1100 °C per second was achieved by the Bähr dilatometer which is confirmed by the related T,t-curve in Fig. 4.53, nevertheless the electronic sampling rate was too low which caused a zigzag shape of the dilatometer curve. The temperature data was therefore smoothed before plotting the length change data, see Fig. 4.54. The achieved cooling rate is equivalent to the Gleeble experiments, the obtained $t_{8,5}$ time is 6 s. The data for the transformation points shown in Tab. 4.8, has to be regarded with reservations, since the high frequency of the induction coil smeared the curve out. The simulation of the sample heating with time using Autodesk Simulation Mechanical 2015 confirms the measurement as shown in Fig. 4.55. At the end of the heating ramp the outer surface is already at the desired temperature while the center of the sample is about 200 °C cooler. The inner volume with higher volume than the outer cylinder ring experiences the transformation point later and thus the change in length appears smeared out.
The microstructure at the inner of the dilatometer sample was investigated in order to compare it with the results from Gleeble and EBW experiments. The micrographs shown in Fig. 4.56 were taken at the center of the gleeble sample. The obtained microstructure is compared with the microstructure obtained during the welding and the HAZ simulation in Fig. 4.57. In all three cases different sample geomtries are used and the heating is based on very different mechanisms, thus the micrographs are not directly comparable. In general, all three micrographs exhibit a tendency to finely pronounced martensite laths and also finely dispersed small precipitates.

Table 4.8: Transformation temperatures with a heating rate of 1100 K/s

Arrest point	T [°C]
A_{C1}	870-970
A_{C3}	1095
M_s	420
M_f	280

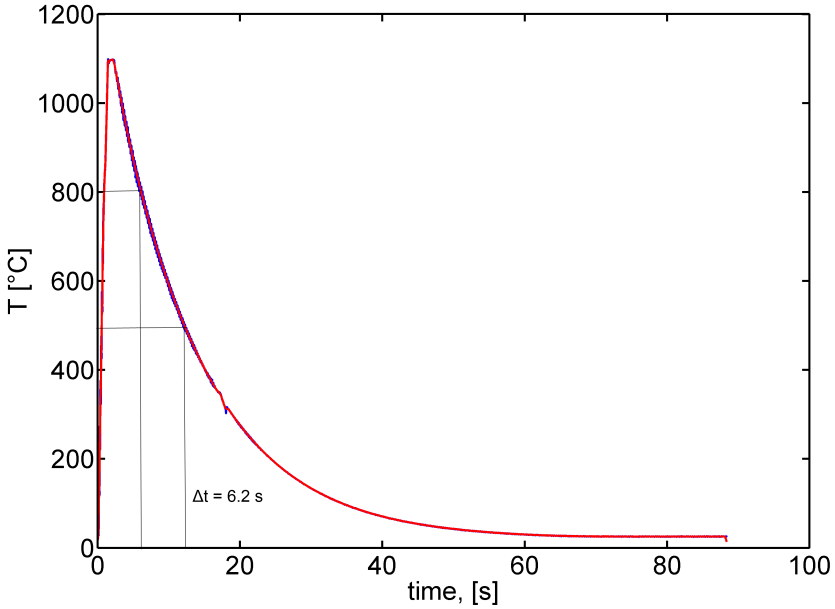

Figure 4.53: The recorded temperature data is shown in blue and the smoothed curve is overlayed in red.

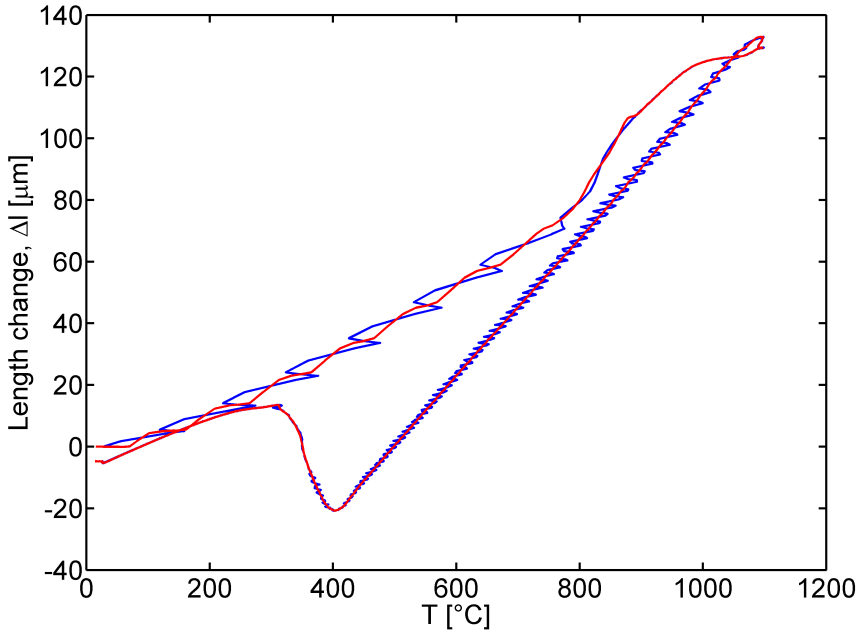

Figure 4.54: The original data is shown in blue and the smoothed curve is overlayed in red. The beginning of the austenitising transformation temperature is quite smeared due to the high frequency of the induction heating coil.

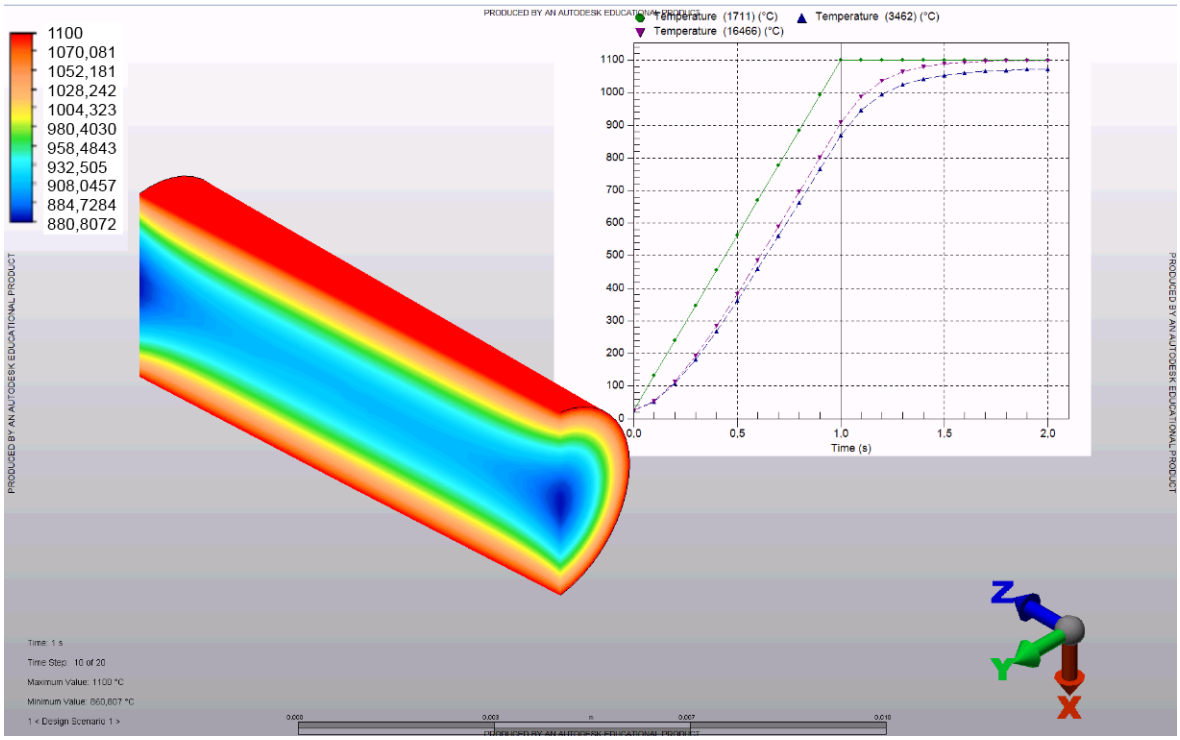

Figure 4.55: Simulation of the radial heat development with time of the dilatometer sample. The green curve in the diagram equals the surface temperature of the dilatometer sample, the violet curve refers to the temperatures at the center of the sample while the blue one is the temperature of the top surface in contact with the dilatometer dies. The physical properties calculated via JMat-Pro were used for this simulation, the dilatometer dies in contact with the top surface were also considered but are not shown in the image. Picture provided by M. Luckabauer

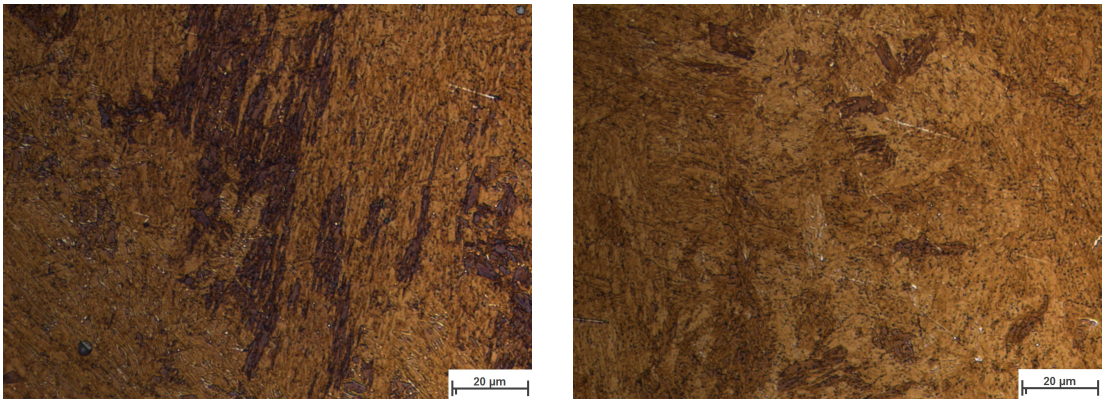

(a) Gleeble HAZ simulation **(b)** Dilatometer with high h

Figure 4.56: Microstructure of dilatometer sample etched with mod. LB. Both micrographs were recorded at the axial center of the sample at different positions.

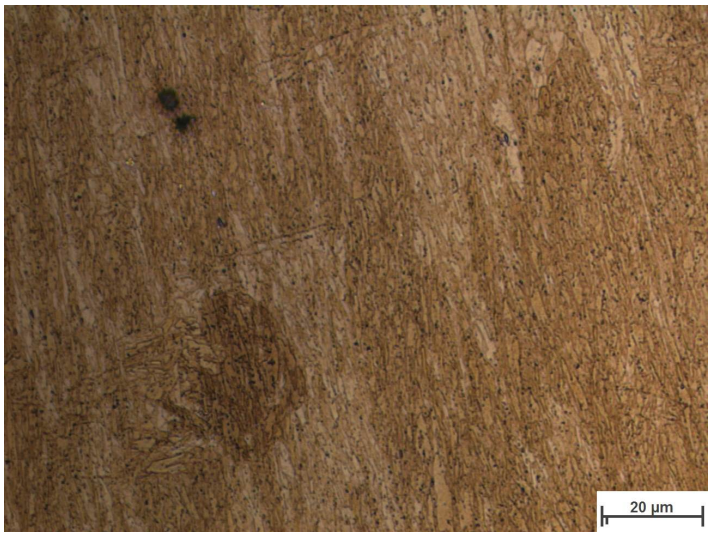

(a) Gleeble, $T_{peak} = 1100°C$

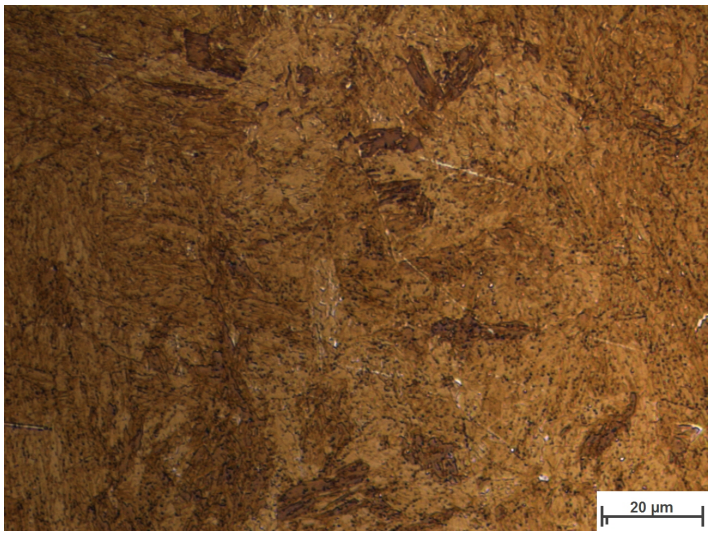

(b) Dilatometer, $T_{peak} = 1100°C$

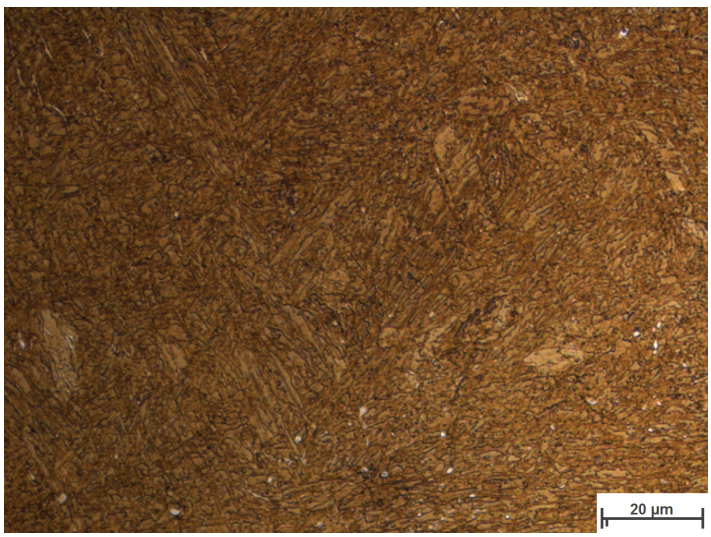

(c) EBW near molten zone

Figure 4.57: Comparison of micrographs obtained from the weld test plate during different experiments.

5 Evaluation of Synchrotron-µCT Data

Crosswelded samples which have been creep tested at 650 °C at different stress levels, were subjected to computer tomographic investigations. This chapter will focus on the evaluation of the obtained data as well on the software-based aspects as on the material-based findings. An overview of the workflow is given in Fig. 5.1.
Parts of this chapter are also presented in a paper [47], which is at date still under review.

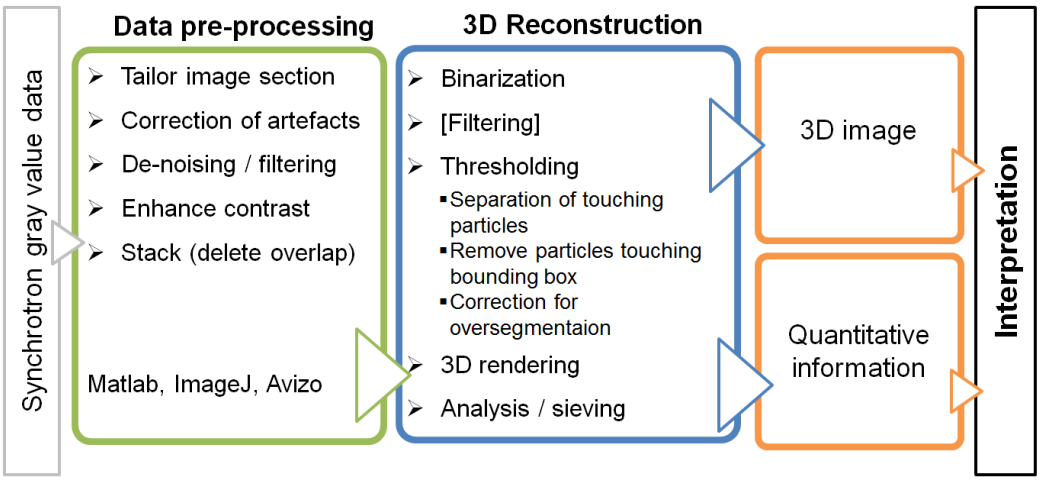

Figure 5.1: Overall workflow for the synchrotron data evaluation

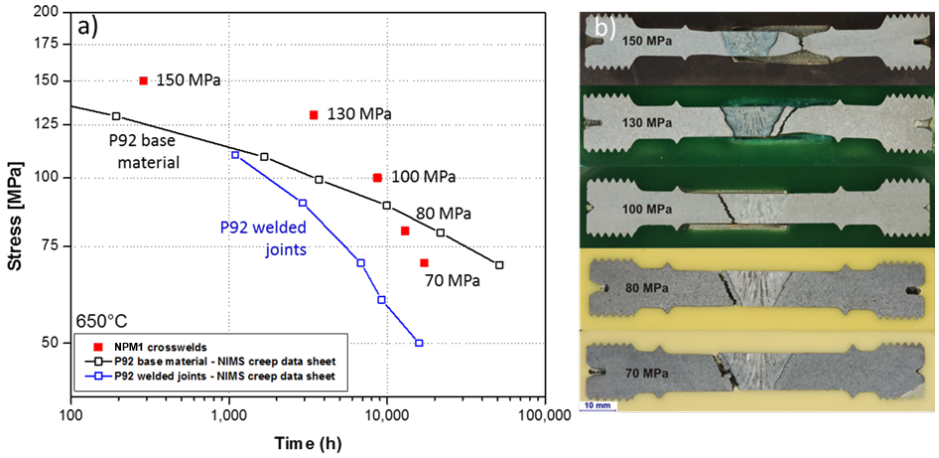

Figure 5.2: Creep testing results for NPM1 crosswelds steel at 650°C (a) compared to grade 92 base material and P92 welded joints. The related samples (b) exhibit a shift in the failure location towards the heat affected zone with decreasing stress levels, image adopted from [47].

5.1 Sample Taking

As part of another project, crosswelded steel of type NPM1 was creep tested. NPM1 is a 9% Cr steel of comparable chemical composition, which is given in Tab. 3.1. The quality heat treatment comprised solution annealing at 1150 °C for one hour followed by precipitation hardening at 740 °C for four hours. The material was tungsten arc welded using Nickel-based filler material (Nibas 70/20-IG). The post weld heat treatment was performed again at 740 °C for four hours. The samples were creep tested at 650 °C and 150, 130, 100, 80, 70 MPa until rupture. The creep curve as well as a longitudinal cut through the creep samples is given in Fig. 5.2. The creep curve also contains data for base material and welded joints of grade 92 steel for comparison. The steel P92 is also a 9% Cr steel but is not modified with a balanced content of Boron and Nitrogen as it is the case for NPM1. The homogenous non-welded base material of P92 refers to the black curve. Compared to the stress-time-to-rupture behaviour of the base material, the welded samples of P92 (blue curve) exhibit a lower creep resistance and the rupture occurs at shorter times for the same stress levels. The negative influence on the creep behaviour is linked to the heat affected zone and the sensitivity of this area to pore formation and cracking. The data of the welded NPM1 samples are indicated with the red marker and show an obvious better creep strength than the welded P92 samples, but still a drop is observed for low stresses and long times. The improvement in creep strength is attributed to the suppression of the fine grained zone by Boron and Nitrogen [47]. In image (b) of Fig. 5.2, the location of failure for the different

stress levels is shown. It is clearly visible, that the location of failure shifts from the base material at high stress levels towards the heat affected zone and fusion line when decreasing the stress level. In order to investigate the pore distribution and size in the heat affected zone, the samples were analysed using SµCT. The sample tested at 150 MPa was excluded from this measurement because the failure location lies without any doubt in the base material and does not require special analysing methods. The sample taking for further CT testing was always done in the HAZ opposite site of the failure which is indicated in Fig. 3.12.

5.2 Synchrotron data evaluation and visualisation

The projection data from the tomographic scan which has been reconstructed via a convolution backprojection, was provided in form of 16-bit gray value images of each tomographic slice. This data was transformed to 8-bit gray scale format, cropped to the desired region, and assembled to a single stack per sample using ImageJ [48]. It is common, that the recorded projection data is processed by a routine in order to remove artefacts for the most part before it is distributed to project partners. Nevertheless the data in the as-received state did still contain strong ring artefacts in some parts of the images, as it is shown in Fig. 5.3 (a). The rings influence the segmentation routine of the software and would require elaborate manual post-processing. The weld metal

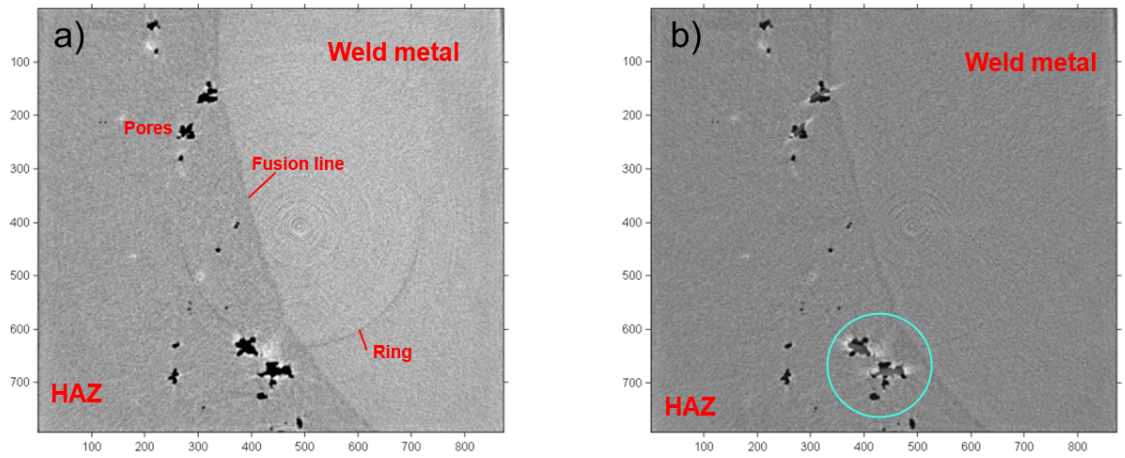

Figure 5.3: Comparison of ring artefacts before (a) and after (b) the ring correction. The ring correction is also causing a decrease in contrast. The scale bars show the number of pixels.

and the rings are in the same contrast region, but the contrast is not too distinct. Several algorithms have been developed in the last years to reduce this artefact while not changing the information of the gray scale value. It was found that a ring correction tool originally developed by Paul Tafforeau at ID19, ESRF worked best [49]. In a first step large structures in the image are masked, their average intensity is calculated and then subtracted from the original data set. The resulting image is transformed into polar coordinates where the former rings are displayed as lines. After Gauss-filtering in angular direction, the image is reversely transformed into Cartesian coordinates. The obtained filtered image again is subtracted from the original one. The Matlab tool was slightly modified to suit the needs and used to reduce the ring artefacts, the corrected image can be seen in Fig. 5.3 (b). The artefact cannot be fully eliminated [49], but the remaining rings do not affect the further images segmentation process.
For the 3D data evaluation and visualisation Avizo Fire (vers. 8.1) from the Visualisation Science Group was used. The gray scale pictures were median filtered which preserves the edge structure and reduces image noise [50]. Afterwards the pores were segmented via thresholding and labelled hereafter. A correction for over-segmentation was performed and pores touching the boundaries were excluded from the region of interest. The pore volume and their equivalent diameter were calculated based on the labelling. The rendering parameters have to be chosen carefully, otherwise the number of pores may be over- or underestimated. In the rendering process, neighbouring pixels of the same segmentation class are grouped to an object which is in the case of the present data equal to a pore. When the acceptance tolerance level is very high, voxels may be included which refer to another pore and thus a single larger pore is rendered instead of two pores close but still separated. In Fig. 5.4, a small detail of pores is shown to illustrate the effect of too high tolerance values.

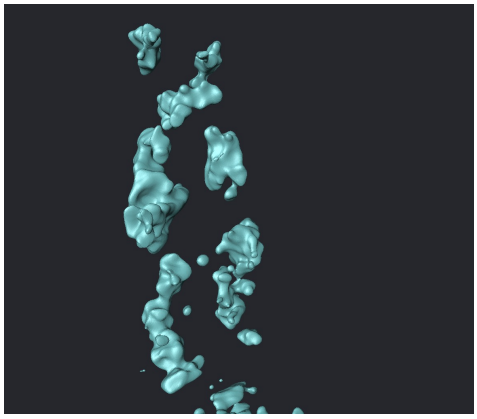

Figure 5.4: Unseparated pores due to a too large acceptance value for merging neighbouring voxels to a single object (i.e. pore).

5.3 Size distributions

The segmented pores were analysed with some of the Avizo Fire built in functions. The particle frequency distribution shows the percentage of particles within a predefined size range (bin) [51]. Each pore generated during the rendering process (see above) is linked to a unique number, each individual pore (object) can be analysed. For the total number of pores, the number of individual objects is simply summed up and for the volume of each pore the incorporated voxels are counted. In addition, the equivalent diameter for each pore was calculated by Avizo. The equivalent diameter is used to report the particle sizes and reflects the diameter when the shape of the pore was an ideal sphere. Based on these three very basic measures, the size distribution of pores can be plotted volume- or number-weighted as bar or line chart. In Fig. 5.5-5.8 the 3D image and the related size distributions are displayed volume and number-based for each of the samples. The volume-based distributions reflect the coalescence and coarsening of the pores (with time) very good while the number-based distribution is shifted only slightly to larger radii. The sample tested at 130 MPa has its failure location outside the heat affected zone and thus a volume based size distribution gives no additional information. The diagram in Fig. 5.5 shows that most of the pores are distributed between 5 and 40 µm equivalent diameter and that only a small percentage has a higher equivalent diameter than 40 µm. The graphs represent always the final time step of the evolution of pores from the begin to the end of the creep test. The other graphs in Fig. 5.6-5.8 show even more explicitly a bimodal distribution. This means that the distribution function of the relative volume has two distinct (local) maxima and thus the obtained distribution is the overlay of the different functions. The graphs therefore quantitatively express what can be seen from the 3D images, at the end of the creep test, larger pores due to coarsening and coalescence and small, new generated pores define the shape of the distribution.

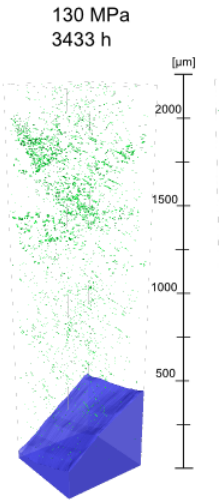

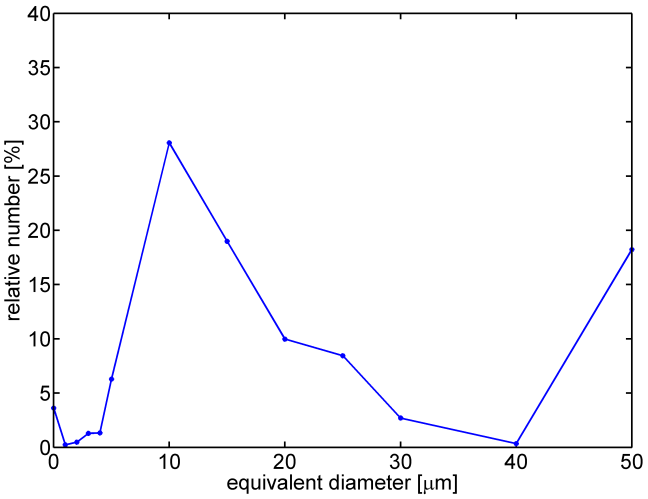

Figure 5.5: Number based size distribution for sample creep tested at 650 °C and 130 MPa.

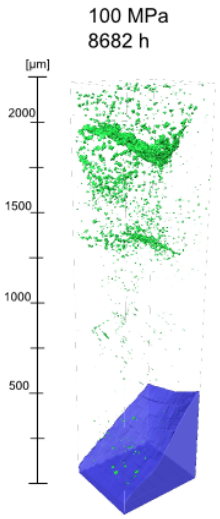

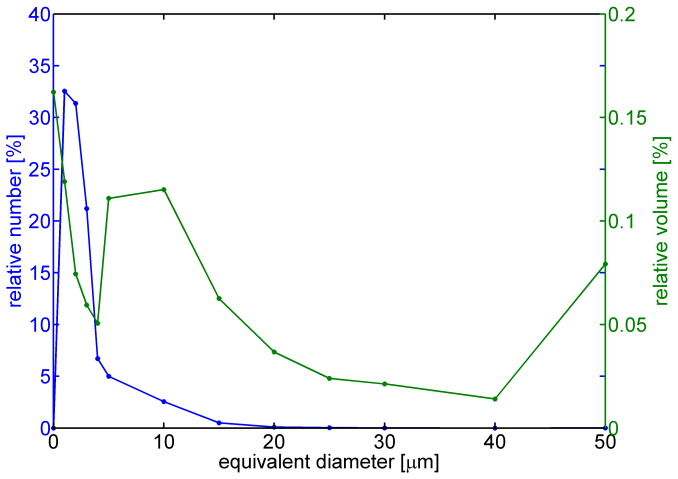

Figure 5.6: Comparison of the volume and number based size distribution for sample creep tested at 650 °C and 100 MPa.

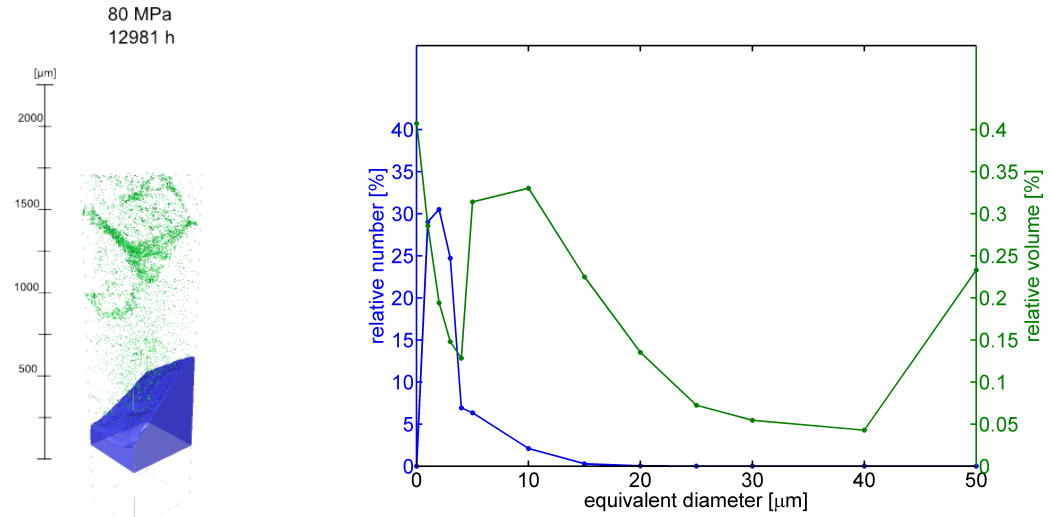

Figure 5.7: Comparison of the volume and number based size distribution for sample creep tested at 650 °C and 80 MPa.

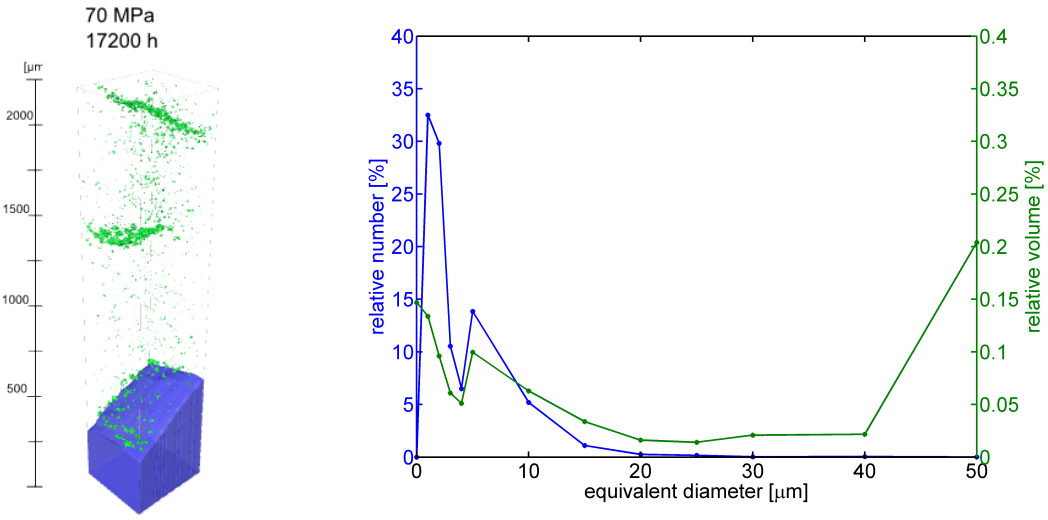

Figure 5.8: Comparison of the volume and number based size distribution for sample creep tested at 650 °C and 70 MPa.

5.4 3D reconstruction

Besides the quantitative analysis, also a qualitative analysis of the pore distribution is of interest. The very small sample size and the sample extraction process itself do not allow to achieve reproducible and exact positions for the sampling. The individual data sets therefore differ in the volume fraction of weld metal. The 80 MPa-creep sample contained the largest fraction of weld metal and was cropped to a desired region of interest, the 3D image height is thus reduced compared to the other images.

All reconstructed samples are shown in Fig. 5.9 in relation to the respective stress levels.

130 MPa The pores are comparably small and homogeneously distributed, at a distance of ≈ 700 µm from the weld metal, there are very few pores. The initial stadium of pore accumulation in the upper part of the HAZ may be identified around 1500 µm on the scale bar.

100 MPa Coarse pores and severe accumulation and coalescence around 1700 µm on the scale bar, again only a few pores in the region between fusion line and the accumulated region.

80 MPa The smaller HAZ region extracted does not allow to make a statement about the pore distribution at the position of the above samples, the pore accumulation is slightly shifted towards the fusion line.

70 MPa The number density of pores exhibits three peaks, one at the fusion line and two at a distance comparable to the sample of 130 and 100 MPa.

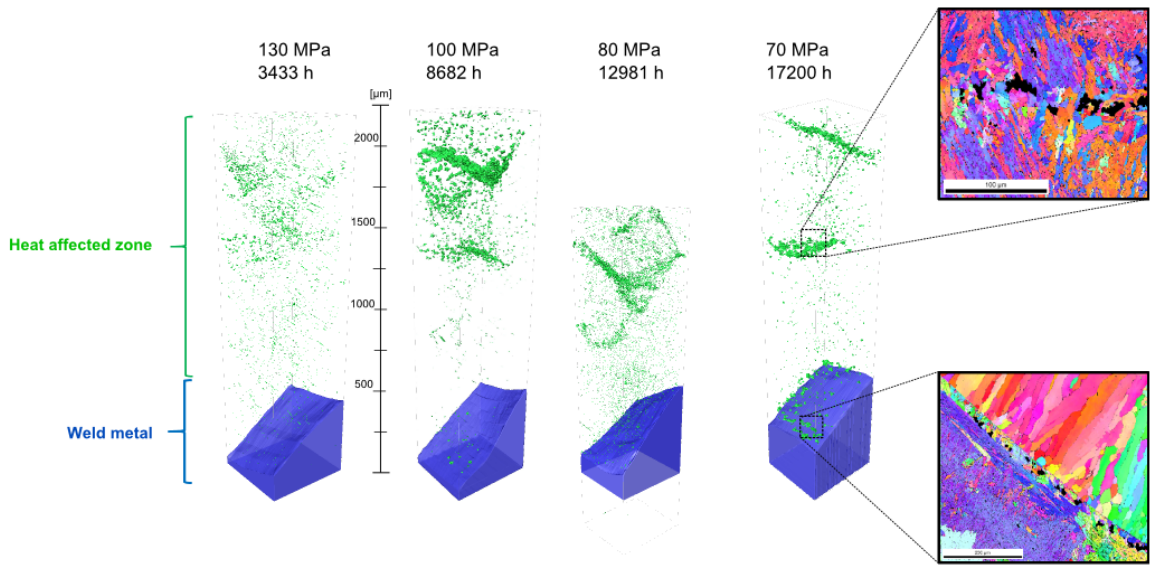

Figure 5.9: 3D micro-CT images of the creep tested crosswelds with supporting EBSD measurements.

The dimensions of the bounding box (the box determined by the number of pixels in x,y,z-direction) is in the x,y-plane (along a single slice) in the order of 400 µm, which

is also in the range of the grain size of the samples [1]. Additional EBSD measurements which were performed for the 70 MPa-sample, allowed to link the pore formation to fine grains present at the prior austenite grain boundaries. It is concluded, that these fine grains introduced by the weld thermal cycle increase the number of possible nucleation sites for pores. In parallel, the number of evolving precipitates is humble due to the shortness of the weld thermal cycle and so the grain boundaries are not pinned which favours grain boundary sliding.

[1] The grain size of the material used in the experimental part of this work could not be determined, but was estimated with 350 μm.

6 Summary and Conclusion

The results of all experiments and tests performed within the framework of this thesis have been discussed in the previous two chapters in the corresponding sections. These results are summarised in the following and some additional aspects are discussed further on. At first, extensive preliminary weldability trials have been carried out for selecting and optimising the EB welding parameters for the provided martensitic 9% Chromium steel. The accelerating voltage has been chosen to be constant and 120 kV based on a prior internal field study. The welding parameters which have been varied are the following:

- The beam current controls the beam diameter and thus the volume of molten metal and the stability of the weld pool, furthermore it influences the weld metallurgy by the applied thermal cycle (solution of precipitates)
- The welding speed acts together with the beam current and the accelerating voltage on the total line energy and thus on the penetration depth, determines the shape of the isothermal curves around the heat source and also influences the weld quality (heat cracks, porosity)

The influence of the different parameters with regard to the soundness, microstructure development and reproducibility was investigated for a 9%Cr MARBN steel plates with a thickness of 25 mm. In addition, the transferability of the welding parameters between the material of slightly different chemical composition but same thickness was investigated. It can be concluded that the obtained weldments are very reproducible, but the applicable parameter window is quite narrow. Higher welding speeds caused the entrapping of gas pores and also lead to micro- and end-crater cracks. The pores

already present in the material together with Nitrogen influence the weld quality to a large extent. The effect of beam oscillation on the de-gassification is reported positively in literature [27] but has not been investigated here. The final optimised weld parameters have been set after an extensive blind weld and butt weld study and subsequent characterisation of the weldment and are summarised in the following table:

Table 6.1: Final optimised parameter set used for butt welding of MARBN steel

Parameter	**Value**
Accelerating voltage	120 kV
Beam focus	focus on sample surface
Beam modulation figure	circle
Beam oscillation	600 Hz
Beam oscillation amplitude	x = y = 0.5 mm
Beam current	65 mA
Welding speed	8 mm/s
Plate thickness	25 mm

The metallographic investigations showed that the obtained microstructure does not contain any delta ferrite except for the molten zone. A coarse zone is visible close to the fusion line but the prior austenite grain boundaries could be brought out by etching. The microhardness results show that the hardness increased from the base material to the HAZ from about 280HV10 to 400HV10 and increased further to 420HV10 at the fusion line. The average hardness in the weld metal did not exceed 475HV10.
Since no filler metal is used, the PWHT is a very important parameter to further affect the weld properties. The applied PWHT reduced the hardness gradient so that the average hardness in the base material was 235HV1 and the maximum value obtained in the weld metal was 300HV1. The tensile test of a cross welded samples at room temperature lied with their yield strength of ($\approx$ 615 MPa) in the order of the base material (after QHT). The fracture occurred clearly recognisable in the base material. Overall, the microstructure investigations and the results from mechanical testing are promising for the future creep testing. Compared to other 9% Cr steels welded with conventional arc melting process, the width of the heat affected zone is significantly smaller and thus also the different subregions are restricted to even smaller areas. On the other hand the microstructure of EB weldments in the heat affected zone is finer due to the very high cooling rates. This unwanted effect is expected to be partly

compensated by the addition of Boron and Nitrogen countermeasuring the boundary sliding suppressing the fine grained heat affected zone. Thus a better creep behaviour than obtained with other welding procedures is expected.
The simulation of the heat affected zone using the Gleeble QuickSim system revealed suitable results. However, the region near the fusion line with temperatures above 1100 °C could not be simulated due to the very high heating and cooling rate. The maximum cooling rate determined by $t_{8,5}$ time was 6 s. The originally envisaged sample diameter of 16 mm yield to be too high to achieve this cooling rate, and was thus reduced to 10 mm. The direct comparison between the thermally simulated heat affected zones and the microstructure obtained with EBW yield to be difficult and requires further investigation.

The experimental work was supplemented with the data evaluation of synchrotron micro-CT measurements of GTAW crosswelded creep samples which have been tested at 650 °C and different stress levels. The measurement principle together with software-based 3D image analysis is a powerful tool to analyse particle size distributions. Quantitative and qualitative data for the HAZ in the opposite side of the failure as well as for distinct pores is obtained. However, the data requires pre-processing to reduce image artefacts and simplify the segmentation process. The ring correction tool presented by [49, 52] was found to be very viable but requires contrast enhancement afterwards. The separation of pores should be of particular attention to avoid over- or underestimation of the actual pore size distribution and number density. Furthermore, it is highly recommended to choose a small region of interest for analysis which requires a high amount of computations.
In general, a clear trend for the location of failure shifting from the base material towards the fusion line with decreasing stress level could be observed. Despite the different location of failures, a certain distance in the order of $\approx 1500\mu$m from the fusion line could be identified as favorite site for pore formation, coarsening and coalescence. Nevertheless the number density and their size distribution in this region are differently pronounced depending on the applied stress. The evaluation volume-weighted pore distribution is bimodal which is explained by the overlap of two different pore size distribution. One is covering the formation of new pores with high sphericity and low equivalent diameter and is overlaid by the existing pores which coarsen and coalesce. The dimension of the three dimensional volume analysed is in the order of magnitude of the prior austenite grains. Thus, the intense void formation in restricted areas could be related by additional EBSD measurements to small grains located at prior austenite grain boundaries. Parts of this particular analysis have been published in [47].

Outlook

In a next step the creep behaviour of the optimised butt welds obtained during this work as well as the samples with a simulated heat affected zone shall be investigated at creep conditions which allow comparison with the existing data. The determination of the grain size in the different zones of the weldment in the PWHT condition proofed to be rather difficult and did not yield any results. A measurement of the grain size using alternative methods such as EBSD is required. A further characterisation of the weldment by Charpy or side bend testing as well as further investigation of the microstructure in the molten and heat affected zone in view of grain size and evolution of precipitates, will supplement the existing measures. The investigation of entrapment of gas pores caused by ascending inherent (pre-existing) pores or by degassing of alloying elements such as Nitrogen may proof to be meaningful. The selection of measurements to correlate the obtained weld quality with the material, thickness and parameters may be extended to a larger range.
The Avizo Fire software is a powerful tool for 3D image analysis and may be used to supplement 2D measurements. A lot of filter and analysis tools do not limit the application to solely computed-tomography data but also allow for example FIB image analysis. In addition the visual representation of the data is advanced and allows the generation of videos. Further quantitative analysis of the present data is possible as well as the analysis of the future data obtained from the above EB welded creep samples. The Software package might also be of interest for other IWS research groups, it supports the implementation of Matlab code which can be used for creep damage modelling.

Acknowledgement

The often arising general question “where shall I begin”, which is also related to this section, has been concisely answered by the King of Hearts who is a character from Lewis Caroll’s novel Alice’s Adventures in Wonderland. The following text is structured in order to follow this wise piece of advice.

Begin at the beginning . . .

I thank Univ.-Prof. Dipl.-Ing. Dr.techn. Christof Sommitsch for giving me the opportunity to write this master thesis at the Institute for Materials Science and Welding.
I was provided with two supervisors, Coline Béal and Christian Schlacher, who are very qualified in both counts, the professional but also the personal level. The prospects for a good start in the research topic of 9% Cr steels are provided by the longstanding research expertise of the Institute in this field and the associated experience from which I did benefit.
I see it as a high priviledge to concentrate most of my energy and time in a topic I am very fascinated of – the academic research of materials and related scientific questions – and I thank my parents Josef and Karin Pelzmann for enabling me to do so as well as for their lovingly support.

and go on till you come to the end:

On the way to this final written form of my thesis, I have spent countless hours in the laboratory. I thank the laboratory team under the direction of Kurt Kerschbaumer who readily provided information at any time and helped me in machining the samples. The professional exchanges and dialogs with my collegues at the institute have also contributed to my work. In particular, I want to express my thanks to Surya Deo

Yadav and Romain Bureau for a lot of good conversations and their help. Many of our "coffee & discussion"-meetings have contributed in solving questions and inspired me. Not to forget about the regular IWS squash games, which were the perfect ending to long days in the laboratory. Special thanks go to Thomas Galli-Magerl and Edina Monsoon, who have provided the final touches to my text and to Martin Schwinzerl for his feedback helping me to improve some of the sections.

then stop.

Although this may sound like a simple enough task, the right point to stop in an experimental work is not always evident. At this point, I want to express again my thanks to Coline and Christian, for their fair and professional feedback and for helping me to identify the end to stop. All that remains is to thank my partner Martin Luckabauer for asking the "good" questions, supporting me in manifold ways and for his patience especially in the last period of my work.

Bibliography

[1] J. Ahrendts, *Das Ingenieurwissen: Technische Thermodynamik* -. Wiesbaden: Springer Berlin Heidelberg, 2014. aufl. ed., 2013.

[2] H. J. Schüller, L. Haigh, and A. Woitscheck, "Cracking in the weld region of shaped components in hot steam lines - materials investigations," *Der Maschinenschaden*, vol. 47, no. 1, 1974.

[3] A. I. H. Committee and D. Olson, *ASM handbook: Welding, brazing, and soldering*. ASM Handbook, ASM International, 1993.

[4] M. Yoshimo, "Precipitation behaviour of mx carbonitride in high cr ferritic steels," in *Performance and Requirements of Structural Materials for Modern High Efficient Power Plants*, pp. 127–138, 2005. International Workshop.

[5] B. Sonderegger, *Charakterisierung der Substruktur in modernen Kraftwerkswerkstoffen mittels der EBSD Methode*. Institute for Materials Science and Welding, TU Graz, 2005. PhD Thesis.

[6] E. Letofsky, *Das Verhalten von Schweißverbindungen moderner Kraftwerkswerkstoffe*. Institute for Materials Science and Welding, TU Graz, 2001. PhD Thesis.

[7] A. Shibli and D. G. Robertson, *A Review of Martensitic 9-12% Chromium Steels for Elevated Temperature Service*. Materials and Data Review, European Technology Development Ltd - UK, January 2011. final report.

[8] M. Donachie, *Superalloys: A Technical Guide*. ASM International, 2002.

[9] K. E. Easterling, *Introduction to the physical metallurgy of welding*. Butterworth Heinemann, 2 ed., 1992.

[10] H.-J. Bargel and G. Schulze, *Werkstoffkunde*. Düsseldorf: Springer, fifth ed., 1988.

[11] P. Mayr, *Evolution of microstructure and mechanical properties of the heat affected zone in B-containing 9% chromium steels*. Institute of Materials Science, Welding and Forming, TU Graz, 2007. PhD Thesis.

[12] J. Rösler, H. Harders, and M. Bäker, *Mechanisches Verhalten Der Werkstoffe -*. Berlin Heidelberg New York: Springer-Verlag, 4. edition 2012 ed., 2012.

[13] J. Cadek, *Creep in metallic materials*. Amsterdam: Elsevier, 1988.

[14] G. Gottstein, *Physikalische Grundlagen der Materialkunde*. London: Springer London, Limited, 2007.

[15] M. Hacksteiner, *Microstructure characterization and heat treatment simulation of a modern 9%Cr steel for the use in thermal power plants*. Institute of Materials Science and Welding, TU Graz, 2010. Bachelor Thesis.

[16] D. J. Abson and J. S. Rothwell, "Review of type iv cracking of weldments in 9 – 12% cr creep strength enhanced ferritic steels," *International Materials Reviews*, pp. 437–473, November 2013.

[17] J. A. Francis, W. Mazur, and H. K. D. H. Bhadeshia, "Type iv cracking in ferritic power plant steels," *Materials Science and Technology*, vol. 22, no. 12, pp. 1387–1395, 2006.

[18] M. Kondo, M. Tabuchi, S. Tsukamoto, F. Yin, and F. Abe, "Suppressing type iv failure via modification of heat affected zone microstructures using high boron content in 9cr heat resistant steel welded joints," *Science and Technology of Welding and Joining*, vol. 11, no. 2, pp. 216–223, 2006.

[19] F. Abe, M. Tabuchi, M. Kondo, and S. Tsukamoto, "Suppression of type iv failure and improvement of creep strength of 9cr steel welded joints by boron addition," *International Journal of Pressure Vessels and Piping*, vol. 84, pp. 44–52, 2007.

[20] Y. Liu, S. Tsukamoto, K. Sawada, and F. Abe, "Role of boundary strengthening on prevention of type iv failure in high cr ferritic heat-resistant steels," *Metallurgical and Materials Transactions A*, vol. 45A, pp. 1306–1314, March 2014.

[21] F. Abe, "Precipitate design for creep strengthening of 9%cr tempered martensitic steel for ultra-supercritical power plants," *Science and Technology of Advanced Materials*, vol. 9, 2008.

[22] Y. Liu, S. Tsukamoto, T. Shirane, and F. Abe, "Formation mechanism of type iv failure in high cr ferritic heat-resistant steel-welded joint," *Metallurgical and Materials Transactions A*, vol. 44A, pp. 4626–4633, October 2013.

[23] F. Abe, "Effect of boron on microstructure and creep strength of advanced ferritic power plant steels," *Procedia Engineering*, vol. 10, pp. 94–99, 2011.

[24] P. Ernst, *Effect of boron on the mechanical properties of modified 12%Chromium steels*. Eidgenössische Technische Hochschule Zürich, 1988. PhD thesis ETH No. 8596.

[25] G. B. u. C. W. W. (Kapfenberg), *Böhler Edelstahl-Handbuch*. Freuburg i.B.: Böhler Edelstahl GmbH & Co KG, 1998.

[26] H. Semba and F. Abe, "Alloy design and creep strength of advanced 9%cr usc bioier steels containing high boron," *Materials for Advanced Power Engineering*, p. 1041, 2006. Liege Conference,Part II.

[27] J. C. von Wortel and C. Coussement, "Optimisation of creep behaviour of welded components in modified 9%cr," *European Commission / Technical Steel Research*, 1994. Final report.

[28] K. Kussmaul, D. Blind, P. Deimel, and W. Gaudig, "Mechanical properties and structure of electron beam welds in alloy fe-0.2%c-12%cr-1%mo," *Welding Research Supplement*, pp. 267–272, September 1984.

[29] T. Tabuchi, M.and Watanabe, K. Kubo, J. Matsui, M.and Kinugawa, and F. Abe, "Creep crack growth behavior in the haz of weldments of w containing high cr steel," *International Journal of Pressure Vessels and Piping*, vol. 78, pp. 779–784, 2001.

[30] D. Allen. private communication, 2013–2014.

[31] G. Alkan, *Grundrisse der Gefügeausbuldung und der Zeitstandeigenschaften martensitischer 9-12% Chromstähle*. Eidgenössische Technische Hochschule Zürich, 1997. PhD Thesis.

[32] R. Rai, *Modelling of Heat Transfer and Fluid Flow in Keyhole Mode Welding*. The Pennsylvania State University, 2008. PhD Thesis.

[33] A. I. H. Committee, T. Lienert, T. Siewert, A. S. for Metals. Joining Division, S. Babu, and V. Acoff, *ASM Handbook: Welding Fundamentals and Processes*. ASM Handbook, Asm International, 2011.

[34] V. Adam, C. U., D. v. Dobeneck, T. Krüssel, and T. Löwer, *Elektronenstrahlschweißen - Grundlagen einer faszinierenden Technik*. pro-beam AG & Co. KGaA, 2011.

[35] DVS - DEUTSCHER VERBAND FÜR SCHWEISSEN UND VERWANDTE VERFAHREN E.V., ": Empfehlungen zum reinigen der fügezone für das elektronenstrahlschweißen," *Merkblatt DVS 3213*, June 2010.

[36] K. Lachenber, P. Hochanadel, and J. Elmer, "Design considerations for electron beam welding," in *ASM Handbook; Welding Fundamentals and Processes*, vol. 6A, pp. 522–539, ASM International, 2011.

[37] F. Pengfei, M. Zhiyong, Z. Congjin, W. Yajun, and W. Chunming, "Microstructures and fatigue properties of electron beam welds with beam oscillation for heavy section tc4-dt alloy," *Chinese Journal of Aeronautics*, no. 0, pp. –, 2014.

[38] H. Schultz, *Elektronenstrahlschweißen*. Fachbuchreihe Schweisstechnik, DVS-Verlag, 2000.

[39] D. D. S. Inc., *Gleeble Systems and Applications*, 2010. Gleeble Users Training 2010.

[40] D. Radaj, *Heat Effects of Welding - Temperature Field, Residual Stress, Distortion*. Wiesbaden: Springer Berlin Heidelberg, 2012.

[41] D. Radaj, *Schweißprozeßsimulation: Grundlagen und Anwendungen*. Fachbuchreihe Schweisstechnik, Verlag für Schweißen und Verwandte Verfahren, DVS-Verlag, 1999.

[42] N. N. Rykalin, *Die Wärmegrundlagen des Schweißvorganges - d. Wärmeausbreitungsvorgänge bei der Lichtbogenschweißung*. Berlin: Verlag Technik, 1952.

[43] American Association of State Highway and Transportation Officials; American Society for Testing and Materials, *E8M-04 Standard Test Methods for Tension*

Testing of Metallic Materials (Metric)1 -. West Conshohocken: ASTM International, 2004.

[44] J. Radon, "Über die bestimmung von funktionen durch ihre integralwerte längs gewisser mannigfaltigkeiten," in *Berichte über die Verhandlungen der Königlich Sächsischen Gesellschaft der Wissenschaften*, vol. 69, pp. 262–277, Mathematisch-Physikalische Klasse, 1917.

[45] P. Mayr *et al.*, "Critical issues with creep-exposed ferritic-martensitic welded joints for thermal power plants," *Proc. of IIW Int. conf. on 'Global Trends in Joining, Cutting and Surfacing Technology'*, pp. 417–425, July 2011.

[46] Y. Tanabe, "Investigation of behavior for improved p92 steel." Internal Report, Institute for Materials Science and Welding, TU Graz, 2013.

[47] C. Schlacher, T. Pelzmann, C. Béal, C. Sommitsch, C. Gupta, H. Toda, and P. Mayr, "Investigation of creep damage in advanced martensitic chromium steel weldments using synchrotron x-ray micro-tomography," *Materials Science and Technology*, 2014. Under review.

[48] W. Rasband, "Imagej." http://imagej.nih.gov/ij/, 1997-2014.

[49] A. Lyckegaard, G. Johnson, and P. Tafforeau, "Correction of ring artifacts in x-ray tomographic images," *International Journal of Tomography & Simulation*, vol. 18, no. F11, pp. 1–9, 2011.

[50] A. Haibel, *μ-Tomography of Engineering Materials. In Neutrons and Synchrotron Radiation in Engineering Materials Science.* Wiley-VCH Verlag GmbH & Co. KGaA, 2008.

[51] G. van Daalen and M. Koster, "2d & 3d particle size analysis of micro-ct images," in *Proceedings of the SkyScan Micro-CT User Meeting*, 2013. Brussels / Belgium.

[52] A. Lyckegaard, *Development of tomographic reconstruction methods in materials science with focus on advanced scanning methods.* Risø DTU National Laboratory for Sustainable Energy, June 2011. Risø-PhD-73(EN).

[53] G. V. Voort, "Committee e-4 and grain size measurements: 75 years of progress," *ASTM Standardization News*, May 1991.

[54] S. Hasse, *Guß- und Gefügefehler: Erkennung, Deutung und Vermeidung von Guß-*

und Gefügefehlern bei der Erzeugung von gegossenen Komponenten. Schiele & Schön, 2003.

[55] R. Honig and D. Kramer, "Vapor pressure data for the solid and liquid elements," *RCA Review*, vol. 30, pp. 285–305, 1969.

A Appendix

The objective of this thesis with regard to the empirical optimisation of welding parameters for a given material with given thickness, as well as the extensive synchrotron data evaluation of crosswelded creep samples lead to a large amount of data and results. Many of the measurements and experiments served only one purpose, to observe a trend in the weld quality and to define the next parameters. It does not seem to be useful to present all performed measurements and results therefore. On the contrary, some of the results or conclusions might be useful for further investigations or measurements, even though they do not account primarily to the aim of this thesis. Additionally, some measurement procedures and parameters are documented in the appendix in the manner of a manual to save time of trial and error and to document some useful observations.

The following sections are incorporated in the Appendix:

A.1 Comparison of Etchants to Yield PAGB in Heat Treated MARBN

A.2 Phase-Fraction-Diagrams

A.3 Prior Weldability Study and Initial Test Run

A.4 EDX - Analysis of Tensile Sample Inclusion

A.5 JMat-Pro calculations

A.6 Gleeble®-3800 QuikSim / Heat Affected Zone Programming

A.7 Vapor Pressure Data

A.1 Comparison of Etchants to Yield PAGB in Heat Treated MARBN

The grain size of the martensite structure in heat treated steels turns out to be not easily accessible because of the absence of any convenient structural shape. The martensite lath structure is build within a parent austenite grain in form of packets. Therefore, it is often tried to measure the size of the prior austenite grain boundaries instead. In order to reveal these grain boundaries etching is required and many etchants have been developed for this purpose. Nevertheless the etching process has proved very difficult and did not yield an etch quality adequate for imaging but caused substantial pitting. [53]
The material investigated in the present work exhibited an inconsistent etching behaviour, making it difficult to obtain an even etched surface. A heat treatment reduced the etching time in general, in some cases to more than the half compared to the sample without heat treatment. The method described in the following provided satisfactory results in most of the cases. For some samples, especially in the heat treated condition, Vilella's Reagent (picric acid) in which the sample is dipped at room temperature gave also good results. At the end of this section, a comparison for different etchants, different contact times, and different applications (wipe or dip) is shown in Fig. A.1 to Fig. A.8. In general, it was observed, that the dipped samples exhibited a more homogenous reaction to the etchant and that long vibrational polishing is preferable. However, none of the tested etchants satisfactorily developed the PAGB.

modified Lichtenegger's and Bloech's reagent

Composition: 100 ml distilled water
0.75 g $(NH_4)HF_2$ (ammonium hydrogen fluoride)
0.90 g $K_2S_2O_5$ (potassium disulfite)

The distilled water is warmed to 50°C, then ammonium hydrogen fluoride and potassium disulfite are added. Stir the solution for about 5 minutes using magnetic stir bars or a glass rod. The sample surface should be polished up to 1 μm, vibrational polishing is recommended. Before the sample is dipped in the etchant, the surface should be wet with distilled water to improve the etching process. The contact time is about 3-5 s. Under-etched sample require repolishing of the surface before etching it again. The etchant has a limited shelf life of 2-3 hours.

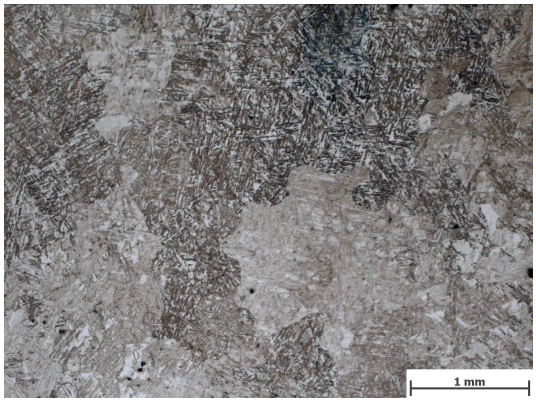

Figure A.1: Vilalla, 30 s, wiped

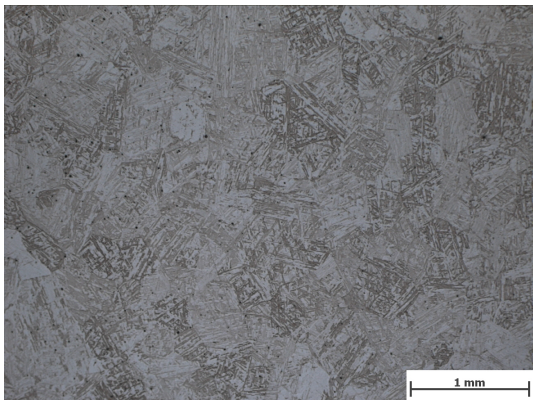

Figure A.2: Vilella, 35 s, wiped

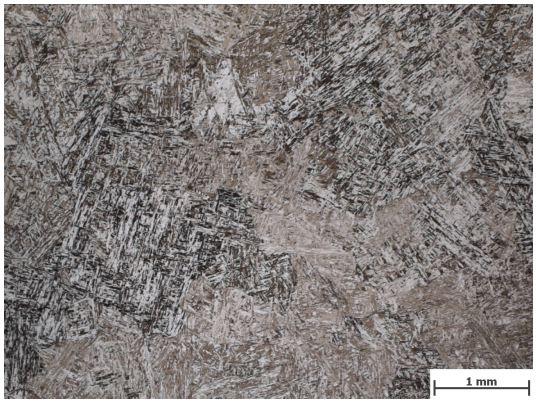

Figure A.3: Vilalla, 50 s, wiped

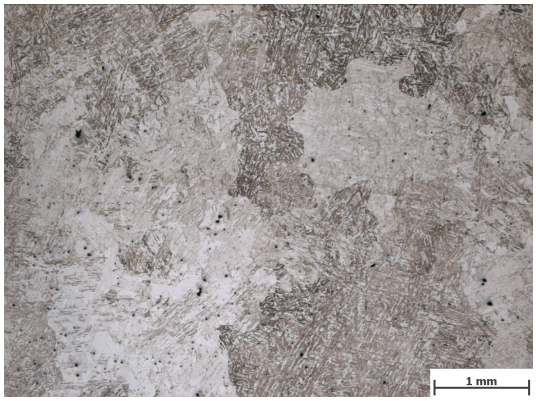

Figure A.4: Vilella, 50 s, dipped

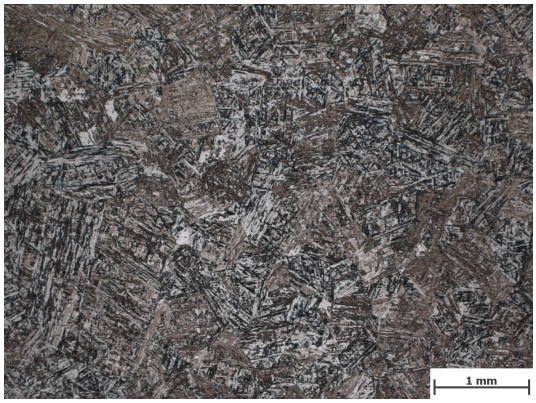

Figure A.5: Vilalla, 65 s, wiped

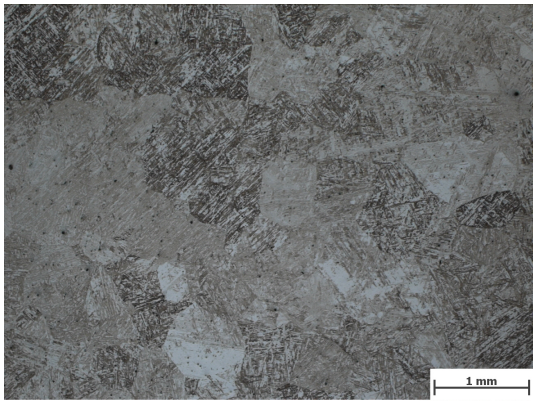

Figure A.6: Vilella, 65 s, dipped

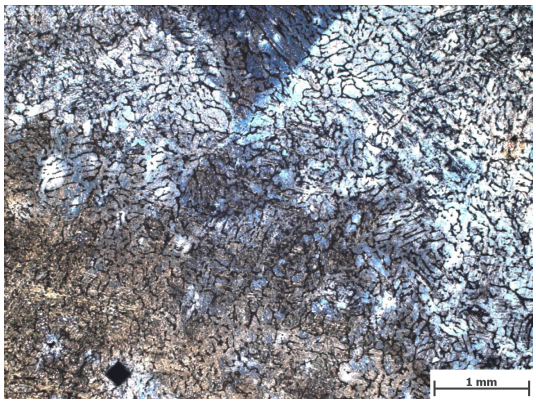

Figure A.7: Beraha I, t<5 s, dipped

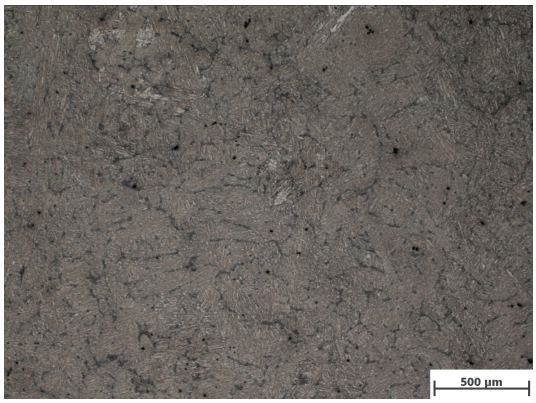

Figure A.8: Beraha I, t<5 s, dipped

A.2 Phase-Fraction-Diagrams

The change of fractions with temperature for potential phases were calculated based on the chemical composition for both steel test plates using the software tool MatCalc. The related arrest points for the start and end of the austenitisation according to this calculation are:

Material	$\mathbf{A_{C1}}$ [°C]	$\mathbf{A_{C3}}$ [°C]
WTP	805	833
MTP	812	886

The onset temperature of the liquid phase is around 1370 °C for both materials, above 1500 °C 100% liquid phase is obtained in the case of equilibrium.

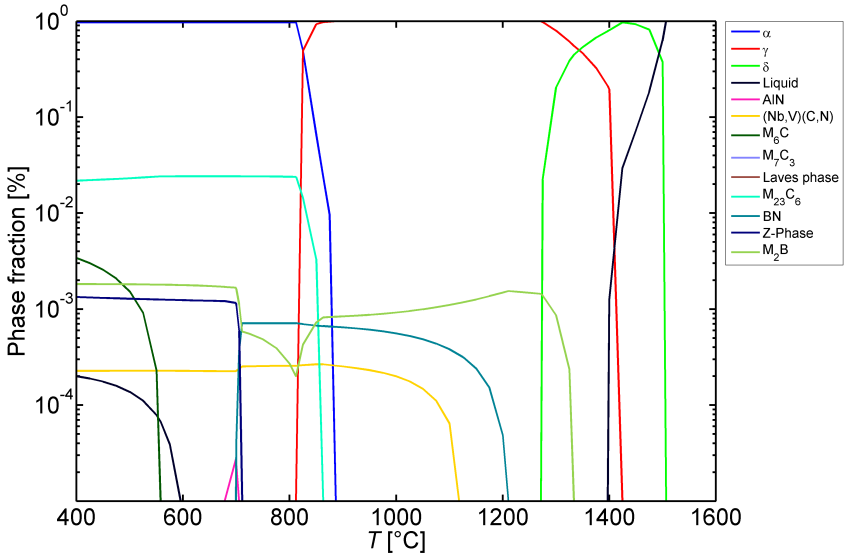

Figure A.9: Phase fraction diagram of the material test plate material calculated with the MatCalc software package

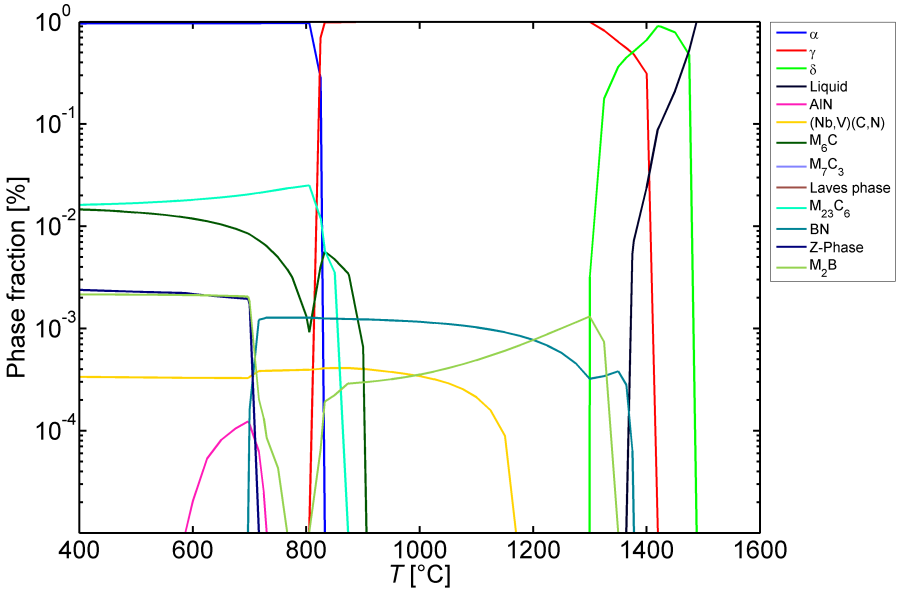

Figure A.10: Phase fraction diagram of the weld test plate material calculated with the MatCalc software package

A.3 Prior Weldability Study and Initial Test Run

Data from a prior weldability study on an optimized P92 steel were available. The material used and the condition can be summarized as follows:

optimized P92 (MNB2603)

Boron :	70 ppm
Nitrogen :	1030 ppm
thickness :	22 mm
annealing :	25 min @1070°C
tempering :	25 min @780°C

The welding parameters listed in the table below correspond to an accelerating voltage of 120 kV, a beam oszillation of 600 Hz and a circle as beam figure with an amplitude of 0.5 in x and y-direction. For the given material and the given thickness t=22 mm parameter set #3 gave the best results.

Table A.1: Blind weld parameters for an optimized steel P92. Tests performed by Y. Tanabe

No	**U [kV]**	**I [mA]**	**v [mm/s]**	**E [W/cm]**	**Fl [mA]**	**d(circle)**	**f [Hz]**
1	120	60	8,5	8,47	0	0,5	600
2	120	60	8,5	8,47	0	0,5	600
3	120	55	8	8,25	0	0,5	600

A new parameter-set for a plate of comparable thickness (t=21 mm) but with unknown composition and condition was created based on this best parameter #3. The values vor the beam current and velocity were increased and decreased with respect to the "optimum" parameter and resulted in 22 exploratory blind weld test. From all parameters tested, as outlined in Fig. A.11, #2, #6, and #7 yield the best results and are coincident with the above best parameters of the P92 weldability study.

Table A.2: Exploratory EBW-Weld Tests for an arbitrary steel plate with t=12 mm.

No	U [kV]	I [mA]	v [mm/s]	E [W/cm]	FL [mA]	d(circle)	f [Hz]
1	120	55	8,5	7,76	0	0,5	600
2	120	55	9	7,33	0	0,5	600
3	120	55	8	8,25	0	0,5	600
4	120	55	8	8,25	-2,5	0,5	600
5	120	55	8	8,25	0	0,3	600
6	120	55	8,5	7,76	0	0,5	600
7	120	55	9	7,33	0	0,5	600
8	120	55	9,5	6,95	0	0,5	600
9	120	55	10	6,60	0	0,5	600
10	120	57	8	8,55	0	0,5	600
11	120	57	8,5	8,05	0	0,5	600
12	120	57	9	7,60	0	0,5	600
13	120	60	8	9,00	0	0,5	600
14	120	60	8,5	8,47	0	0,5	600
15	120	60	9	8,00	0	0,5	600
16	120	60	9,5	7,58	0	0,5	600

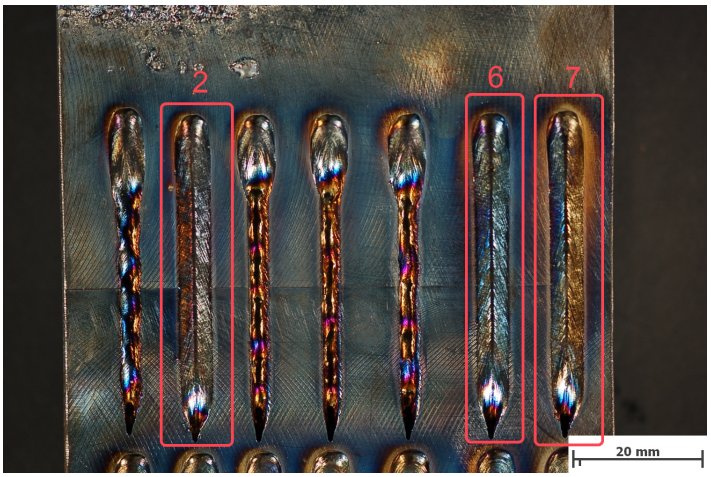

Figure A.11: Selection of best parameters from test run

A.4 EDX - Analysis of Tensile Sample Inclusion

After the quality heat treatment, a part of the weld test plate was machined to tesile test samples as described in 4.1. Altogether three samples of the weld test plate in this condition were tested at room temperature, but one sample (indicated by the black

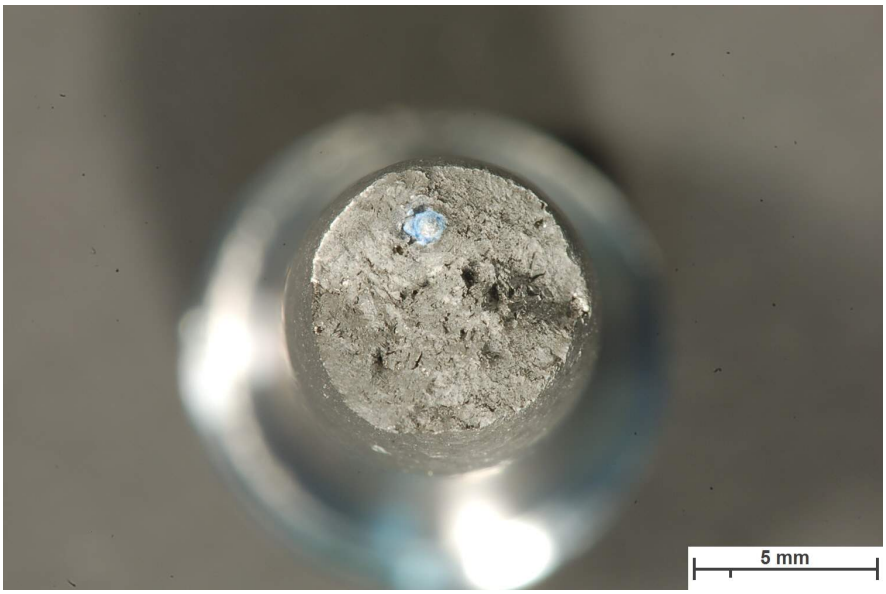

Figure A.12: Picture of the inclusion which is visible as a light blue particle.

curve in Fig. 4.12) exhibited a significantly smaller breaking elongation. The investigation of the fractured surface permits the conclusion that an non-metallic inclusion lead to the premature failure. The inclusion is clearly visible to the naked eye (see Fig. A.12) and was broke in two. The LEO 1450 VP Scanning Electron Microscope available at the institute is additionally equipped with a Röntec EDX (energy dispersive X-ray analysis). The characteristic x-ray emission was detected using the spotscan technique to record the EDX spectrum for a found inclusion. An EDX analysis was performed to gain more information about the particle. The upper part of the broken tensile sample was cut to allow the sample positioning on the SEM sample stage. A spotscan was recorded on the particle as well as on the surrounding metallic matrix, the scanned areas are highlighted in the below figures. The data acquisition requires that the electron beam is directed to a specific spot, the size of spot is determined by the focus spot of the beam, and retained. The X-rays generated by the beam-sample interaction are recorded, but the hold time has to be long enough to achieve a good signal-to-noise ratio. The high intensity oxygen peak which is accompanied by an Al, Ca Cr, and Si peak suggests that the inclusion is a conglomerate of seraval different chemical compounds. Aluminium, Silicon, and Chromium have a high chemical affinity to oxygen and thus tend to form insoluble oxide layers during the casting process. Aluminium and Silicon are used as deoxidising agents and added to the steel in the casting process, the resulting oxidic inclusions often are made up of MnO-Al_2O_3-SiO_2 compound [54]. A high SiO_2 content will lead to a glassy apperance and a more globular shape as it is the case for the inclusion found.

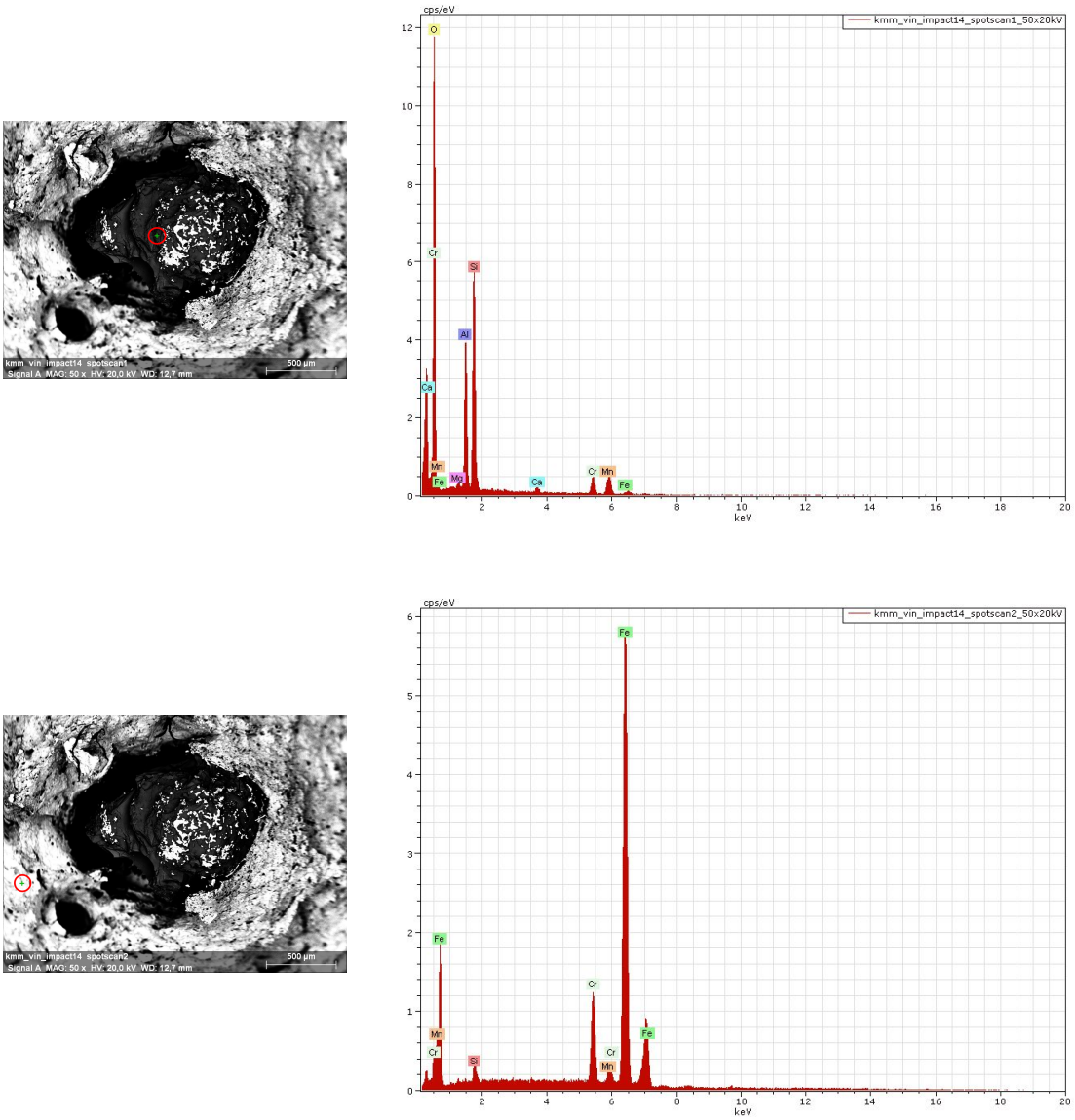

Figure A.13: EDX Analysis of the inclusion found in one tensile sample of the weld test plate after quality heat treatment (first row) and the surrounding base material (second row). The sample was analysed using the spotscan technique and the related spots are highlighted.

A.5 JMat-Pro calculations

The Gleeble HAZ QuikSim requires entries for the physical propertiy of the material. Since none of the data was available, JMat-Pro calculations based on the chemical composition of the weld test plate were performed.

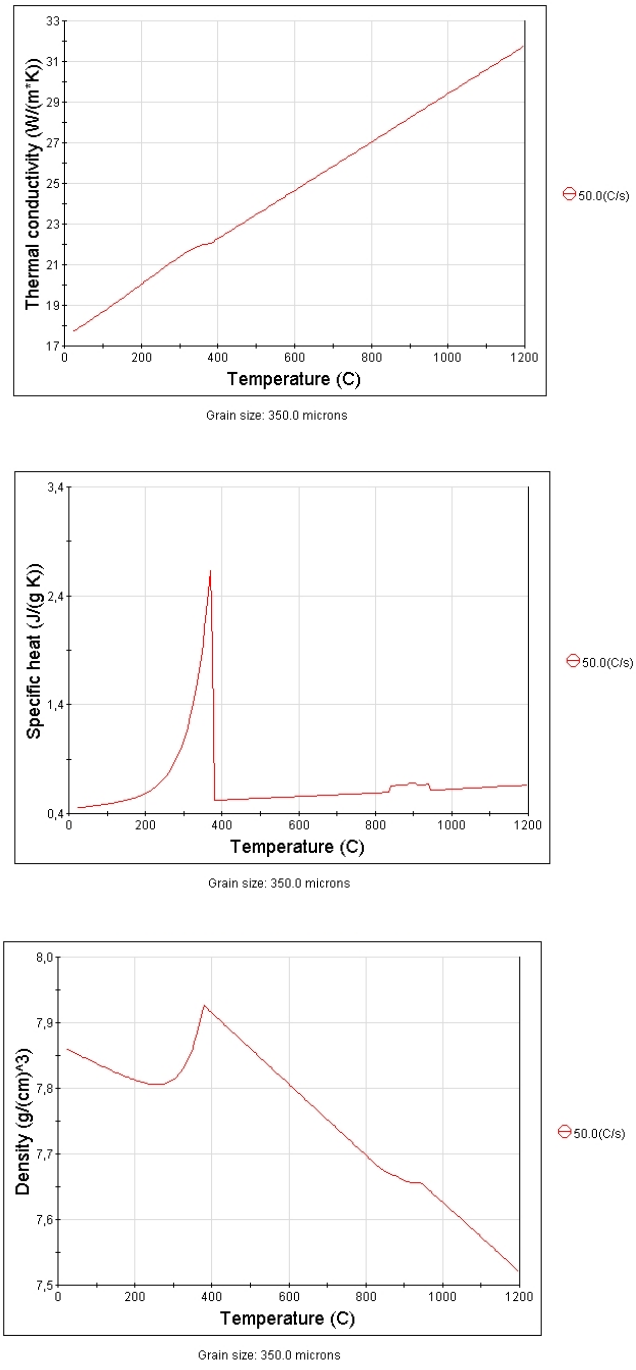

Figure A.14: Thermal conductivity, specific heat and density as a function of temperature.

A.6 Gleeble®-3800 QuikSim / Heat Affected Zone Programming

A Gleeble system with a series 3 digital control and the QuickSim Software package (installed on a Windows-based Computer) is required to use the HAZ programme. After starting the HAZ module in the QuickSim application, one can select among different mathematical models for the description of the cooling behaviour due to the heat transfer.
The Rykalin 2D model was used for all HAZ physical simulation experiments, but the material properties (green frame in the below figure) are mandatory fields regardless of the model. The parameters of the main window were set to the values shown in the following figure:

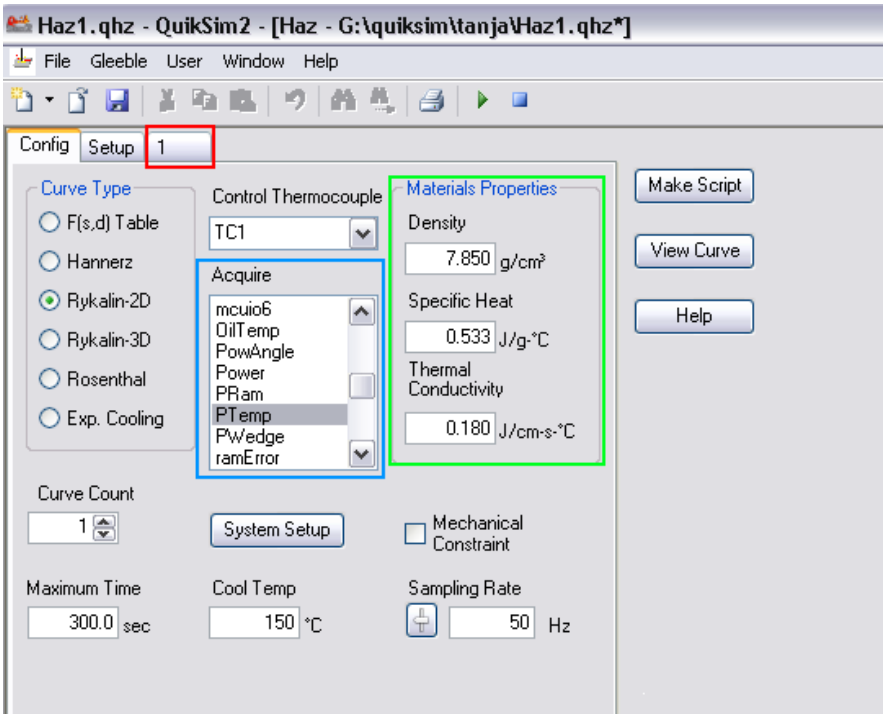

The control thermocouple refers to the one welded on the horizontal center of the specimen and is chosen by selecting the related TC connection. The selection of the acquisition variables (blue frame) is done by simply clicking them and the variables appear highlighted in blue when selected (deselection is done when clicking again an the variable). The selected variables for acquisition are: PTemp, TC1, TC2, TC3, TC4.
The parameters related to the model selected, i.e. Rykalin 2D, can be entered in a separete window which is accessed by selecting the tabulator named "**1**" which is

highlighted with a red frame in the above figure.
The variables of the Rykalin-2D model were set to:

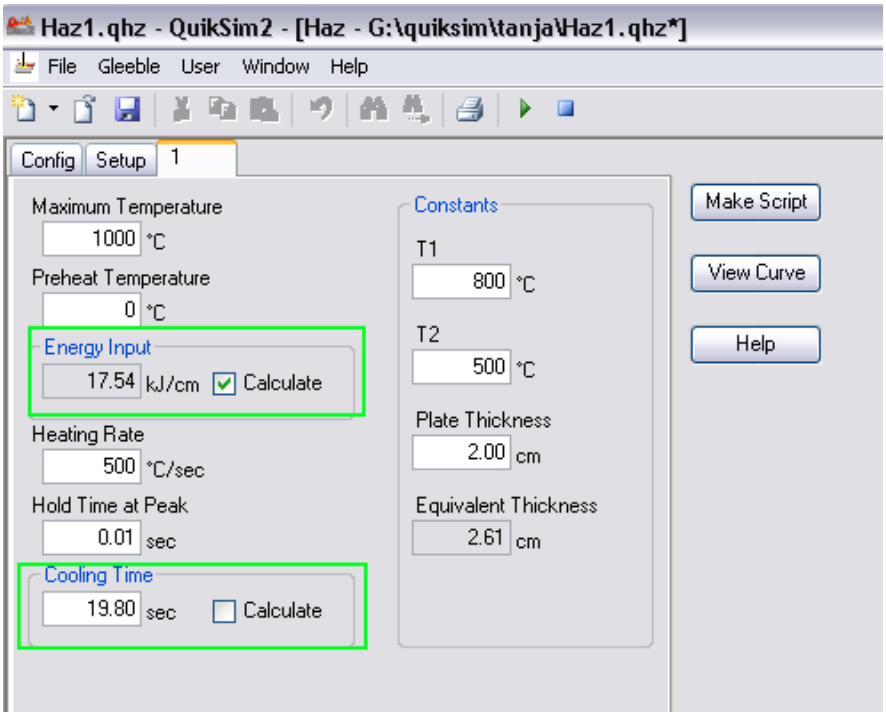

Via the "**Make Skript**"-button, the script is generated in Gleeble Script Language (GSL) and opened in a separate editor window where it still can edited and saved before the run. The "**View curve**"-button generates a preview of the curve to obtain the desired cooling behaviour based an the values entered.

A.7 Vapor Pressure Data

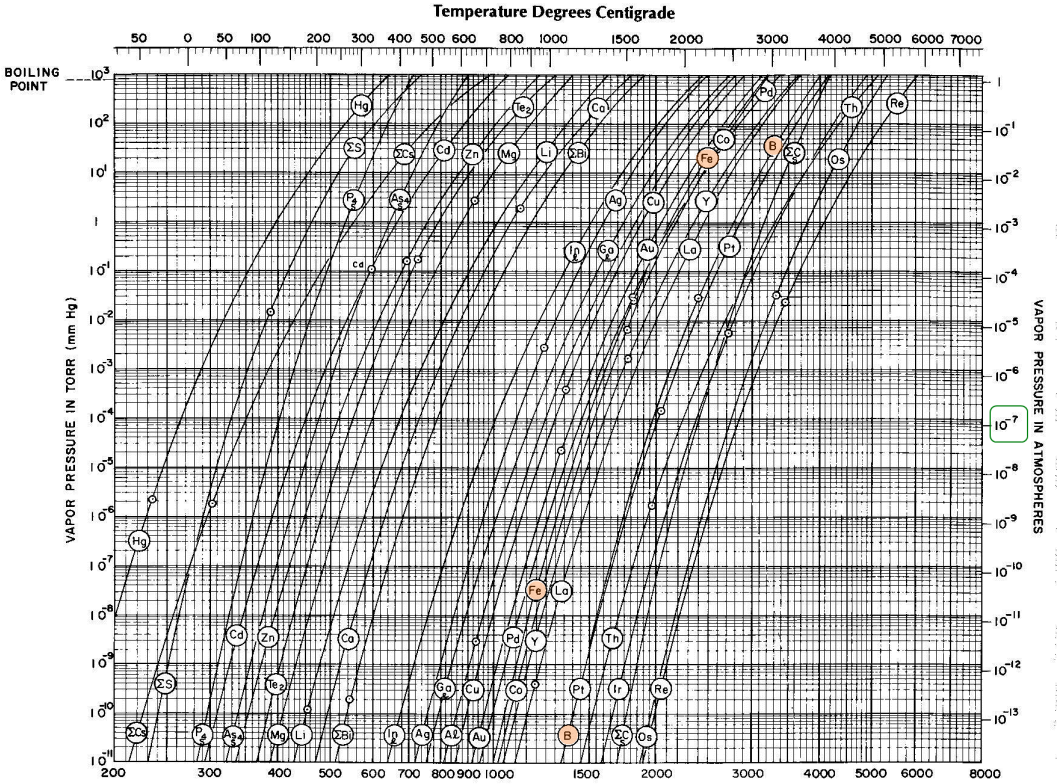

Figure A.15: Vapor pressure data of elements, the highlighted elements are relevant alloying elements of the present weld test plate. A typical pressure in the EBW vacuum chamber is highlighted with a green frame (1 atm = 1013.25 mbar). Temperature skale on top in Degrees Centigrade and on bottom in Kelvin. The charts can be found in [55].

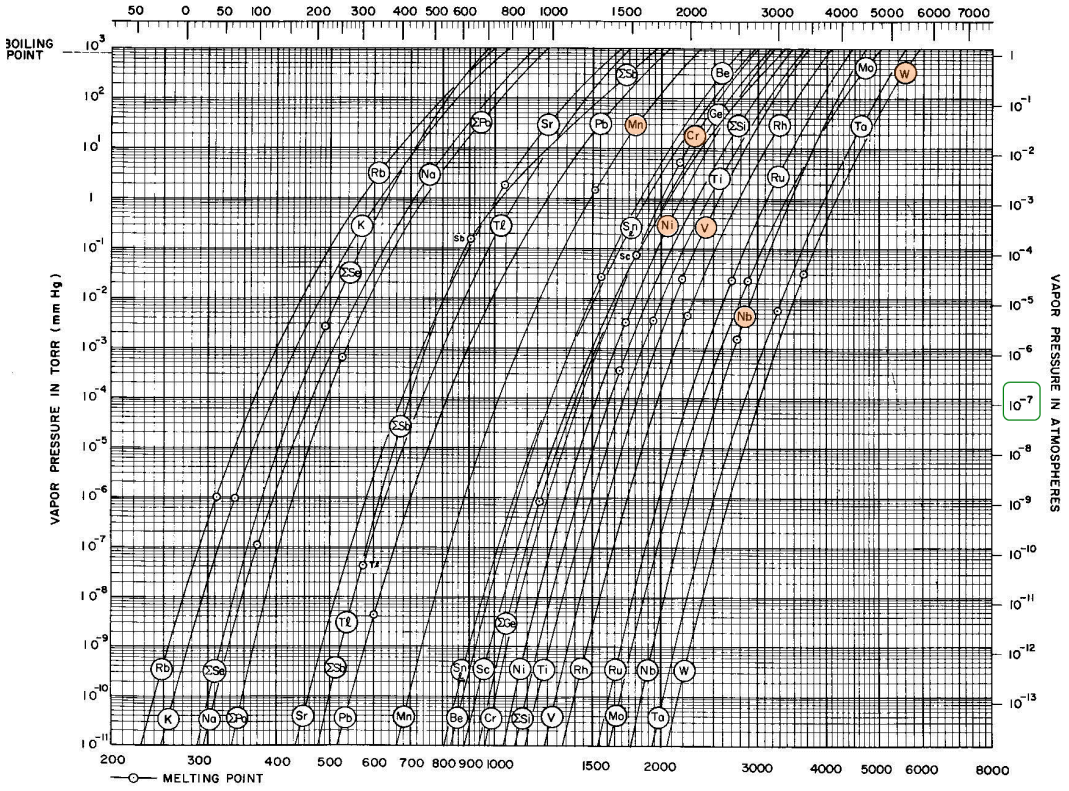

Figure A.16: Vapor pressure data of elements, the highlighted elements are relevant alloying elements of the present weld test plate. A typical pressure in the EBW vacuum chamber is highlighted with a green frame (1 atm = 1013.25 mbar). Temperature skale on top in Degrees Centigrade and on bottom in Kelvin. The charts can be found in [55].